SOME OPTICAL TECHNIQUES FOR CHARACTERIZING MICRO-SCALE PARTICLES AND ON-CHIP PLASMONIC NANOFOCUSING

A Thesis
Presented to
The Academic Faculty

by

Ye Luo

In Partial Fulfillment
of the Requirements for the Degree
Doctor of Philosophy in the
School of Electrical and Computer Engineering

Georgia Institute of Technology
August 2014

SOME OPTICAL TECHNIQUES FOR CHARACTERIZING MICRO-SCALE PARTICLES AND ON-CHIP PLASMONIC NANOFOCUSING

Approved by:

Professor Ali Adibi, Advisor
School of Electrical and Computer Engineering
Georgia Institute of Technology

Professor John Buck
School of Electrical and Computer Engineering
Georgia Institute of Technology

Professor Gee-Kung Chang
School of Electrical and Computer Engineering
Georgia Institute of Technology

Professor Haomin Zhou
School of Mathematics
Georgia Institute of Technology

Professor Stephen Ralph
School of Electrical and Computer Engineering
Georgia Institute of Technology

Date Approved: May 5, 2014

To my parents,

Jian Luo and Xiutang Luo,

with love.

ACKNOWLEDGEMENTS

I wish to first thank Prof. Ali Adibi for his support, guidance, patience and encouragement in this thesis process, and also for giving me the freedom to explore different research areas. I enjoyed the atmosphere in the Photonic Research Group at Georgia Tech led by Prof. Adibi.

I would also like to thank my committee members, Prof. Gee-Kung Chang, Prof Stephen Ralph, Prof. John Buck, and Prof. Haomin Zhou, for their time and valuable comments on my work.

Special thanks to Dr. Jiandong Huang and Dr. Maysam Chamanzar, with whom I had the precious opportunities to work closely with. I would also like to thank my other collaborators, Dr. Charles Camp, Dr. Aniello Apuzzo and Prof. Sylvain Blaize, all of whom I had great experience with.

I am also grateful to all my former and current colleagues in the Photonic Research Group for unsparingly sharing their ideas and experience with me, especially Dr. Reza Eftekfar, Dr. Siva Yegnanarayanan, Dr. Fengtao Wang, Dr. Qing Li, Zhixuan Xia, Dr. Amir Atabaki, Dr. Omid Momtahan, Dr. Chaoray Hsieh, Dr. Mohammad Soltani, Dr. Babak Momeni, Dr. Saeed Mohammadi.

Finally, I wish to express my deep gratefulness and thankfulness to my parents for their everlasting support and encouragement.

TABLE OF CONTENTS

LIST OF FIGURES

SUMMARY

The content in the dissertation is divided into two main categories: (1) micro-particle characterization techniques based on elastic light scattering, and (2) ultra-compact on-chip plasmonic light concentration and its applications. For category (1), I developed two techniques, one is in vitro and the other is in the scenario of flow cytometry. I investigated theoretically and experimentally the spectra of scattered light from spherical dielectric particles at certain fixed angles, and demonstrate the linearity between the peak positions in the Fourier domain and the diameter of the particle. Based on this discovery, I demonstrate an efficient and accurate technique for in-vitro micro-particle sizing. Moreover, I theoretically analyzed the far-field elastic scattering signals from micro-particles passing through a flow cytometer with tightly focused incident beams, and established an algorithm to extract size information from the detected signals with higher accuracy than that in conventional flow cytometry systems. For category (2), I proposed an on-chip plasmonic nanofocusing technique whose unit device is a plasmonic triangle-shaped nanotaper mounted upon a dielectric optical waveguide. This structure provides highly efficient and robust light concentration into the tip of the nanotaper. Near-field measurements were performed to thoroughly investigate a fabricated sample and prove the concept. I also proposed theoretically a novel concept named phase-induced local-field configuration with logic behaviors, whose actuators are composite devices built on units of single on-chip plasmonic light concentrators mentioned above.

CHAPTER I

INTRODUCTION

The content in the thesis is divided into two main categories: (1) some micro-particle characterization techniques based on elastic light scattering, and (2) ultra-compact on-chip plasmonic light concentration. The first category includes Chapters 2, 3 and 4, and the second category includes Chapters 5, 6 and 7. In particular, Chapter 2 gives a concise description of elastic light scattering theories, Chapter 3 describes a Fourier technique of particle sizing based on spectrum detection on elastic light scattering, Chapter 4 gives a theoretical analysis on flow cytometry based on focused incident light beam with a comparison to experimental results, Chapter 5 proposes and conceptually demonstrates an ultra-compact on-chip plasmonic device for light concentration, Chapter 6 shows the design, fabrication, and near-field measurements of on-chip plasmonic light concentration on a Silicon platform, and Chapter 7 discusses two applications, plasmonic nanotrapping and local-field configuration, of this plasmonic device.

In this chapter, I will give a brief introduction to the backgrounds and motivations of the above work.

1.1 Particle Characterization from Elastic Light Scattering

Various elastic-light-scattering methods have been reported and used for efficient and accurate measurement of the geometrical properties (size, refractive index, shape, distribution, concentration etc.) of micro-particles, which is essential for many biomedical applications including early cancer detection [1], cellular morphology exploration [2] and bacteria size determination [3]. In general, these methods can be

divided into two categories [4]: (1) methods that analyze light scattering from a particle suspension, and (2) methods that analyze light scattering from an individual particle. For the techniques in the first category, the scattering profiles are usually averaged over all the particles in the suspension. In particular, analyzing the angular scattering patterns [2, 6] and spectral scattering patterns [7, 8] are two primary approaches for particle characterization. The major techniques in the second category are based on flow cytometry [5]. Conventional flow cytometry can record the forward-scattered light (FSC) and the side-scattered light (SSC) with individual particles/cells passing through the light detection spot. The data collected in this way are relatively rough in accuracy when determining particle parameters. In the mid-90's, a scanning-flow-cytometry (SFC) technique was developed. Using this technique, the angular light-scattering-pattern of an individual particle passing through the detection spot can be measured.

Inverse problems need to be solved to obtain the scatterer's parameters from the scattering profiles, which is the most challenging part to the light-scattering techniques for particle characterization. The first step towards solving the inverse scattering problems is to solve the direct scattering problems, i.e., what are the scattering patterns for the scatterers. The most commonly used scattering model is Mie theory [9,10] which gives precise analytical solutions to the scattering problem of micro-spheres. In this case, the scatterer's parameters are usually the diameter of the sphere, the relative refractive index of the sphere, or both. Other methods that can attack the problem of scattering from nonspherical particles include the T-matrix approach [11] which allows the exact simulation of light scattering from micro-particles of some basic shapes, the discrete dipole approximation (DDA) [12,13] which approximates the scattering from micro-objects of varied shapes by a finite set of dipoles, and the Wentzel-Kramer-Brillouin (WKB) approximation [15, 83] which assumes the relative refractive index of the micro-object is close to 1.

In the first category of elastic-light-scattering methods, a typical angular scattering pattern or a spectral scattering pattern has some oscillatory features, which can be used to reconstruct particle parameters. At present, most of those methods based on light scattering spectroscopy (LSS) are investigated in a back-scattering geometry, since it has been shown that the spectrum over the wavenumber of back-scattered light has a periodic component with an oscillation frequency proportional to the particle size [7]. However, certain data fitting algorithms based on look-up tables are still required, which can be quite time-consuming [8]. In Chapter 3, I will present a Fourier transform technique using the scattering spectrum at a certain fixed angle, which can provide an accurate reconstruction of particle sizes [17].

In the second category of elastic-light-scattering methods, most flow cytometers nowadays Forward-scattered light (FSC) is proportional to cell-surface area or size. FSC provides a suitable method of detecting particles greater than a given size independent of their fluorescence and is therefore often used in immunophenotyping to trigger signal processing. Side-scattered light (SSC) is proportional to cell granularity or internal complexity. SSC is a measurement of mostly refracted and reflected light that occurs at any interface within the cell where there is a change in refractive index. SSC is collected at approximately 90 degrees to the laser beam by a collection lens and then redirected by a beam splitter to the appropriate detector.

Most of the flow cytometers nowadays uses loosely focused incident light beams. However, tightly focused beams are used in the MCARS (Multiplex Coherent Anti-Stokes Raman Scattering) flow cytometer developed by my colleague Charles H. Camp Jr. [18]. In Chapter 4, I will present a theoretical analysis of the elastic scatter in this platform of focused incident light beam.

1.2 Plasmonic Light Concentration

According to the review [19], plasmonic light concentrators (PLC) can be divided into two big categories: resonant and non-resonant. In resonant structures, plasmon oscillations can be excited resonantly by light waves at specific optical frequencies and produce a strong field enhancement. Such structures include metallic nano-particles, nano-disks, nano-rods, etc [20]. The discussion in this section will focus on non-resonant PLCs, on which I will give a further classification.

Interference-induced plasmonic nanofocusing. For this type of techniques, the plasmonic excitation sites on a metal film are carefully tuned so that the propogation of surface plasmon polaritons (SPP) originated at the sites can get focused into a hot spot on the metal film. Some people call their structures "plamonic lenses", and others stick to the term "nanofocusing". Typical planar patterns for plasmonic excitation on the metal film include individual circular rings [21], multiple concentric rings [22], curved arrays of nanoholes [23], and certain coaxial structures [24].

Geometry-induced plasmonic nanofocusing. In contrast to the interference-induced nanofousing techniques which are planar in nature and lack of accurate control on the focus point, geometry-induced techniques are more versatile with higher concentrating ability. In principle, tapering the cross section of the SPP propagation gradually will increase the intensity of the SPP and the slow down its group velocity. At the tip end of the taper, the group velocity becomes infinity which mean the surface plasmon becomes localized and the energy is highly concentrated [25–40].

On-chip plasmonic light concentrators. The aforementioned interference-induced and geometry-induced naofocusing techniques all have the SPP excited in free space. Therefore, the light energy is concentrated from a "$> 10\lambda$" scale to a "$< \lambda$" scale with λ being the wavelength. The length of the SPP propagation is usually in the order of $10\,\mu$m. There are two issues which limit the concentration efficiency. First, the efficiency of SPP excitation is usually quite low. Therefore only a small portion

of light energy is coupled into surface plasmons. Second, the SPP propagation length is limited by the lossy nature of metal. Very recently, several approaches of realizing plasmonic nanofocusing on integrated-optics platforms have been reported [42–44]. Using these on-chip light concentration techniques, the light energy is coupled from a photonic waveguid to a plasmonic structure (usually a metallic taper) and then concentrating the light energy to the tip of the taper. The coupling from the photonic waveguide to the plasmonic structure is efficient and the plasmonic part is usually compact. The plasmonic structures concentrate light from a "$\sim \lambda$" scale to a "$< \lambda/10$" scale. Therefore, the two limitations for free space plasmonic nanofocusing can be well addressed by the on-chip techniques.

In Chapters 5, 6, and 7, I will show the design, experimental demonstration and applications of a novel ultra-compact on-chip plasmonic light concentrator [45, 58].

CHAPTER II

ELASTIC LIGHT SCATTERING THEORY

Mie theory (also known as Mie scattering, the Mie solution, or the Lorenz-Mie solution), named after Gustav Mie and Ludvig Lorenz, was developed as an analytical theory of electromagnetic plane wave scattering by a spherical particle. The formalism of Mie solutions is based on solving the coefficients of the scattered field from the coefficients of the incident plane wave under radiating spherical vector function expansions using the boundary conditions on the spherical surfaces. If the scatterer has a size much smaller than the light wavelength, a dipole model makes a good approximation. If the scatterer has a size much larger than the light wavelength, we may refer to geometric optics to approximately solve the scattering problem. But for scatterers of size similar to the wavelength of the incident light, Mie theory provides a more exact approach. Since the elastic light scattering problems considered in this thesis fall into the last category of particle sizes, the formalism of Mie solutions (following Bohren and Huffman [16]) is to be concisely presented in this chapter. I will also give brief descriptions to other computational methods.

2.1 Formulation of Mie Scattering Functions of Spherical Dielectric Particles

For Mie particles, the far field scattering functions represent the scattering in all the angles. In general, we have two scattering functions $S_1(\theta)$ and $S_2(\theta)$ for two polarizations (here θ is the angle between the incident vector and the scattering vector), and they are quite similar to each other at small angles.

Let the angle ϕ be the angle between the incident electrical field and the scattering plane. Let E_θ^s be the scattered far-field component in the scattering plane, and E_ϕ^s

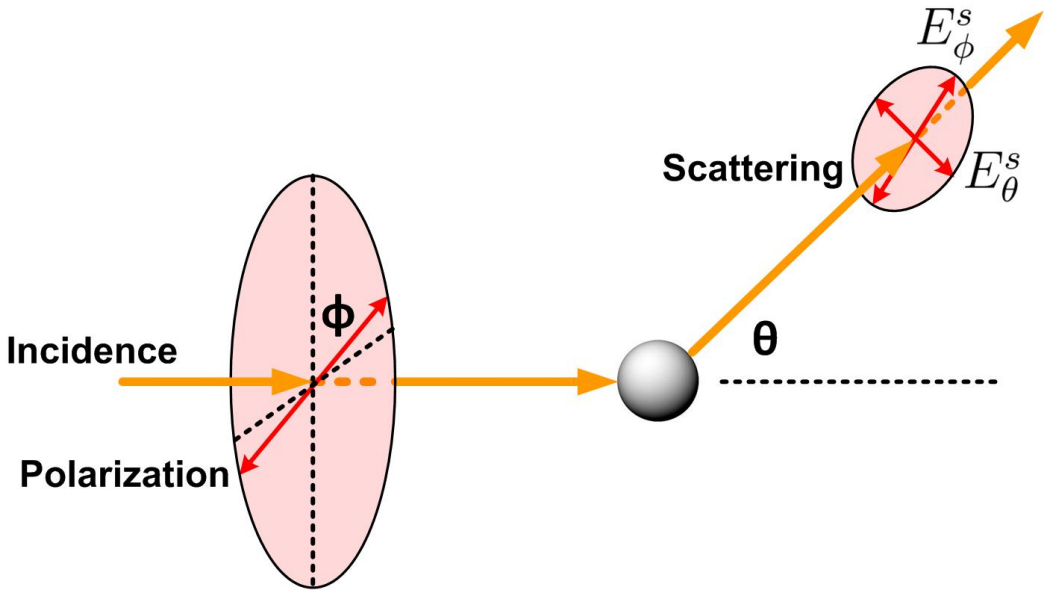

Figure 1: A schematic for Mie scattering. The scattering plane is defined by the incident vector and the scattering vector.

be the orthogonal component (perpendicular to the scattering plane). Then

$$E^s_\phi = \frac{e^{ikr}}{-ikr}\sin(\phi)S_1(\theta) \tag{1}$$

$$E^s_\theta = \frac{e^{ikr}}{-ikr}\cos(\phi)S_2(\theta). \tag{2}$$

If the incident light polarization is perpendicular to the scattering plane, then $\phi = \pi/2$, $E^s_\theta = 0$ and $E^s_\phi = \frac{e^{ikr}}{-ikr}S_1(\theta)$. On the contrary, if the polarization is in-plane, then we will only have E^s_θ.

Let n_1 be the refractive index of the scattering sphere, n_0 the refractive of the ambient medium, and $m = n_1/n_0$ the refractive index of the sphere relative to the ambient medium, λ the wavelength in vaccuumm, $\lambda_0 = \lambda/n_0$ the wavelength in the ambient medium, d the radius of the sphere and $k = 2\pi/\lambda_0 = 2\pi n_0/\lambda$ the wave number, and $x = kd/2 = \pi d n_0/\lambda$ the size parameter.

Then the scattering functions $S_1(\theta)$ and $S_2(\theta)$ can be expressed in the following

terms:

$$S_1(\theta) = \sum_{n=1}^{\infty} \frac{2n+1}{n(n+1)} [a_n \pi_n(\cos\theta) + b_n \tau(\cos\theta)], \tag{3}$$

$$S_2(\theta) = \sum_{n=1}^{\infty} \frac{2n+1}{n(n+1)} [a_n \tau_n(\cos\theta) + b_n \pi(\cos\theta)] \tag{4}$$

where

$$\pi_n(\cos\theta) = \frac{1}{\sin\theta} P_n^1(\cos\theta), \tag{5}$$

$$\tau_n(\cos\theta) = \frac{d}{d\theta} P_n^1(\cos\theta). \tag{6}$$

Here P_n^1 is the associated Legendre polynomial. The functions $\pi_n(\cos\theta)$ and $\tau_n(\cos\theta)$ can be computed by the recurrence relations

$$\pi_n = \frac{2n-1}{n-1} \cos\theta \cdot \pi_{n-1} - \frac{n}{n-1} \pi_{n-2}, \tag{7}$$

$$\tau_n = n \cos\theta \cdot \pi_n - (n+1)\pi_{n-1} \tag{8}$$

starting with the first few terms

$$\pi_0 = 0, \pi_1 = 1, \pi_2 = 3\cos\theta, \tau_0 = 0, \tau_1 = \cos\theta, \tau_2 = 3\cos(2\theta). \tag{9}$$

Suppose the relative magnetic permeability of the sphere to the ambient medium is 1 (which is the case for all our applications). Then the coefficients a_n and b_n are given by

$$a_n = \frac{m^2 j_n(mx)[x j_n(x)]' - j_n(x)[mx j_n(mx)]'}{m^2 j_n(mx)[x h_n^{(1)}(x)]' - h_n^{(1)}(x)[mx j_n(mx)]'}, \tag{10}$$

$$b_n = \frac{j_n(mx)[x j_n(x)]' - j_n(x)[mx j_n(mx)]'}{j_n(mx)[x h_n^{(1)}(x)]' - h_n^{(1)}(x)[mx j_n(mx)]'}. \tag{11}$$

Here j_n and $h_n^{(1)}$ are spherical Bessel functions of order n.

Some examples of scattering functions are shown in Section 4.1.1.2.

2.2 Other Computational Methods

2.2.1 Discrete Dipole Approximation

There are several techniques for computing scattering of radiation by particles of arbitrary shape. The discrete dipole approximation is an approximation of the continuum target by a finite array of polarizable points. The points acquire dipole moments in response to the local electric field. The dipoles of these points interact with one another via their electric fields. There are DDA codes available to calculate light scattering properties in DDA approximation.

2.2.2 T-matrix

The technique is also known as null field method and extended boundary technique method (EBCM). Matrix elements are obtained by matching boundary conditions for solutions of Maxwell equations. The incident, transmitted, and scattered field are expanded into spherical vector wave functions. Finite-difference time-domain method Main article: Finite-difference time-domain method

The FDTD method belongs in the general class of grid-based differential time-domain numerical modeling methods. The time-dependent Maxwell's equations (in partial differential form) are discretized using central-difference approximations to the space and time partial derivatives. The resulting finite-difference equations are solved in either software or hardware in a leapfrog manner: the electric field vector components in a volume of space are solved at a given instant in time; then the magnetic field vector components in the same spatial volume are solved at the next instant in time; and the process is repeated over and over again until the desired transient or steady-state electromagnetic field behavior is fully evolved.

CHAPTER III

AN ELASTIC-SCATTERING-BASED FOURIER-TRANSFORM TECHNIQUE FOR PARTICLE SIZING

In this chapter, I will give a Fourier analysis on the far-field light scattering spectra of micro-particles over wavenumber at a certain angle and show the observation that the spectrum can be decomposed into many components with different oscillation frequencies, each with linear dependence on the particle size.

For most angles, there is one oscillatory component predominant over the others, which I call the "major oscillatory component". The Fourier transform is used to separate these oscillatory components. By isolating the regime of the major oscillation in the Fourier domain and inversely mapping the position of the peak in the Fourier domain (corresponding to the oscillation frequency) to the particle size, I propose and experimentally demonstrate a simple and fast particle sizing technique with a robust data processing algorithm and a flexible detection system [17].

3.1 Fourier Transforms of Scattering Spectra of a Mie Paritcle

The scattering spectra of a spherical particle can be calculated analytically using Mie theory [9, 10] with formulation discussed in Section 2.1. Consider a dielectric sphere of diameter d and refractive index n_1 in a surrounding medium of refractive index n_0. For a nonpolarized plane wave of intensity I_{in} and wavelength λ incident on this particle, the far-field scattering intensity I_{sca} at scattering angle θ can be expressed

as

$$I_{\text{sca}}(\theta, \lambda, d, n_0, n_1) = \frac{\lambda^2}{(n_0\pi)^2 r^2}(|S_1(\theta, x, m)|^2 + |S_2(\theta, x, m)|^2) I_{\text{in}}. \tag{12}$$

Here, r is the distance from the scatterer to the detector, and S_1 and S_2, obtained via Mie calculations, are scattering amplitudes for polarizations perpendicular and parallel to the scattering plane, respectively. They are functions of the scattering angle θ, a dimensionless size parameter $x = n_0\pi d/\lambda$, and the refractive index ratio $m = n_1/n_0$.

Consider the scattering spectra of polystyrene suspensions, i.e., dielectric microspheres ($n_1 = 1.59$) in water ($n_0 = 1.33$). Figure 2(a) shows the calculated spectra over wave number $1/\lambda$ for suspensions of particles of diameter $10\,\mu$m at scattering angles of 10°, 30°and 60°, with unpolarized incident light. In each spectrum, there exists an easily observable ripple. It can be observed that the oscillation of these ripples, which is generated by the combined effects of diffraction and resonance in the dielectric spheres, is periodic. Furthermore, aside from the prominent major ripple, there are more oscillatory components: a slow background oscillation and higher order ripples oscillating with higher frequency. Note that in Eq. (12), the particle diameter d is tied with wave number $1/\lambda$ by multiplication into a dimensionless size parameter $x = n_0\pi d/\lambda$. This implies that the oscillation frequencies are proportional to the particle size. Figure 2(b) illustrates such linear relationships. The Fourier transforms of downshifted spectra (to annihilate the DC offset) versus ($0.001\,\text{nm}^{-1} \sim 0.0025\,\text{nm}^{-1}$) are plotted for particle sizes in a range from $5\,\mu$m to $20\,\mu$m. The major ripple corresponds to the bright straight line, while the background oscillation and higher order ripples generate other observable straight lines.

A particle sizing technique can be developed based on this phenomenon. The major oscillatory component in a scattering spectrum is well-isolated from other components in the Fourier domain, and its corresponding peak position can be linearly mapped to particle size. As the spectrum measurements are usually taken over

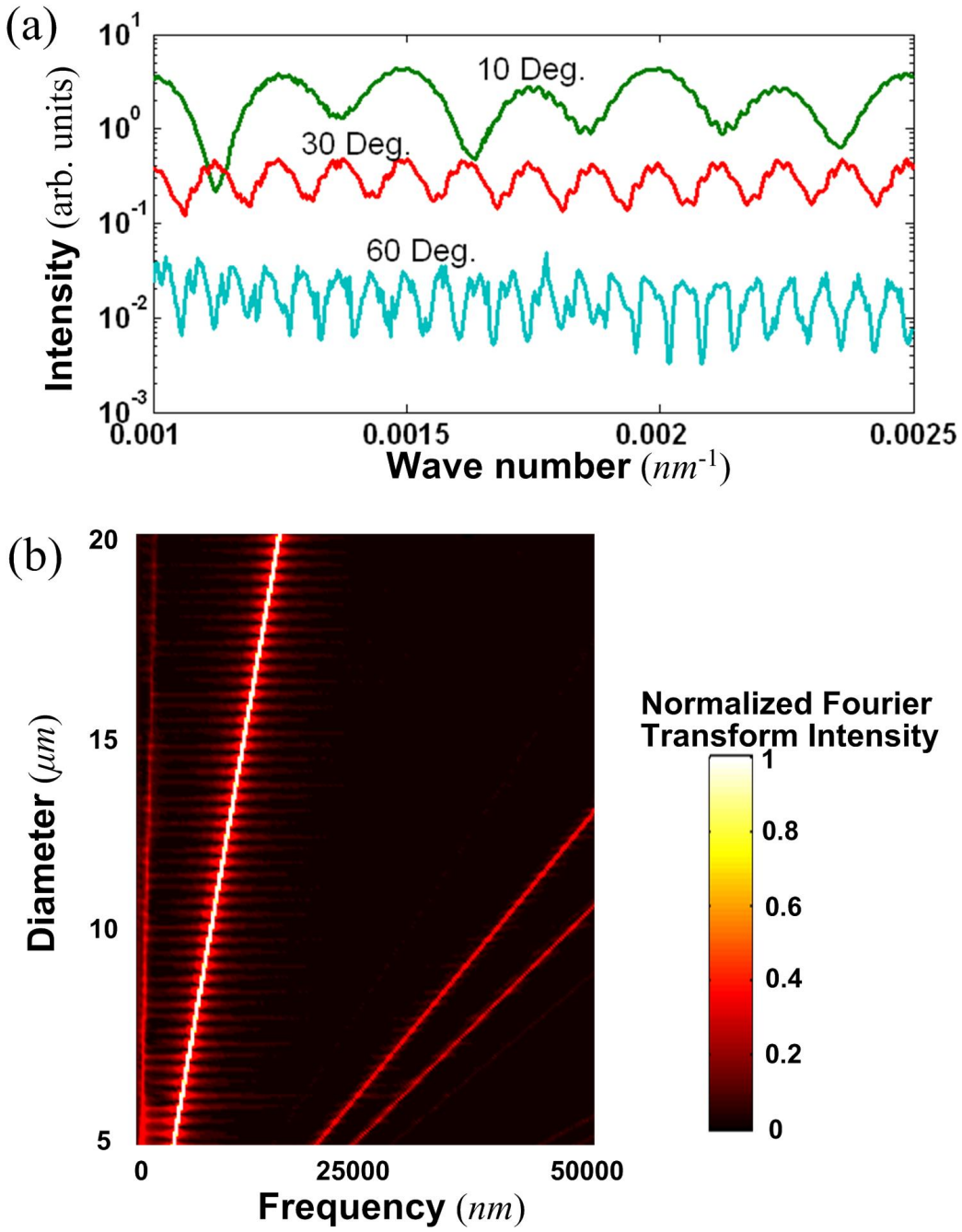

Figure 2: (a) The calculated scattering spectra as a function of wavenumber $1/\lambda$ at different scattering angles for 10 μm polystyrene particles. (b) The linear evolution of Fourier transform of spectrum over $1/\lambda$ with the increasing of particle size, scattering angle fixed to 30°. Note that the "frequency" here is the Fourier transform variable in Eq. (13).

wavelength, it is necessary to convert spectra over wavelength λ into spectra over $1/\lambda$ before applying a Fourier transform. Consider a wavelength sampling sequence $\lambda_1, \lambda_2, \cdots, \lambda_n$ and a spectrum $I(\lambda)$. Then the Fourier transform of the corresponding spectrum over $1/\lambda$ is

$$\widetilde{I}(f) = \sum_{j=1}^{n-1} \frac{1}{2}[(I(\lambda_j)-C)\exp(-i\frac{2\pi}{\lambda_j}f)+(I(\lambda_{j+1})-C)\exp(-i\frac{2\pi}{\lambda_{j+1}}f)](\frac{1}{\lambda_j}-\frac{1}{\lambda_{j+1}}), \quad (13)$$

where C is used to annihilate the DC offset of the spectrum with an expression

$$C = \frac{1}{2}(\frac{1}{\lambda_j} - \frac{1}{\lambda_{j+1}})^{-1} \sum_{j=1}^{n-1}[I(\lambda_j) + I(\lambda_{j+1})](\frac{1}{\lambda_j} - \frac{1}{\lambda_{j+1}}). \quad (14)$$

3.2 Experimental Demonstrations on Particle Suspensions of a Uniform Particle Size

The experimental setup for measuring the light scattering spectra is shown in Figure 3. The white light source is a tungsten lamp, incorporating a monochromator and a lens to provide collimated wavelength-tunable incident light. A detector is mounted directly onto the arm of a rotating motor. A modulator (light chopper) and a lock-in amplifier are used to improve the signal-to-noise ratio (SNR) of the detection system. The suspension samples are contained in thin quartz cuvettes of 2mm thickness.

To verify the performance of this technique, several measurements of the scattering spectra (wavelength scanned from 490 nm to 790 nm in 1 nm intervals) are taken for a number of polystyrene suspensions with different particle sizes, which are dilute enough to validate the single scattering model. Due to the refraction at the water-air interface, the detection angle θ determines the scattering angle θ' by Snell's law ($\sin\theta' = \sin\theta/n_0$). Figure 4(a) shows the theoretical and experimental downshifted spectra for the suspension of 10 μm particles, with corresponding Fourier transforms shown in Figure 4(b). Note that the major peak derived from a measurement is not as dominant as from theoretical calculations, while higher order peaks are not observable at all. The explanation depends on several factors: (1) the probe collects light from a

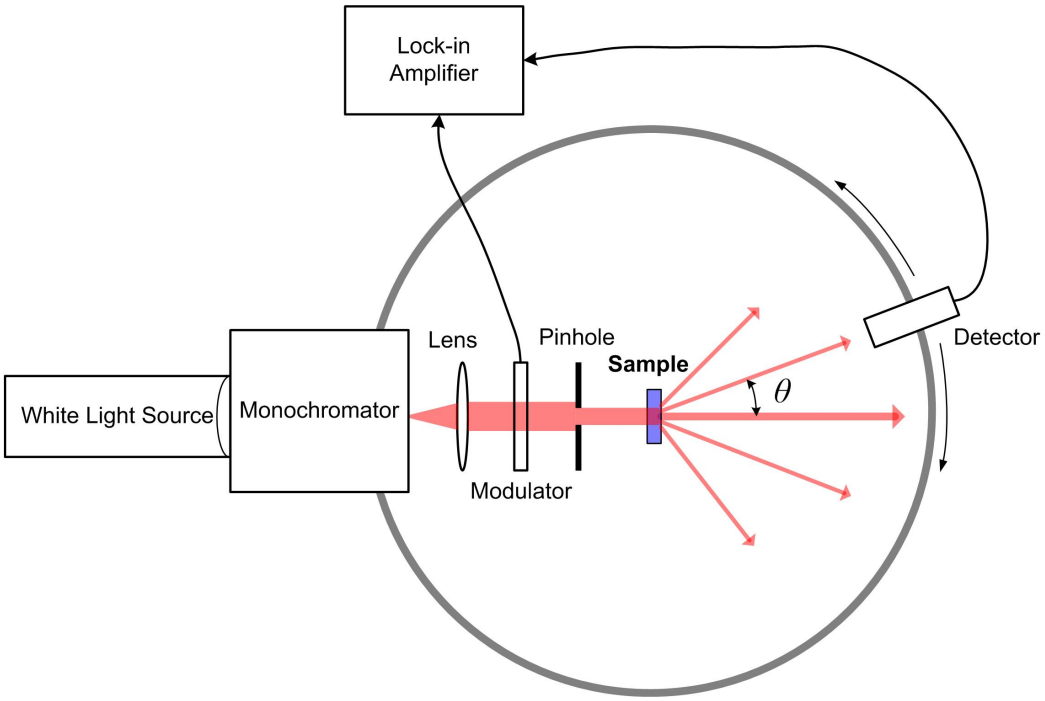

Figure 3: Schematic of the angle and wavelength scanning detection system.

small range of scattering angles due to the nonzero spot area of scatterers and the numerical aperture of the detector, (2) there exists small nonuniformity of particle sizes in each sample, and (3) multiple scattering cannot be neglected completely. All these factors combine to smooth away the higher order ripples and decrease the oscillation amplitude of the major ripple, while having little effect on the slow background oscillation. However, since the oscillation frequencies of these components remain consistent, the precision of particle size estimation is minimally affected, making this technique robust. The particle size estimations for a set of suspensions, based on the linear relation between the major frequency peak and the particle size, are shown in Figure 4(c), where the average percentage error is less than 5%.

The oscillation frequencies are also angle-dependent. For forward-scattered light (scattering angle less than 90°) investigated in this work, the spectrum at larger angles typically has faster oscillations but lower intensity. This is demonstrated in Figure 6, which shows the theoretical and experimental spectra at different scattering angles.

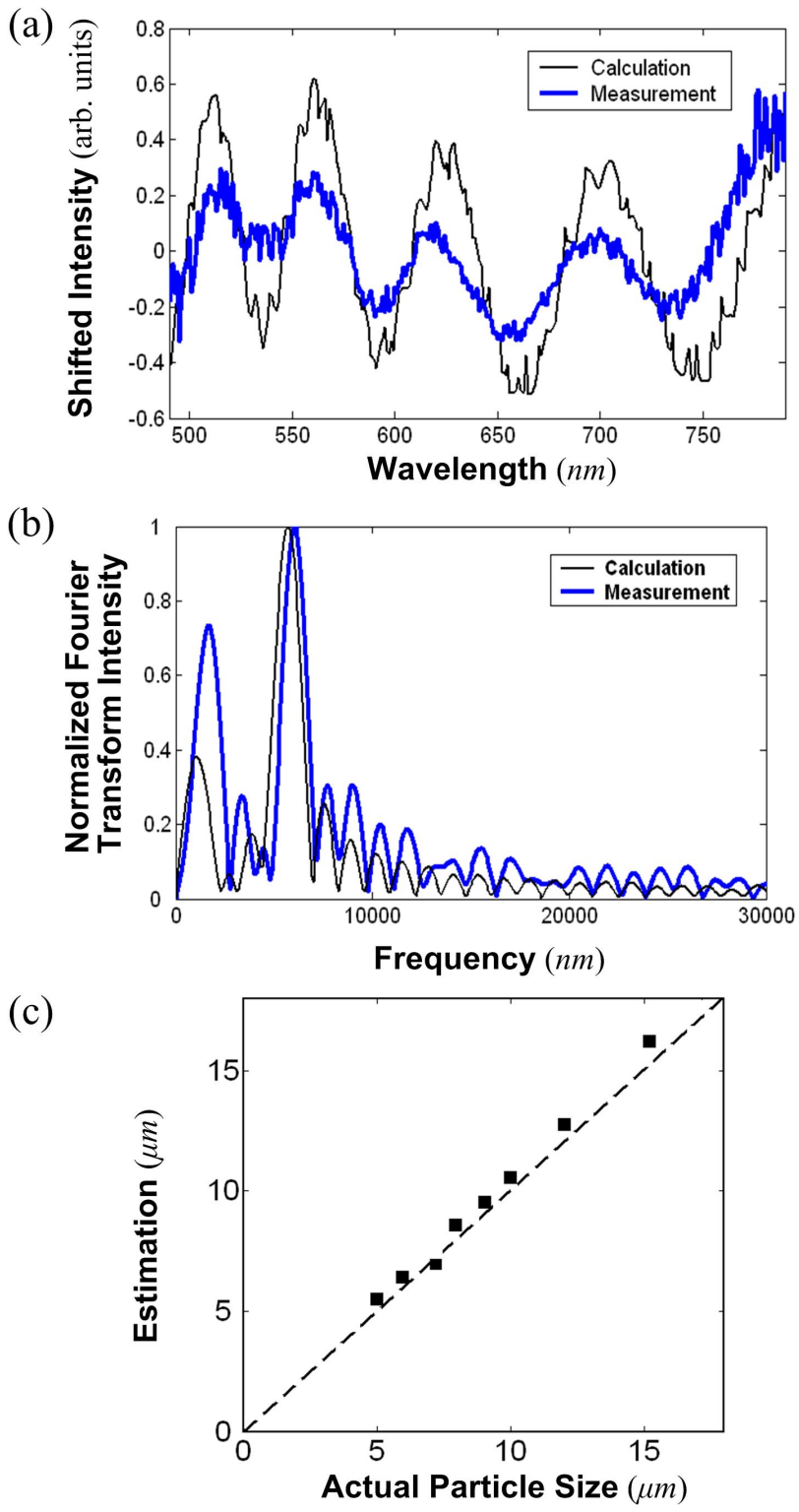

Figure 4: (a) The calculated and measured scattering spectra for the suspension of 10 μm particles, detection angle fixed at 25°. (b) Fourier analyses for the curves in Fig. 4(a). Note that the "frequency" here is the Fourier transform variable in Eq. (13). (c) Particle size determination for a set of suspensions.

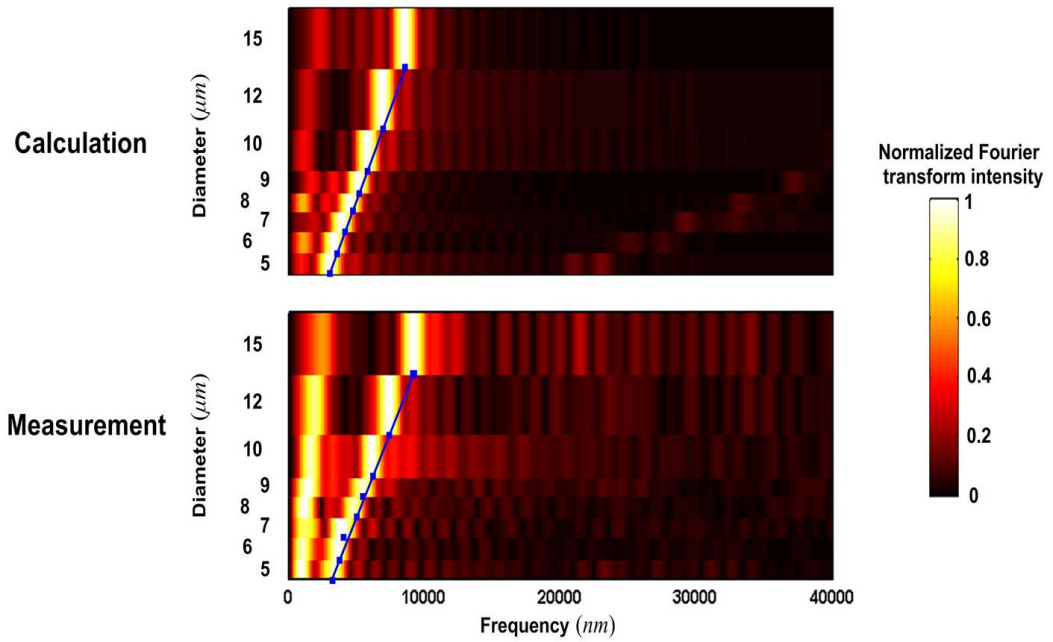

Figure 5: Comparison of Fourier analyses of calculated and measured scattering spectra for a number of suspensions with particle sizes ranging from 5 μm to 15 μm, scattering angle fixed to 25°. Linearity is demonstrated by the straight lines in both cases.

Note that the increasing peak frequencies at higher scattering angles allow for better separation of particle sizes, while the strength reduction in these peaks requires higher sensitivity in the light detection.

Compared to other particle-sizing techniques, this technique uses a simple setup and a fast data processing algorithm. Furthermore, as found in experiments, the discrepancy between the corresponding spectra from a measurement and a computation usually results in the variation of relative amplitude of each oscillatory component, while oscillation frequencies are not affected. This makes this technique robust since the precision is well-preserved even under rough experimental conditions. In addition, the detection angle in our system is flexible, which enables us to employ the angular dependence of the oscillation frequencies to obtain optimum discrimination of particle size based on the available detection capability. The main limitation of this technique is that the peak positions are usually sensitive to the detection angle. Therefore, it

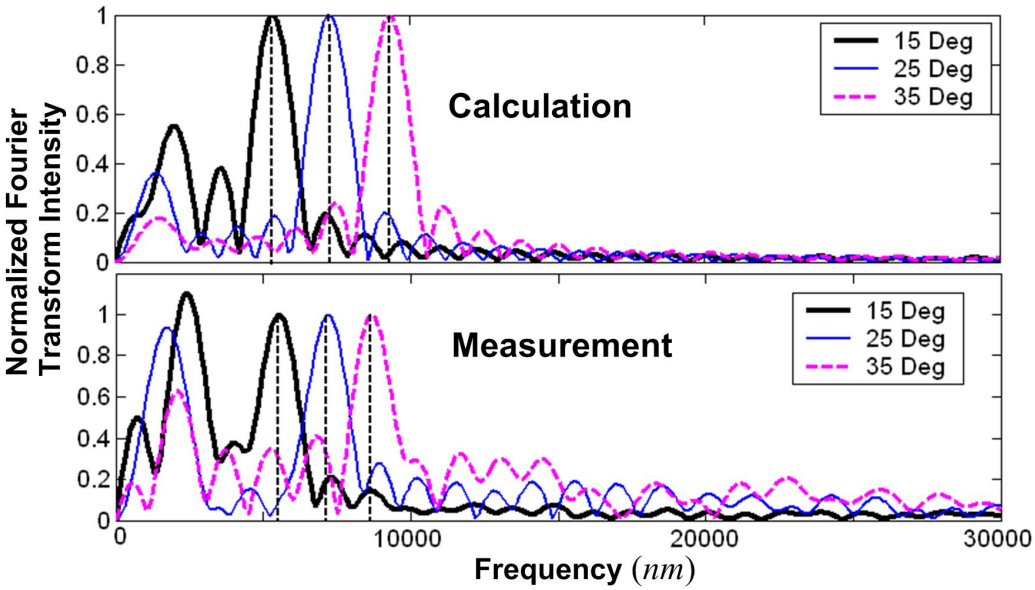

Figure 6: Fourier analyses of calculated and measured scattering spectra for 12 μm particles at detection angles of 15°, 25°and 35°.

is important to obtain accurate angular information. However, this effect can be minimized by an initial calibration of the system with precisely known particle sizes.

In conclusion, I present here a Fourier transform method of particle-size determination using the oscillatory features of scattering spectra, which avoids the complex data fitting algorithms and sophisticated setups that are conventionally used. I show that the linear dependence of the particle size on the major peak in the Fourier transform of the scattering spectrum can be used for particle-size estimation with good accuracy. This technique is simple, robust and flexible.

3.3 Scattering Analysis to Multiple-Sized Particles

The particle-sizing technique can also be applied when the colloidal suspension contains particles of several different sizes.

Figure 7 shows the Fourier analysis of scattering spectrum of a suspension containing particles of diameters 6 μm and 7 μm with the scattering angle fixed at 50°. The two peaks corresponding to 6 μm and 7 μm are prominent in the curve, as marked by red arrows.

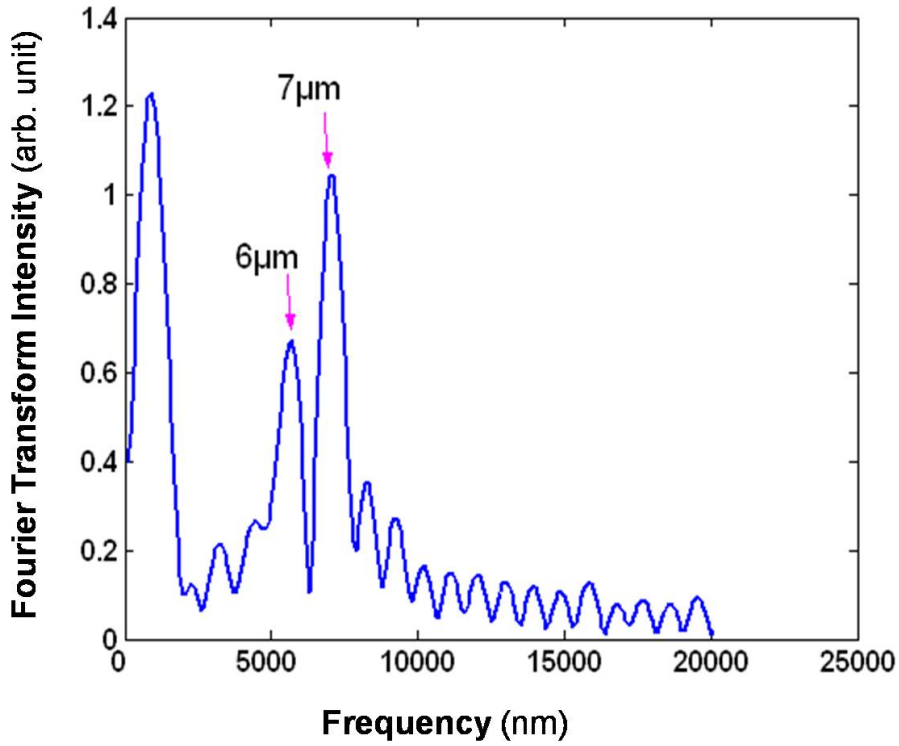

Figure 7: Fourier analysis of measured scattering spectrum for the suspension of $6\,\mu$m $+7\,\mu$m particles, scattering angle fixed to 50 degrees. (Sizes of $1um$ interval are well-discriminated.)

In Figure 8, the number of particle sizes in the suspension is increased to 3, i.e., 6 μm, 8 μm and 12 μm. Correspondingly, one can observe three peaks in the curve of Figure 8.

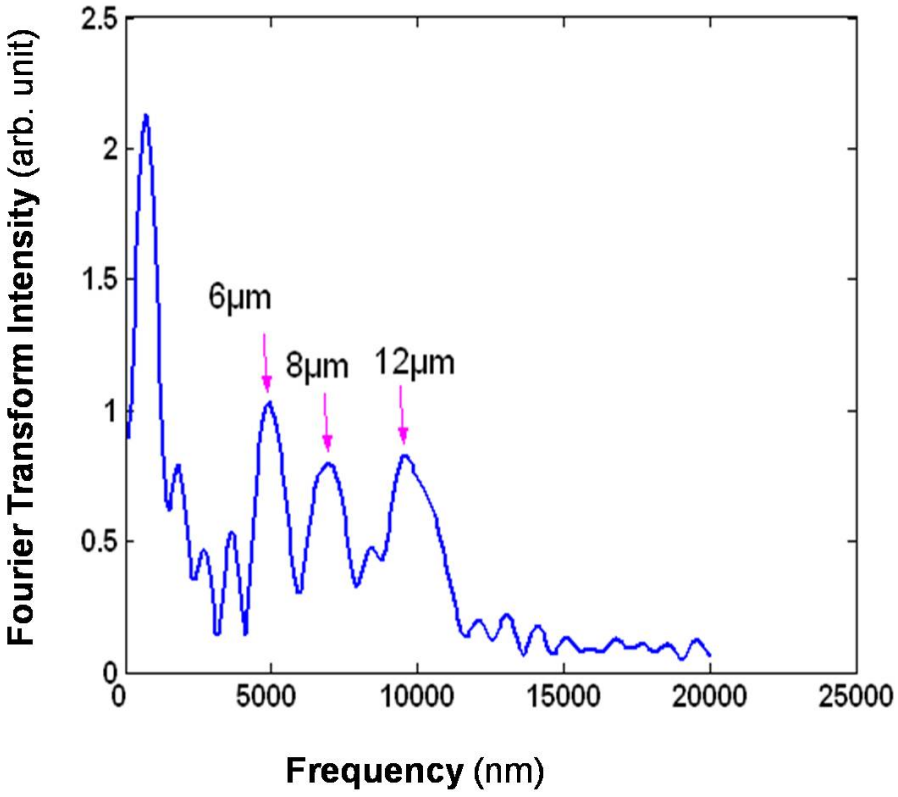

Figure 8: Fourier analysis of measured scattering spectrum for the suspension of 6 μm +8 μm +12 μm particles, scattering angle fixed to 45 degrees.

This Fourier technique is limited when the number of discrete particle sizes increases, or when the particles has sizes continuously distributed in a wide range. In sum, this technique works extremely well for single-sized particle suspensions with high accuracy of size detection, and is applicable to size detections for microparticle suspensions with two or three groups of particle sizes where the particles in each group have relatively uniform particle sizes.

CHAPTER IV

A THEORETICAL ANALYSIS OF OPTICAL SIGNALS FROM A FLOW CYTOMETER USING FOCUSED LIGHT BEAM

Flow cytometry is a technology that simultaneously measures and then analyzes multiple physical characteristics of single particles, usually cells, as they flow in a fluid stream through a beam of light [5]. A flow cytometer is made up of three main systems: fluidics, optics, and electronics. The properties measured include a particles relative size, relative granularity or internal complexity, and relative fluorescence intensity. These characteristics are determined using an optical-to-electronic coupling system that records how the cell or particle scatters incident laser light and emits fluorescence.

Conventionally, light beams used in elastic scatter platforms of flow cytometry are only very loosely focused. Therefore, and a basic plane-wave model is adequate to analyze the scattering signals. In an MCARS (Multiplex Coherent Anti-Stokes Raman Scattering) flow cytometer developed by my colleague Charles H. Camp Jr. [18], multiple tightly focused lasers are used as incident beams. Other than the Raman signals used for species detection, the elastic light scattering signals can also provide important information for particles/cells passing through the detection area. However, the simple plane-wave model is no longer accurate. In this chapter, simulations of elastic light scattering from focused light beams are performed, and a theoretical Fourier model is established to explain the signals. Moreover, a comparison of theory and experimental results are also shown. As a practical application, other than recording the strength of forward scattering (FSC) and side scattering (SSC) which

are common to most flow cytometers, we can also use time-of-flight method to derive a more accurate size information of the particles passing through the detection areas.

4.1 Simulations and a Theoretical Fourier Model of Focused-Beam-Based Flow Cytometry

Figure 9 provides a 3-dimensional schematic of the model for discussion. A focused light beam propagates along the $Z+$ direction with the focus point of this Gaussian beam at the origin. A microparticle moves straightly along the $X+$ direction. The moving trajectory of the center of the particle can have offsets in its Y and Z coordinates.

The detection of far-field scattering is along the red ray of polar angle θ and azimuth angle ϕ. Suppose that the offset of the particle center to beam center is (X, Y, Z). Then since the particle moves in $X+$ direction, we can directly map the X-scan result divided by particle velocity to the time-domain signal.

4.1.1 An Approximation using 2-Dimensional Settings

To give a conceptual demonstration, let us first analyze the 2-dimensional approximation. As illustrated in Figure 10, the particle still moves in $X+$ direction and the incident light still propagates along the $Z+$ direction. The beam get focused in the X direction with focused point at the origin, and is considered to be homogeneous in the Y direction.

4.1.1.1 Plane-Wave Expansion of an Incident Gaussian Beam

The incident Gaussian beam is expanded by plane waves of different wave vectors $\vec{K}$ in the following way.

Let D be a constant with arbitrary unit and let $G(\theta) = \cos\theta \exp(-D\sin^2\theta) = \cos\theta G'(\theta)$, which is indeed a Gaussian function. Consider $G(\theta)$ as the amplitude of a plane wave propagating in the directions of a polar angle θ. Suppose all the

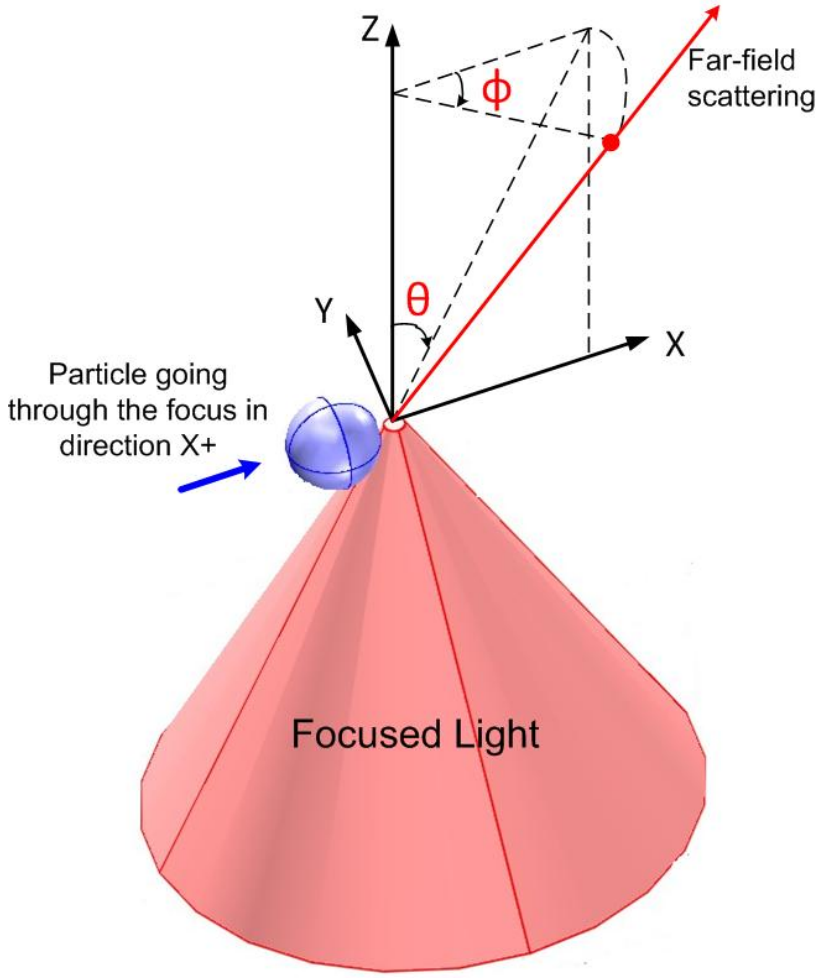

Figure 9: Schematic of a microparticle passing through a focused light beam. The direction of the particle movement is $X+$. The detection of scattering is along the red ray (θ, ϕ).

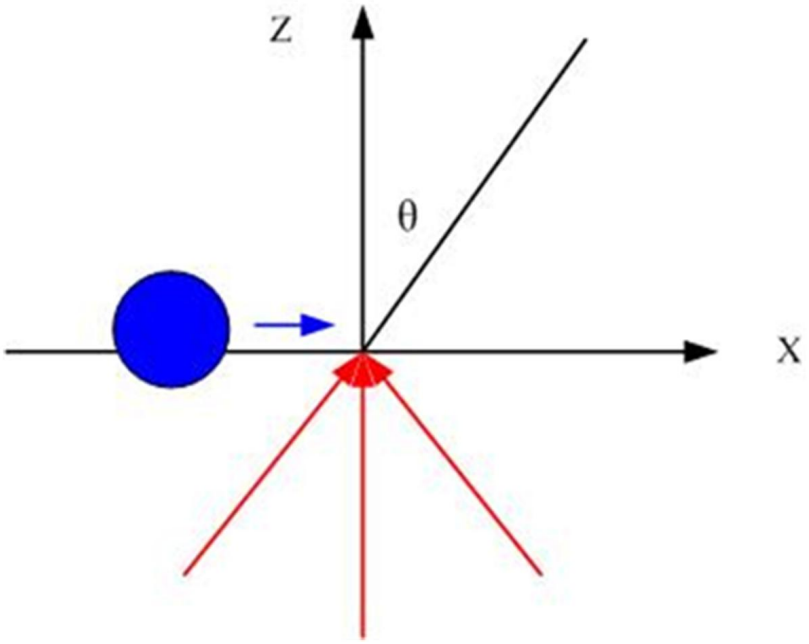

Figure 10: Schematic of a microparticle passing through a focused light beam in the 2D setting.

plane waves have phase 0 at the origin and polarization in the Y direction. Then the composition of all these plane waves is a Gaussian beam focused at the origin of the coordinate system and propagating in the $Z+$ direction. Several functions $G(\theta)$ (which are called θ-spectrum functions) of different values of D (called waist factor) are shown in the Figure 11. The amplitude at position (x, z) of the incident Gaussian beam is computed as

$$E_{\text{in}} = \int_{-\pi/2}^{\pi/2} G(\theta) \exp(ik(\sin\theta \cdot x + \cos\theta \cdot z))d\theta, \tag{15}$$

As shown in Figure 11, when the waist factor D is small ($D = 2$ for example), the θ-spectrum of the Gaussian beam is broad, which actually means that the beam is tightly focused with a small focused waist. When the constant D is larger ($D = 200$ for example), the spectrum is much sharper, which means the beam is relatively loosely focused and performs more like a plane wave.

As illustrated in Figure 12, when $D = 2$, the Gaussian beam is tightly focused

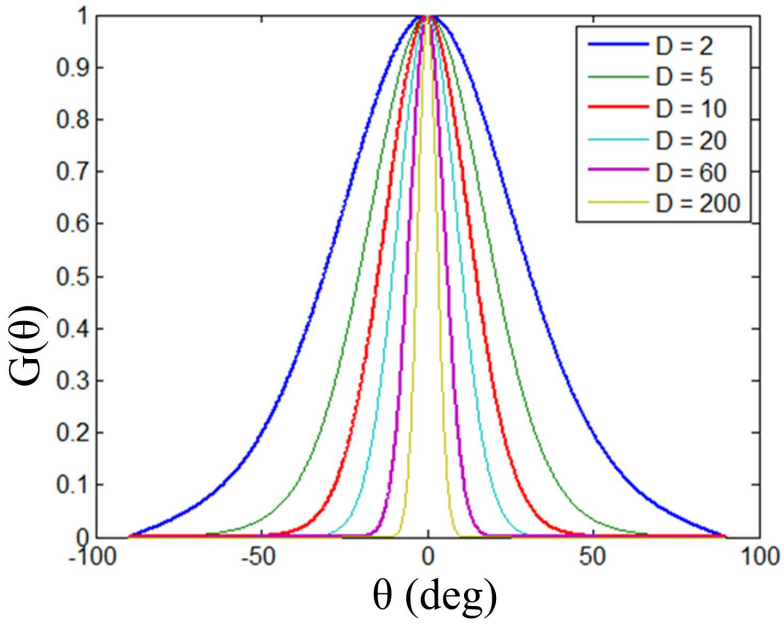

Figure 11: θ-spectrum functions $G(\theta)$ of different waist factors D.

with a waist of about 1 μm which is close to diffraction limit ($\lambda = 633$ nm).

In Figure 12, the waist factor D changes to 60, and the waist of the beam is about 4 μm.

In sum, a small waist factor means a tightly focused beam with small beam waist, and a large waist factor means a loosely focused beam with large beam waist.

4.1.1.2 An Approximation to the Scattering Functions

As discussed in details in Section 2.1, the Mie formulation is based on two scattering functions $S_1(\theta)$ and $S_2(\theta)$ with respect to two polarizations (θ is the scattering angle defined as the angle between the incident vector and the scattering vector).

In this section, I will demonstrate the features of the two scattering functions for particles with different size and refractive index parameters, and show that the scattering functions are quite similar to each other at small angles.

a) The diameter of the particle is 10 μm. The relative index m is 1.59/1.33. (Notice that 1.59 is the refractive index of polystyrene and 1.33 is the refractive index

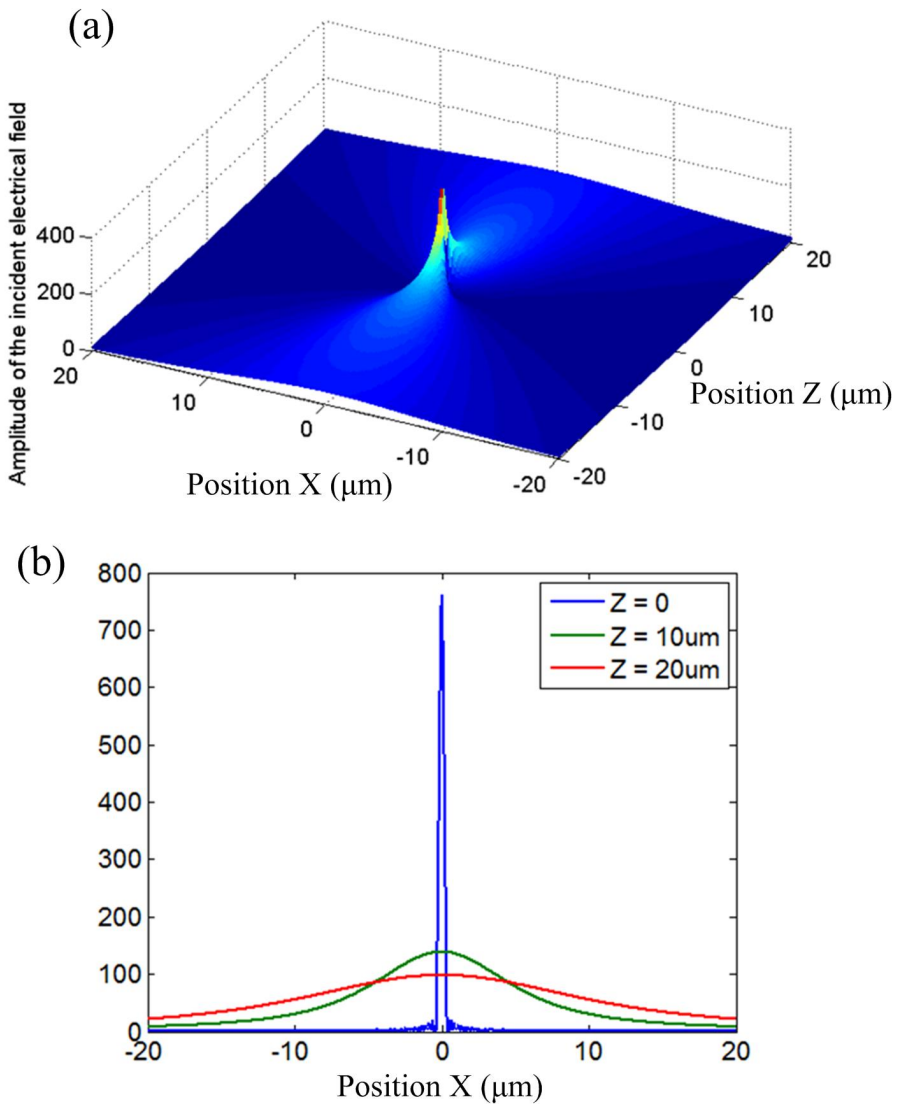

Figure 12: (a) The amplitude function of the electric field profile of a focused Gaussian beam with respect to position (x, z). (b) Curves of amplitude of E-field for different values of position z (slices of (a)). The waist factor D is 2. The wavelength of the beam is 633 nm.

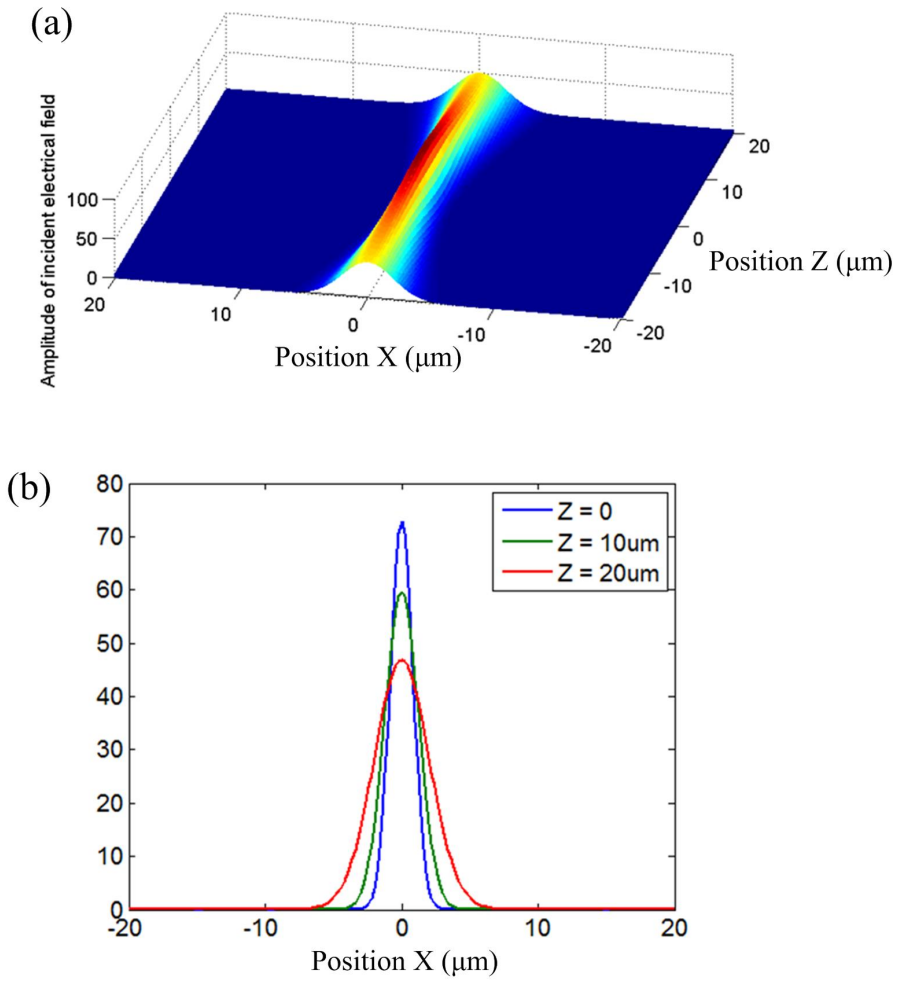

Figure 13: (a) The amplitude function of the electric field profile of a focused Gaussian beam with respect to position (x, z). (b) Curves of amplitude of E-field for different values of position z (slices of (a)). The waist factor D is 60. The wavelength of the beam is 633 nm.

of water.)

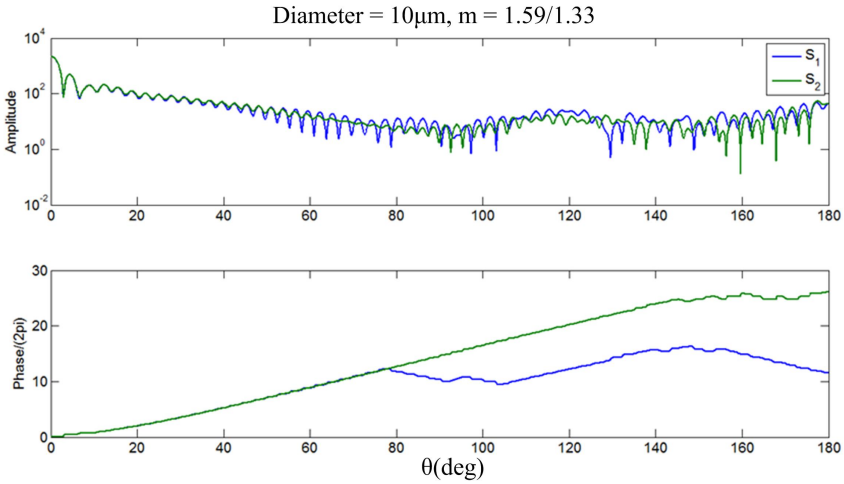

Figure 14: Amplitude and phase for scattering functions S_1 and S_2 of a dielectric particle with diameter 10 μm and index 1.59/1.33 relative to the ambient medium.

Figure 14 shows the amplitude and phase of the scattering functions. There are some ripples in the amplitude curves. (Recall that conventionally elastic light scattering techniques usually involve intensity measurements of these ripples.) In particular, one can notice that S_1 and S_2 are almost identical when θ is less than 40°.

To examine the complex scattering functions more, Figure 15 shows the real and imaginary parts of $S_1(\theta)$ and $S_2(\theta)$. The oscillations happen to both the real part and imaginary part. When θ is not very small, an approximation of a scattering function can be written as $R(\theta)\cos(\omega\theta) + iI(\theta)\cos(\omega\theta + \varphi)$ where $R(\theta)$ and $I(\theta)$ are decreasing amplitude functions. (Note that our time domain signals will be able to capture the complex scattering functions, not just its amplitude.)

b) The diameter of the particle is 10 μm. The relative index is 1.05.

The complex scattering functions are shown in Figure 16. The difference from a) is that the relative refractive index changes to a smaller value. One can observe that $R(\theta)$ and $I(\theta)$ decreases more quickly than in (a) as θ increases.

c) The diameter of the particle is 1 μm. The relative index is 1.59/1.33.

In this case, a smaller particle of diameter 1 μm is consider as the scatterer, and

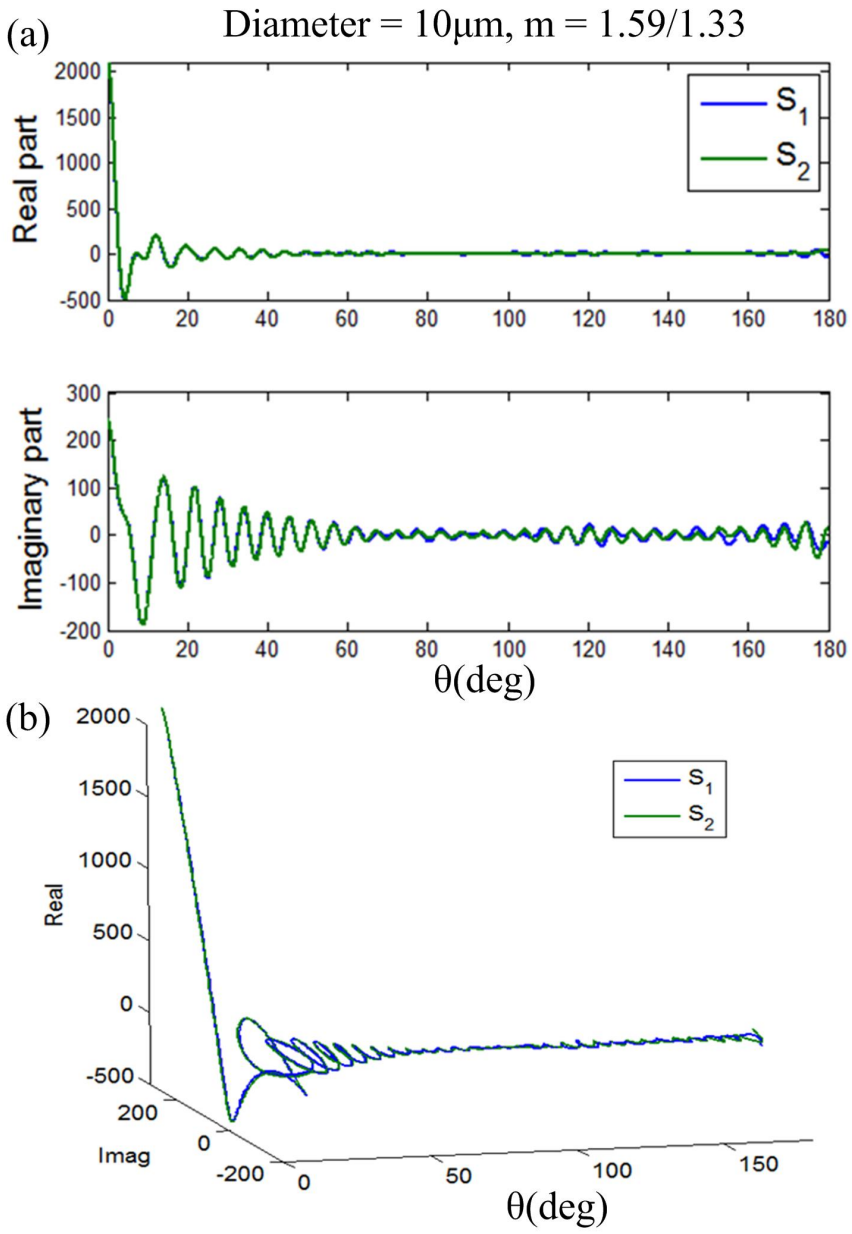

Figure 15: (a) Real and imaginary parts of the scattering functions S_1 and S_2 of a dielectric particle with diameter 10 μm and index 1.59/1.33 relative to the ambient medium. (b) The corresponding 3D plot.

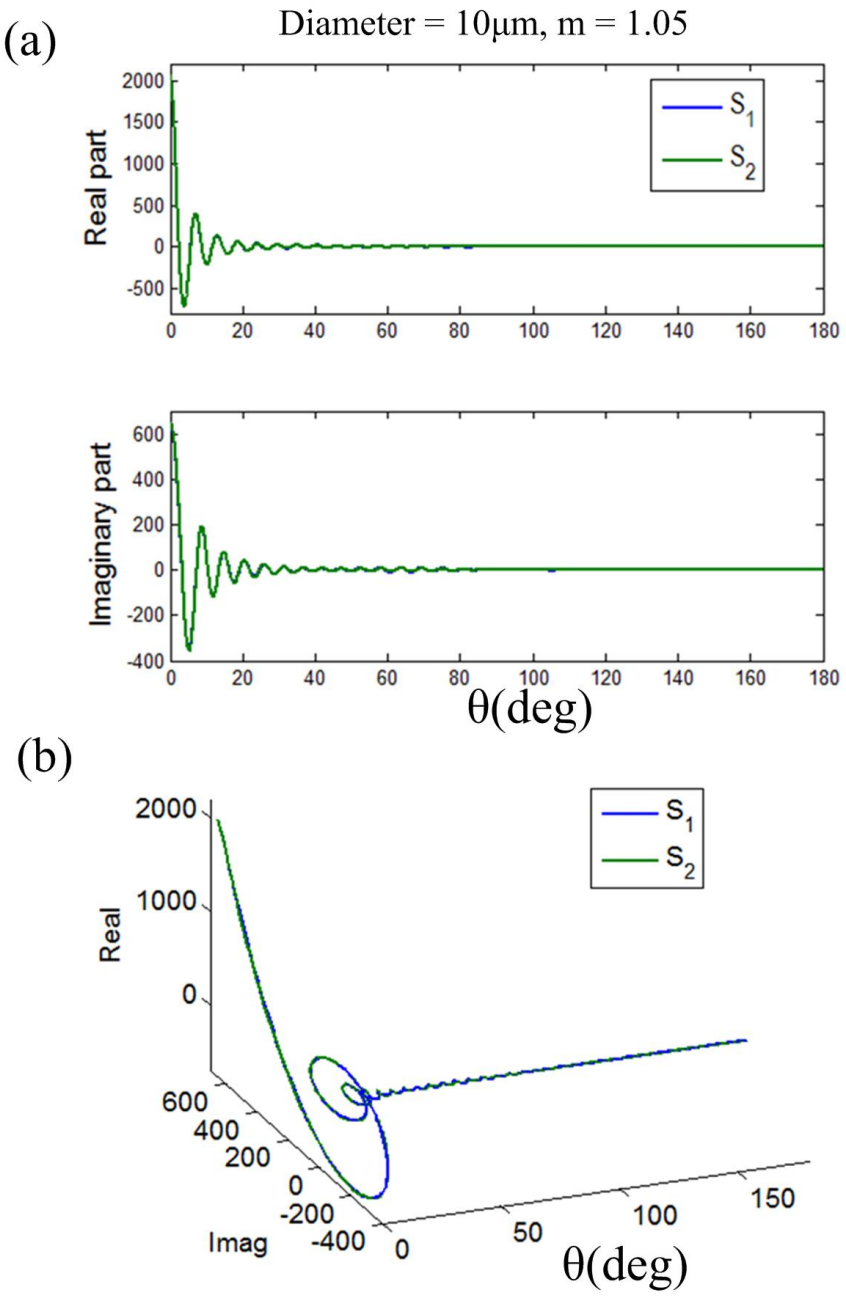

Figure 16: (a) Real and imaginary parts of the scattering functions S_1 and S_2 of a dielectric particle with diameter 10 μm and index 1.05 relative to the ambient medium. (b) The corresponding 3D plot.

the scattering functions are shown in Figure 17. Compare to case (a), the amplitude of the scattering functions decreases and the oscillation feature becomes slower.

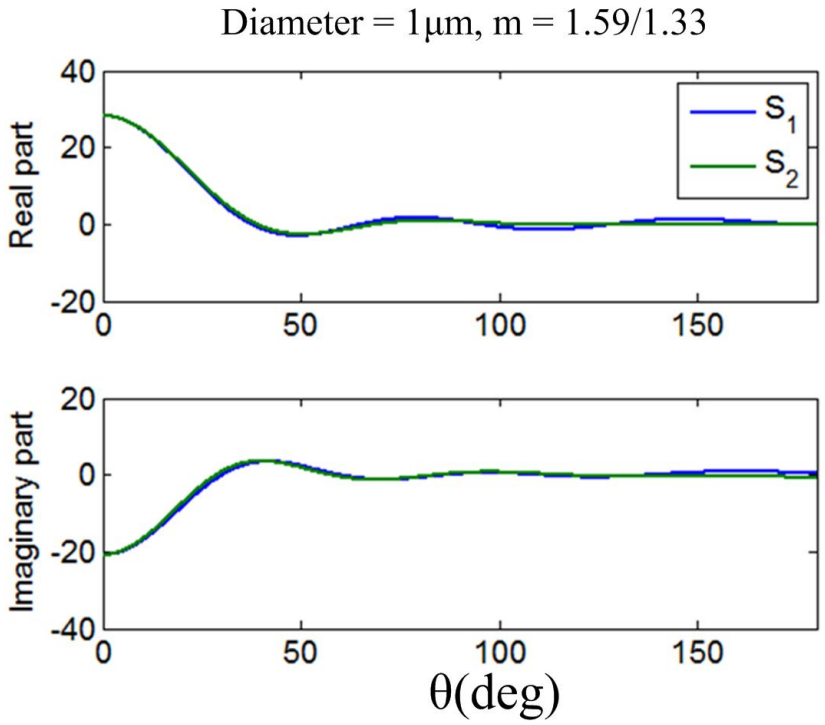

Figure 17: Real and imaginary parts of the scattering functions S_1 and S_2 of a dielectric particle with diameter $1\,\mu$m and index 1.59/1.33 relative to the ambient medium.

d) Core-shell structure. The diameter of the core particle is 1um with relative index 1.59/1.33 (refer to case (c)). The diameter of shell particle is 10um with relative index 1.05 (refer to case (b)). One can actually observe that the scattering cross section of c) is very small compared to b).

Here I just plot the amplitude of S_1 of the core-shell structure and of the pure 10um particle with relative index 1.05 as in b). They are quite similar to each other, which means the scattering from the inside 1um core just provide a fluctuation term.

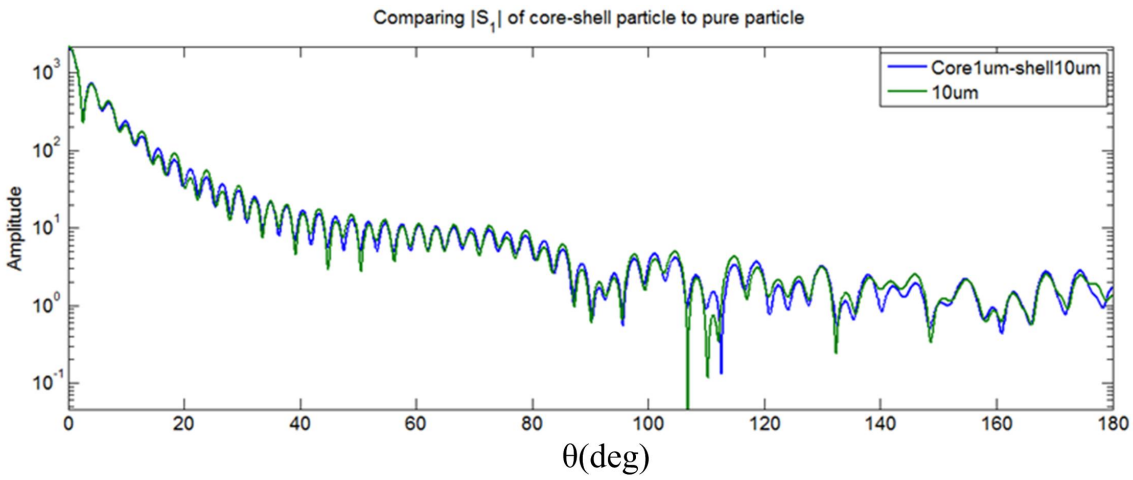

Figure 18: The amplitude of the scattering function S_1 for a core-shell structure (a core of diameter $1\,\mu$m and refractive index 1.59/1.33 and a shell of diameter $10\,\mu$m and refractive index 1.05) and for a pure $10\,\mu$m particle with refractive index 1.05.

4.1.1.3 Time-Domain Signals Perform as Fourier Transforms of the Scattering Function

First recall that the time domain scattering signal is equivalent to the X-offset signal. So here we actually analyze the X-offset (the displacement of the center of the particle and the focus center of the incident Gaussian beam) signal.

Let (X, Z) be the displacement of the particle center to the Gaussian beam center. Let θ_{out} be the output angle of signal detection direction. Then the detected scattering signal is a function of X, Z and θ_{out} in the following way.

$$A(X, Z, \theta_{\text{out}}) = \int G(\theta) S(\theta_{\text{out}} - \theta) \exp(i(\overrightarrow{K}_{\text{in}} - \overrightarrow{K}_{\text{out}})[X, Z]^t) d\theta \tag{16}$$

$$= \int G(\theta) S(\theta_{\text{out}} - \theta) \exp(ik(X(\sin\theta - \sin\theta_{\text{out}}) + Z(\cos\theta - \cos\theta_{\text{out}}))) d\theta. \tag{17}$$

As we are most interested in the X-offset signal, we can fix Z and θ_{out} as constant

parameters. Then

$$A_{Z,\theta_{\text{out}}}(X) = \int \frac{G(\theta)}{\cos\theta} \exp(ikZ(\cos\theta - \cos\theta_{\text{out}}))S(\theta_{\text{out}} - \theta) \tag{18}$$

$$\exp(ikX(\sin\theta - \sin\theta_{\text{out}}))\cos\theta d\theta \tag{19}$$

$$= \int W_{Z,\theta_{\text{out}}}(\theta)S(\theta_{\text{out}} - \theta)\exp(ikX(\sin\theta - \sin\theta_{\text{out}}))d(\sin\theta), \tag{20}$$

where

$$W_{Z,\theta_{\text{out}}}(\theta) = \frac{G(\theta)}{\cos\theta}\exp(ikZ(\cos\theta - \cos\theta_{\text{out}})).$$

This means that the detected signal $A(X)$ can be considered as the Fourier transform of the multiple of the scattering function $S(\theta)$ and a window function $W(\theta)$ (somehow shifted) which is closely related to the profile $G(\theta)$ of the Gaussian beam. (From $\sin\theta$-domain to X-domain, or approximately from θ-domain to X-domain when θ is small.) Note that θ_{out} determines how much we shift the window function. This actually means, depending on θ_{out}, we shift the window function to different parts of the scattering function, and then do Fourier transform.

This 1-dimensional Fourier transform approximation works quite well when $Z = 0$. In this case, $W_{0,\theta_{\text{out}}}(\theta) = \frac{G(\theta)}{\cos\theta}$ is purely real, which means it is more reasonable to consider it as a window function. Although our detection is 1-dimensional, it is necessary to analyze the 2-dimensional case to get the big picture on how the scattering signals should be. Let's get back to the equation

$$A_{\theta_{\text{out}}}(X, Z) \tag{21}$$

$$= \int G(\theta)S(\theta_{\text{out}} - \theta)\exp(ik(X(\sin\theta - \sin\theta_{\text{out}}) + Z(\cos\theta - \cos\theta_{\text{out}})))d\theta \tag{22}$$

$$= \exp(-ik(X\sin\theta_{\text{out}} + Z\cos\theta_{\text{out}}))\int G(\theta)S(\theta_{\text{out}} - \theta)\exp(ik(X\sin\theta + Z\cos\theta))d\theta. \tag{23}$$

The term $\exp(-ik(X\sin\theta_{\text{out}} + Z\cos\theta_{\text{out}}))$ won't be able to be detected by the measurement, since the actual detected signal is the intensity $|A_{\theta_{\text{out}}}(X, Z)|^2$.

Recall that the amplitude at (x, z) of the incident Gaussian beam is

$$E_{\text{in}}(x, z) = \int_{-\pi/2}^{\pi/2} G(\theta) \exp(ik(x \sin\theta + z \cos\theta)) d\theta,$$

and we already know what the field distribution should look like. The above two equations are somehow similar to each other, even though $A_{\theta_{\text{out}}}(X, Z)$ has variables (X, Z) as the displacement of the center of the particle to the center of the incident light focus and $E_{\text{in}}(x, z)$ has variables (x, z) as the actual spatial position. The term $S(\theta_{\text{out}} - \theta)$ is functional on $G(\theta)$.

Now let us consider the scattering from $10\,\mu$m particle with relative index 1.05. Since the scattering functions S_1 and S_2 are almost identical (Figure 16), our computation will use S_2 as the scattering function.

a) $\theta_{\text{out}} = 60^\circ$

For a moderately focused incident Gaussian beam ($D = 20$) as shown in Figure 19(a) (light yellow the window represents the expand of $G(\theta)$), we may somehow model the complex scattering function around θ_{out} as

$$S(\theta_{\text{out}} - \theta) \sim R(\theta) \cos(\omega\theta) + i \cdot I(\theta) \cos(\omega\theta + \varphi),$$

where $R(\theta)$ and $I(\theta)$ are the envelop functions for the real and imaginary parts. (They are real functions themselves.)

A more conceptual way is to write it down as

$$S(\theta_{\text{out}} - \theta) \sim C(\theta) e^{i\omega\theta} + D(\theta) e^{-i\omega\theta}.$$

Now $C(\theta)$ and $D(\theta)$ are complex envelop functions. Thus

$$G(\theta) S(\theta_{\text{out}} - \theta) \sim G(\theta) C(\theta) e^{i\omega\theta} + G(\theta) D(\theta) e^{-i\omega\theta}.$$

Note that phase shift in θ-domain will result in the spatial shift in the (X, Z)-domain. This actually means that we get a split of the input Gaussian beam into two Gaussian beams in the (X, Z)-domain and the detected signal at polar angle θ_{out} with

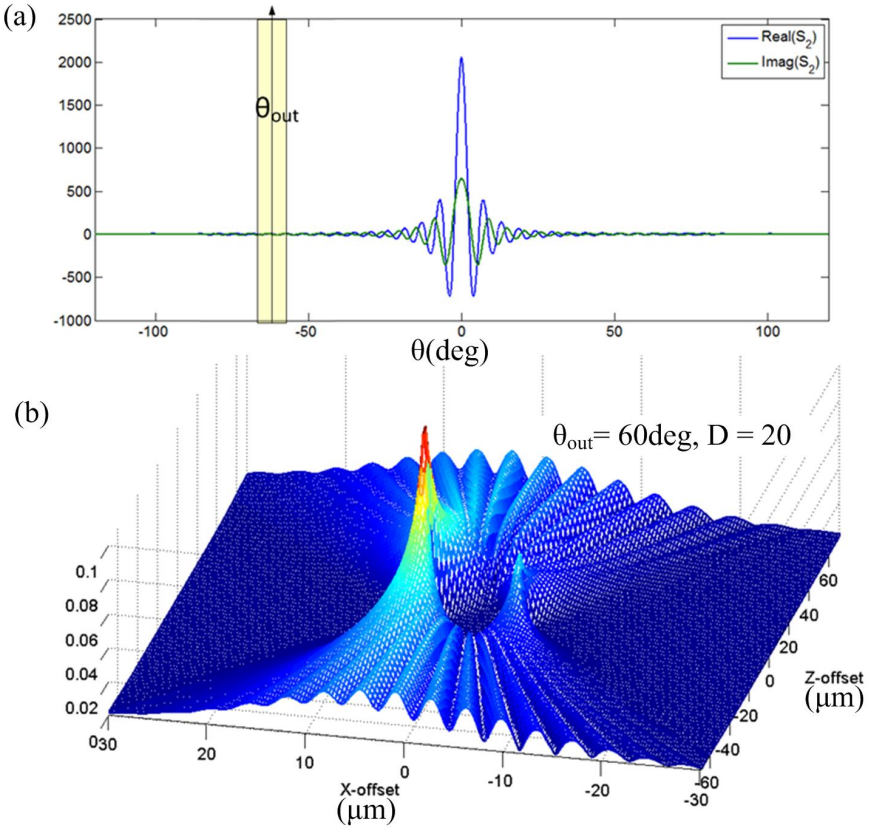

Figure 19: (a) The real and imaginary parts of the scattering function S_2 for particle with diameter $10\,\mu$m and refractive index 1.05. The window illustrated in yellow is derived from the θ-spectrum of the incident beam with waist factor $D = 20$ and the detection angle $\theta_{\text{out}} = 60°$. (b) The 3D plot of the corresponding scattering signal $|A(X, Z)|$.

respect to the X-offset and Z-offset has a pattern looking like the interference of these two Gaussian beams. The two split Gaussian beams may have different amplitudes according to $C(\theta)$ and $D(\theta)$. One can also observe that the two split Gaussian beams has a distance in X-offset of about $10\,\mu$m, the diameter of the particle. Recall that the time-domain signal comes from the X-offset of the particle to the origin of the coordinate. Therefore, the actual signal in measurement is the slice of the pattern $|A_{\theta_{\text{out}}}(X, Z)|$ in Figure 19(b) with a fixed Z-offset of the particle trajectory

Now let $D = 200$, which means the incident light is loosely focused. Then the window performed by $G(\theta)$ is narrower.

Now let $D = 2$, which means the incident light is tightly focused. Then the window performed by $G(\theta)$ is much wider, and the simple approximation

$$S(\theta_{\text{out}} - \theta) \sim C(\theta)e^{i\omega\theta} + D(\theta)e^{-i\omega\theta}$$

is not very precise in this case.

(b)$\theta_{\text{out}} = 0$

This is the case of forward scattering. Still we set different values for the focus constant D of the incident light and get the following figures of scattering amplitudes for moderately, loosely and tightly focused incident beams respectively. They somehow reflect the Fourier transform of $S(\theta)$ into (X, Z)-domain. As a result, the scattering signal $|A(X, Z)|$ looks like an interference pattern from two balanced Gaussian beams with a split distance in X-offset about $10\,\mu$m, i.e., the diameter of the particle.

4.1.2 Analysis in 3-Dimensional Settings

Now let us consider the realistic case of 3D settings. Then the incident Gaussian beam propagates in the $Z+$-direction and get focused in the X and Y directions. For simplicity, we also suppose the incident light is unpolarized and since the two scattering functions S_1 and S_2 are quite close to each other, we can use a scalar assumption of the electric field and choose either S_1 or S_2 as the scalar scattering

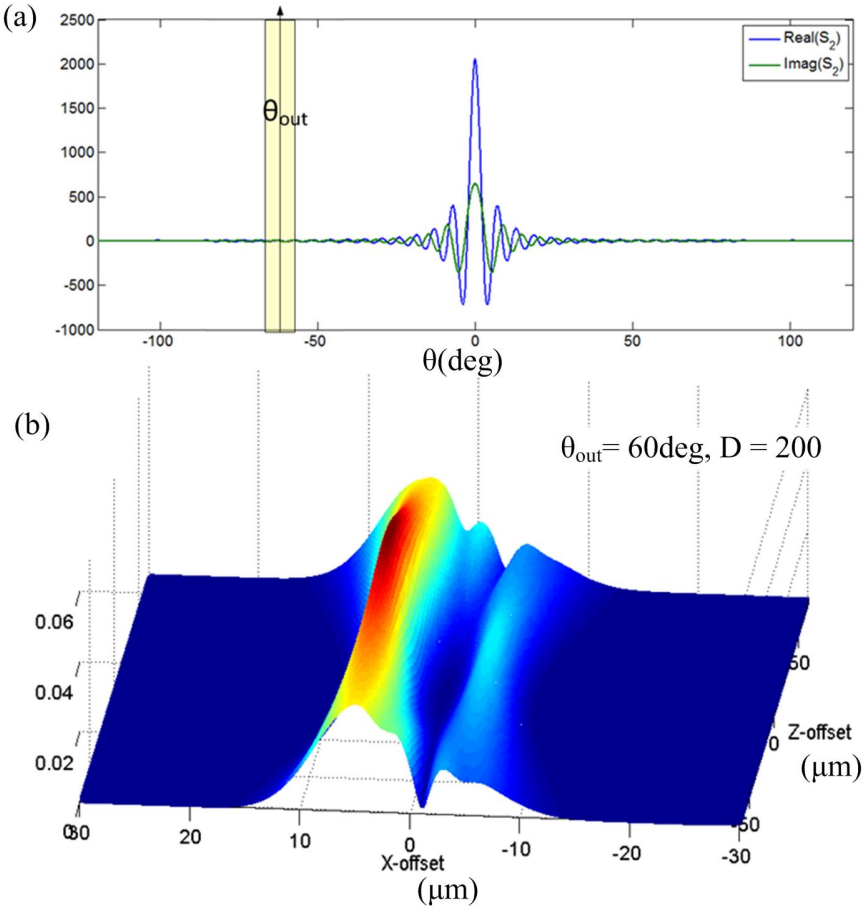

Figure 20: (a) The real and imaginary parts of the scattering function S_2 for particle with diameter $10\,\mu$m and refractive index 1.05. The window illustrated in yellow is derived from the θ-spectrum of the incident beam with waist factor $D = 200$ and the detection angle $\theta_{\text{out}} = 60°$. (b) The 3D plot of the corresponding scattering signal $|A(X, Z)|$.

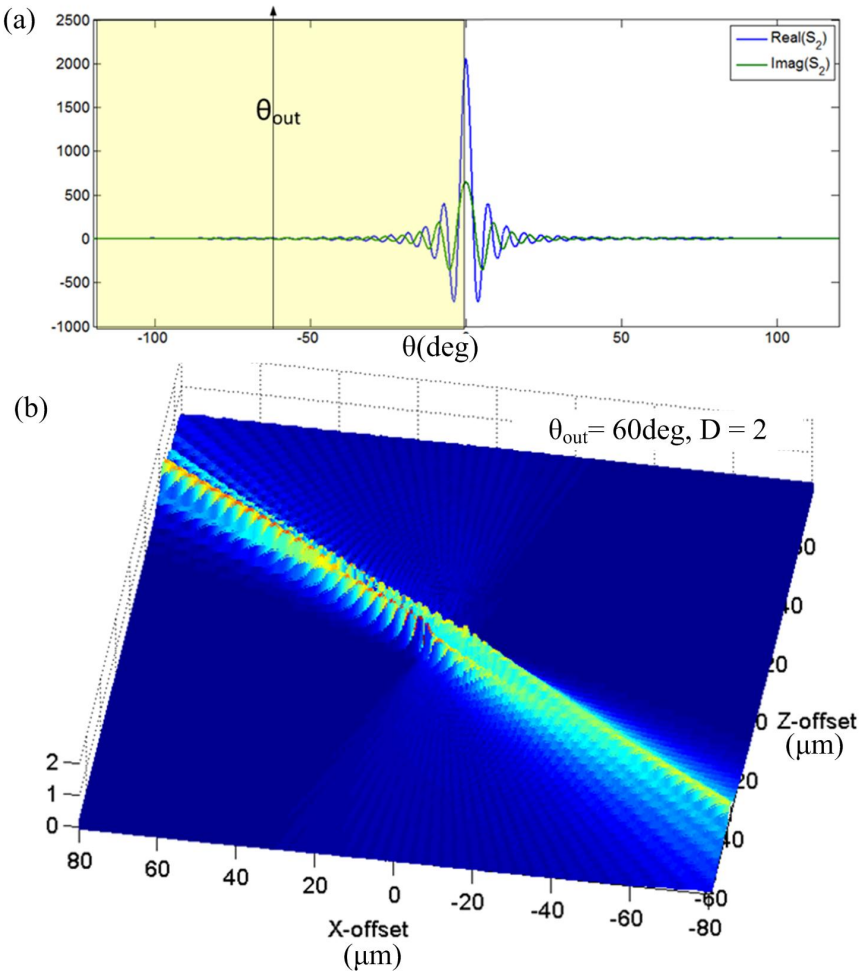

Figure 21: (a) The real and imaginary parts of the scattering function S_2 for particle with diameter $10\,\mu$m and refractive index 1.05. The window illustrated in yellow is derived from the θ-spectrum of the incident beam with waist factor $D = 2$ and the detection angle $\theta_{\text{out}} = 60^\circ$. (b) The 3D plot of the corresponding scattering signal $|A(X, Z)|$.

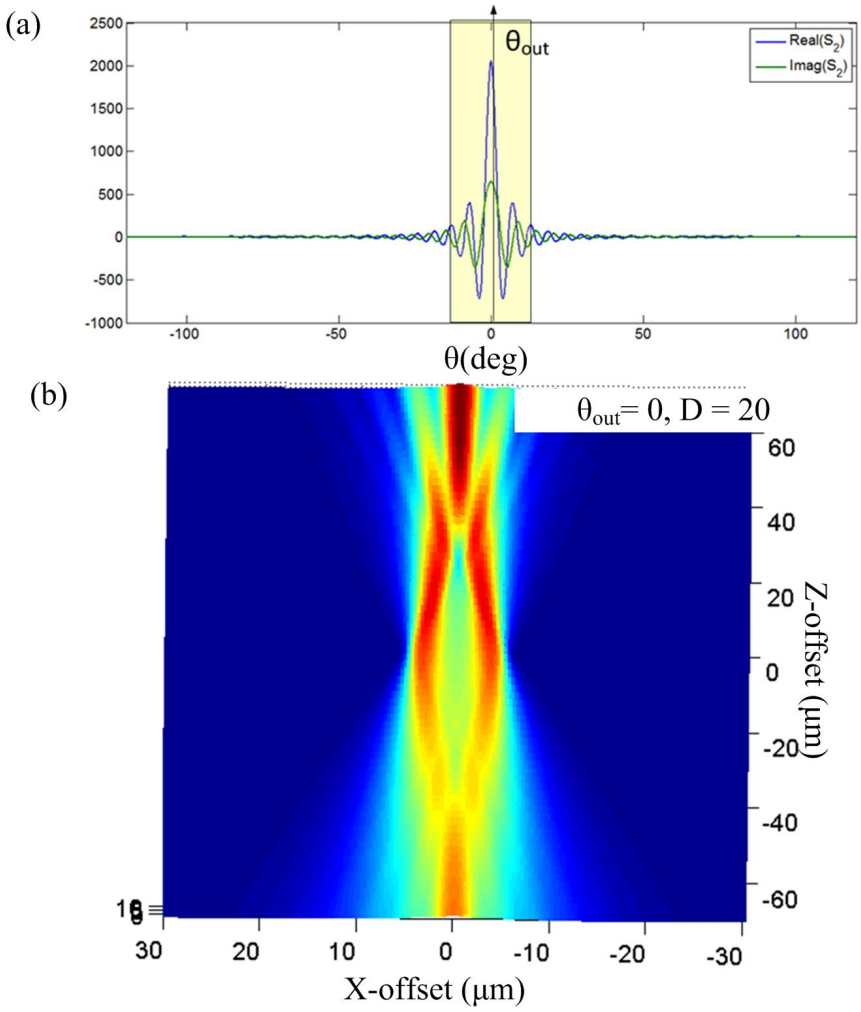

Figure 22: (a) The real and imaginary parts of the scattering function S_2 for particle with diameter $10\,\mu$m and refractive index 1.05. The window illustrated in yellow is derived from the θ-spectrum of the incident beam with waist factor $D = 20$ and the detection angle $\theta_{\text{out}} = 0$. (b) The corresponding scattering signal $|A(X, Z)|$.

function.

Therefore, the scattering signal in direction $(\theta_{\text{out}}, \phi_{\text{out}})$ for a particle with displacement (X, Y, Z) from the origin of the coordinates is formulated as follows:

$$A(X, Y, Z, \theta_{\text{out}}, \phi_{\text{out}}) =$$
$$\iint G(\theta) S(\alpha(\overrightarrow{K}_{\text{out}} - \overrightarrow{K}_{\text{in}})) \exp(i(\overrightarrow{K}_{\text{in}}(\theta, \phi) - \overrightarrow{K}_{\text{out}}(\theta_{\text{out}}, \phi_{\text{out}}))[X, Y, Z]^t) d\theta d\phi.$$

Here $\overrightarrow{K}_{\text{in}}(\theta, \phi) = k \cdot [\sin\theta \cos\phi, \sin\theta \sin\phi, \cos\theta]$,
$\overrightarrow{K}_{\text{out}}(\theta_{\text{out}}, \phi_{\text{out}}) = k \cdot [\sin_{\text{out}} \theta_{\text{out}} \cos_{\text{out}} \phi_{\text{out}}, \sin_{\text{out}} \theta_{\text{out}} \sin_{\text{out}} \phi_{\text{out}}, \cos_{\text{out}} \theta_{\text{out}}]$ and $\alpha(\overrightarrow{K}_{\text{out}} - \overrightarrow{K}_{\text{in}})$ is the angle between $\overrightarrow{K}_{\text{out}}$ and $\overrightarrow{K}_{\text{in}}$.

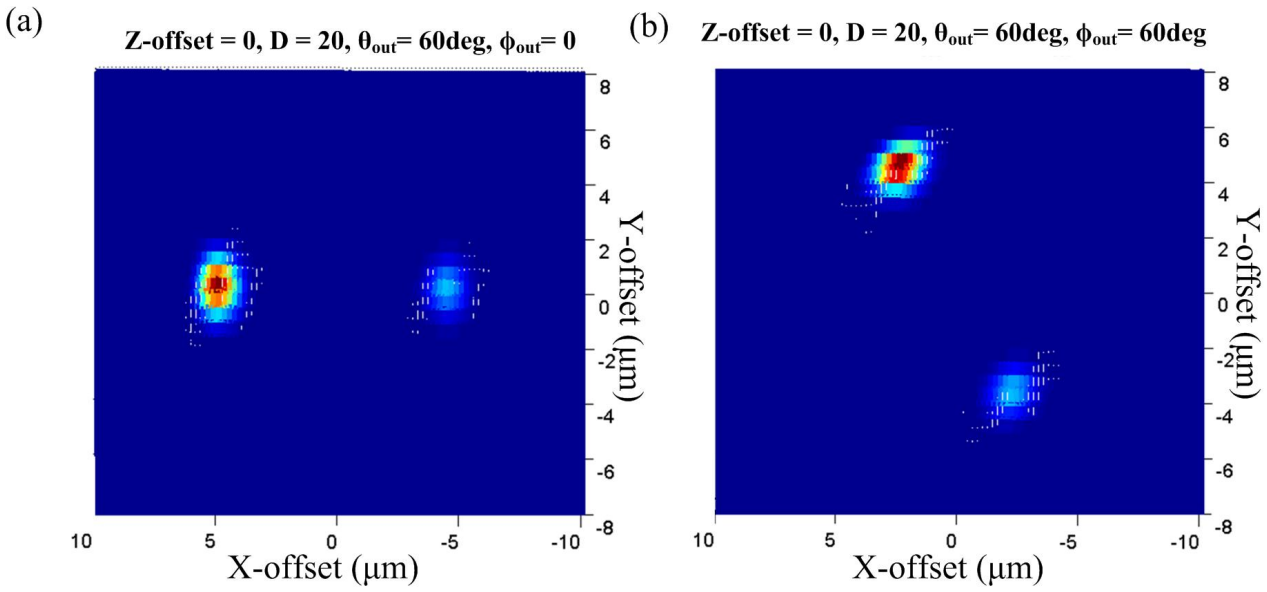

Figure 23: The scattering signals $|(A(X, Y, Z)|$ for a particle of diameter $10\,\mu$m and refractive index 1.05 at $Z = 0$. (a) The detection direction $(\theta_{\text{out}}, \phi_{\text{out}})$ is $(60°, 0)$. (b)The detection direction $(\theta_{\text{out}}, \phi_{\text{out}})$ is $(60°, 60°)$.

Again, we assume the scattering particle has diameter $10\,\mu$m and refractive index 1.05. Figure 23 shows the scattering signals in the detection direction $(\theta_{\text{out}}, \phi_{\text{out}})$ of $(60°, 0)$ and $(60°, 60°)$ when the Z-offset is 0. For each case, two bright spots of distance about $10\,\mu$m can be seen while one is stronger than the other. In addition, it can be observed that Figure 23(b) is actually a 60°rotation of Figure 23(a).

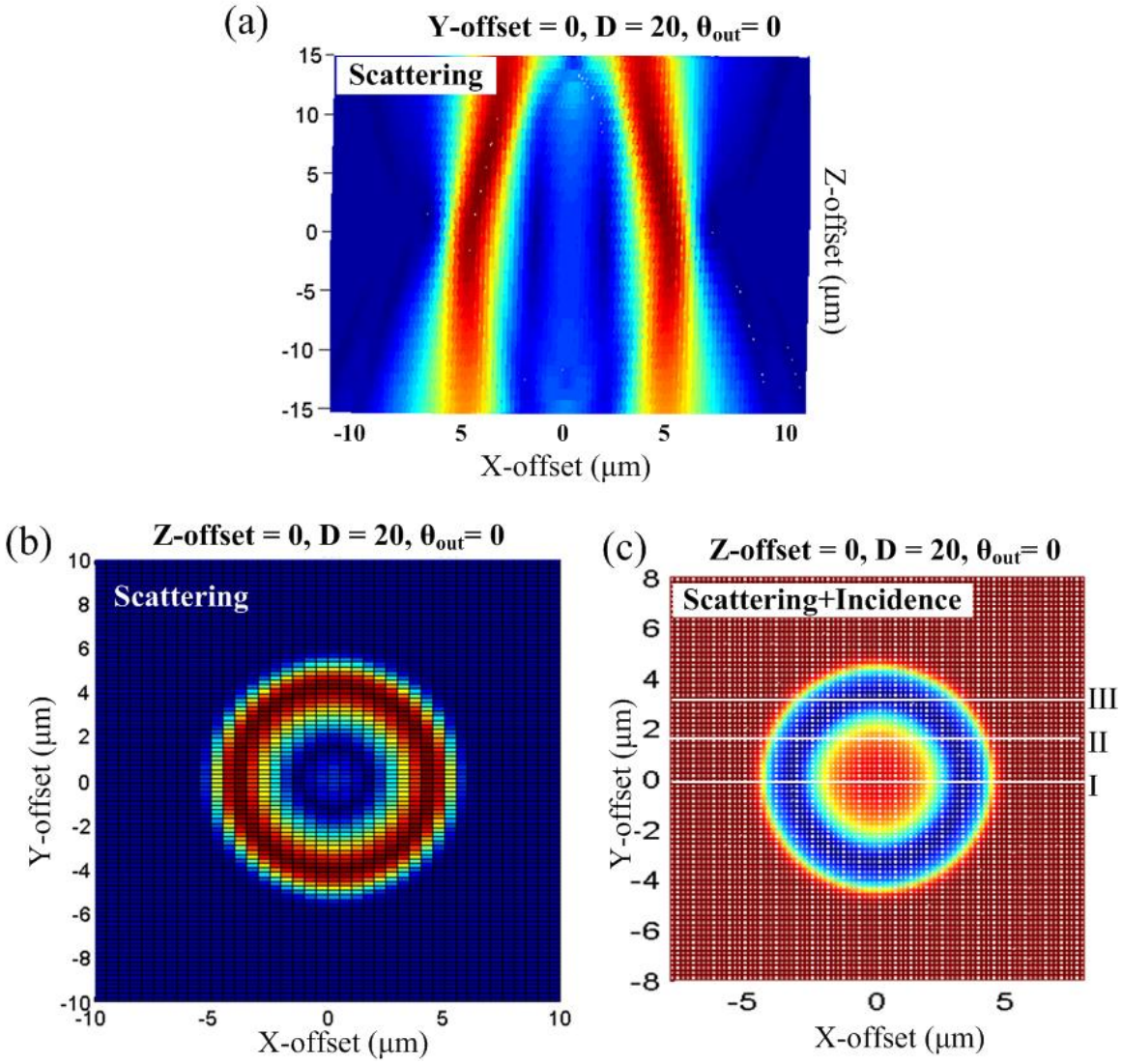

Figure 24: (a) The forward scattering ($\theta_{\text{out}} = 0$) signals $|A(X, Y, Z)|$ when Y-offset of the particle is 0. (b) The forward scattering signals $|A(X, Y, Z)|$ when Z-offset of the particle is 0. (c) The total signal at $\theta_{\text{out}} = 0$ which is the interference of the forward scattering and the incidence. The three white lines represent possible trajectory of the particle movement with different Y-offset. The scattering particle has diameter $10\,\mu$m and refractive index 1.05.

Now let us consider forward scattering with $\theta_{\text{out}} = 0$. As shown in Figure 24(a), the pattern of scattering signals with $Y = 0$ is analogous to the corresponding 2D case (Figure 22) with two peaks. If we assume the Z-offset is 0, then the pattern of scattering signal looks like a ring. The actual signal the photon detector can observe on FSC is actually the interference of the scattering with the incidence, as shown in Figure 24(c), whose pattern looks like the complement of the pattern in Figure 24(b). The three white lines I, II, and III are possible trajectories of the particle passing through the focus spot of the incident beam with different Y-offset. Therefore, when $Y = 0$ (line I), and two dips with separating distance about the size of the particle are expected to be observed in a time-domain measurement; when the Y-offset is a little larger ($\sim 2\,\mu$m line II), the separating distance becomes small; and when the Y-offset is much larger ($\sim 4\,\mu$m line III), one might only observe one dip in the time-domain detection.

4.2 Experimental Demonstration

An experimental measuring result of time-domain FSC and SSC derived from the MCARS flow cytometer [18] is shown in Figure 25.

There are two dips in the FSC curve and two peaks in the SSC curve. The two dips in the FSC curve have almost the same depth and width, while one peak is predominantly stronger than the other in the SSC curve. In addition, the distance between the two dips in the FSC curve is the same as the distance between the two peaks in the SSC curve. All these observations agree well with our theoretical expectations presented in the previous sections. Since the interval distance between the dips for FSC or peaks for SSC is linearly proportional to the particle size which is barely affected by the refractive index of the particle, an accurate time-of-flight morphological technique for focused-light flow cytometry can be developed based on this phenomenon.

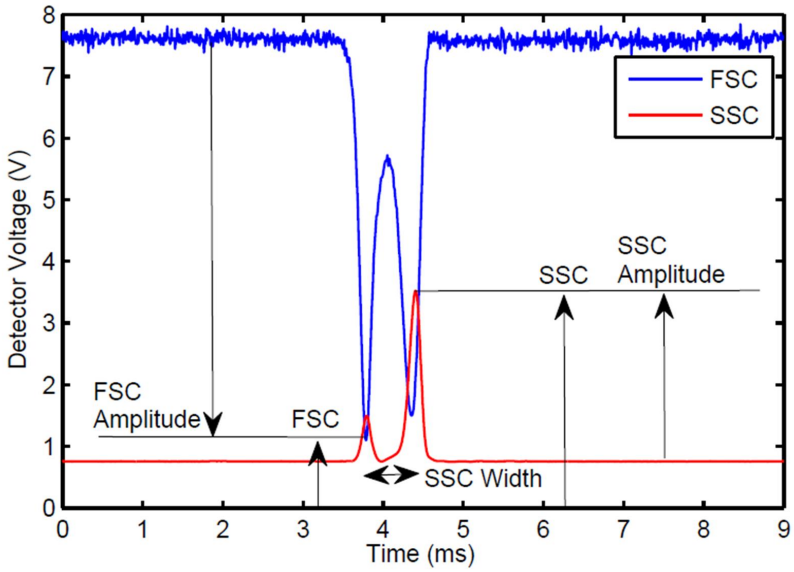

Figure 25: (Reproduced by the courtesy of Charles Camp Jr.) FSC (blue) and SSC (red) waveform recorded from two amplified silicon detectors. Arrows and labels identify various measurable parameters, such as FSC and SSC, FSC and SSC amplitude, and FSC and SSC (width) (N.B.: in this example SSC and FSC widths are the same; thus, the labeling of FSC width was neglected for pictorial clarity).

CHAPTER V

ULTRA-COMPACT ON-CHIP PLASMONIC LIGHT CONCENTRATION

In this section, I will demonstrate a novel ultra-compact on-chip plasmonic light concentrator (PLC) [45]. Some related techniques of plasmonic light concentration in the literature have been reviewed in Section 1.2.

5.1 Hybrid Photonic-Plasmonic Structures for Nano-Scale Light Concentration

The basic structure of the proposed PLC is a small triangle-shaped metal taper on top of a dielectric waveguide, as shown in Figure 26(a). In our analysis of this structure, the material for the metal triangle is gold (Au), and the material for the dielectric ridge waveguide is either silicon (Si) or silicon nitride (Si_3N_4). The substrate is silicon dioxide (SiO_2). In addition, a SiO_2 buffer layer is used to separate the metal triangle and the dielectric ridge waveguide. The ambient material is water or air. The dimensions of the ridge waveguide are chosen to support only the fundamental transverse magnetic (TM, vertical polarization) mode and the fundamental transverse electric (TE, horizontal polarization) mode. For the triange-shaped metal taper analyzed in this section, I only take use of the fundamental TM mode for the light input, while the fundamental TE mode will be considered for a dual structure which will be discussed in Section 5.4. I set up the coordinate system with X-axis in the horizontal direction, Y-axis in the vertical direction and Z-axis in the propagation direction of the input light.

Figure 26(b) shows the top view of the metal triangle, which is isosceles. I use the radius of curvature a at the tip to simulate how the tip of the triangle can be

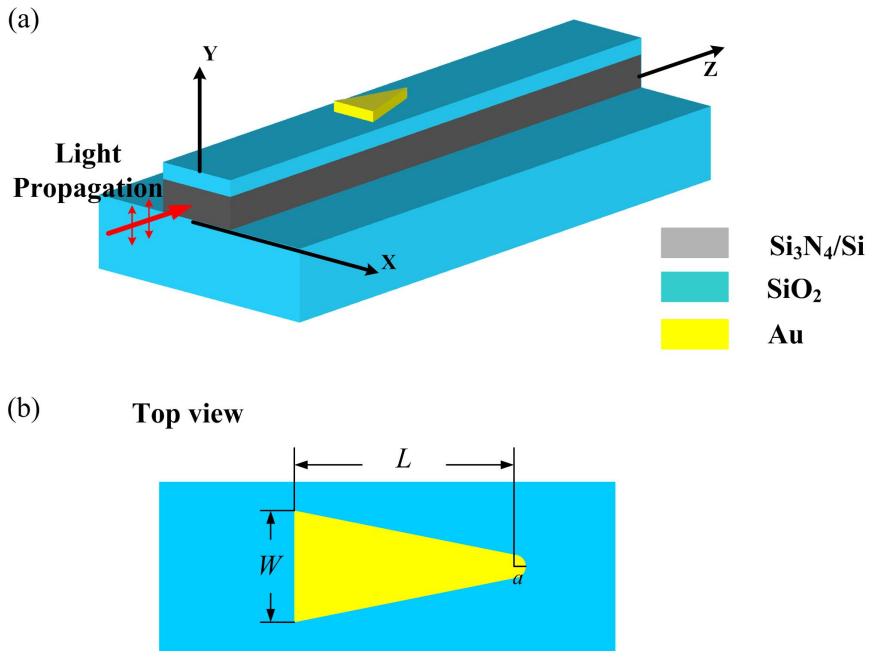

Figure 26: (a) Schematic of an ultra-compact PLC which is a hybrid dielectric-plasmonic structure with a gold triangle taper integrated on top of a dielectric (Si_3N_4 or Si) ridge waveguide with a SiO_2 buffer layer. (b) The top view of this hybrid structure.

rounded up in real fabrications. I use W to denote the length of the base of the isosceles triangle, and L to denote the the length of a perpendicular from the center of the curved tip to the middle point of the base side. In particular, I will call W the width of the triangle and L the length of the triangle throughout this proposal.

5.2 Hybrid Photonic-Plasmonic Waveguides

To analyze the behavior of this hybrid structure with the metal triangle on top, I first do mode analysis on a hybrid photonic-plamsmonic waveguide with a metal strip on top. Plasmonic waveguides [46–48] are waveguides that can guide SPP modes, which are usually in a metal-insulator-metal (MIM) profile or an insulator-metal-insulator (IMI) profile [49]. Hybrid photonic-plasmonic waveguides are waveguides that can guide supermodes which can be decomposed into plasmonic parts and photonic parts. Several different configurations of hybrid waveguides have been developed recently [50,

51]. The hybrid photonic-plasmonic waveguides we discuss in this section are specific to our settings.

As shown in Figure 27(a), the ridge waveguide is made of Si_3N_4 with dimensions of 620 nm in width and 200 nm in thickness. The thickness of the SiO_2 buffer layer is 100 nm. The Au strip has thickness of 40 nm and width of w. The ambient material is water. Assume the working wavelength λ is 800 nm. At this wavelength, the refractive index of Si_3N_4 is 2, the refractive index of SiO_2 is 1.46, the refractive index of water is 1.33, and the permittivity of Au is $-24.02 + j1.18$.

Here I study the supermodes in the hybrid waveguides by looking at possible mode couplings between the modes in the corresponding purely photonic waveguide (with the Au layer removed) and the modes in the corresponding purely plasmonic waveguide (having Si_3N_4 changed to SiO_2). Under the aforementioned dimensions, the purely photonic waveguide only support the fundamental quasi-TM mode (denoted by TM_0) and the fundamental quasi-TE mode (denoted by TE_0). The TM_0 mode can only couple with symmetric modes of the purely plasmonic waveguide, and the TE_0 mode can only couple with the asymmetric modes of the purely plasmonic waveguide. I only consider the fundamental symmetric (S_0) and asymmetric (A_0) modes of the purely plasmonic waveguide, since higher order modes are cut off with the dimensions of our structure at the wavelength λ of 800 nm. Figure 27(b) shows how two supermodes, $H_{TM,0}$ and $H_{TM,1}$, are derived from the superposition of the TM_0 mode and the S_0 mode. The electric field lines are sketched for these modes. Analogously, Figure 27(c) shows how two supermodes, $H_{TE,0}$ and $H_{TE,1}$, are derived from the superposition of the TE_0 mode and the A_0 mode.

To give more details about the mode-coupling processes, I use a COMSOL software to compute the eigenmodes at the wavelength λ of 800 nm based on finite element method (FEM). Note that the effective indices n_{eff} of the propagating modes must have real parts greater than 1.46, which is the refractive index of the SiO_2 substrate.

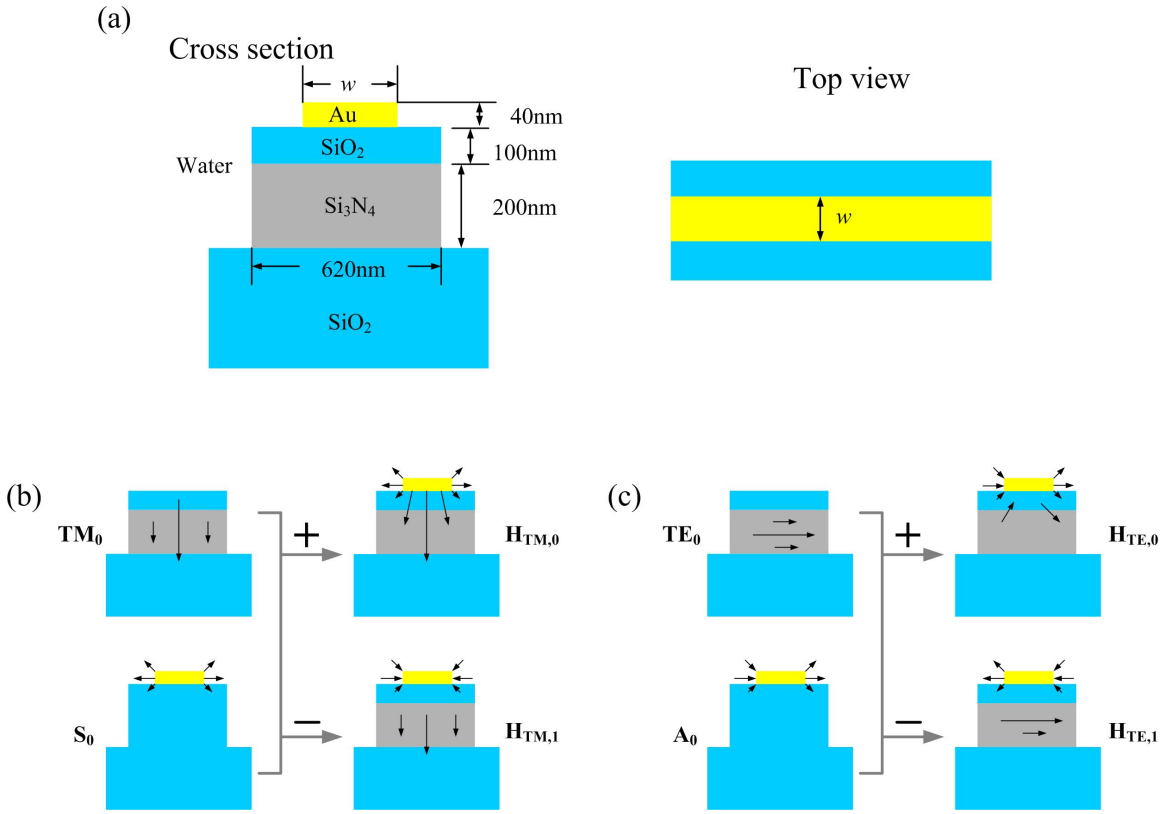

Figure 27: (a) The cross section and top view of a hybrid plasmonic-dielectric waveguide. (b) Two hybrid modes ($H_{TM,0}$ and $H_{TM,1}$) come from the superposition of the fundamental TM mode (TM_0) of the purely dielectric waveguide and the fundamental symmetric mode (S_0) of the purely plasmonic waveguide. (c) Two hybrid modes ($H_{TE,0}$ and $H_{TE,1}$) come from the superposition of the fundamental TE mode (TE_0) of the purely photonic waveguide and the fundamental asymmetric mode (A_0) of the purely plasmonic waveguide.

Figure 28 shows the normalized electric and magnetic mode profiles of TM_0, S_0, $H_{TM,0}$ and $H_{TM,1}$, with the width w of the Au strip set to 620 nm. The electric and magnetic field lines are plotted. This corresponds to the mode coupling process explained in Figure 27(b). The TM_0 mode has an effective index of $n_{\text{eff}} = 1.5696$, the S_0 mode has an effective index of $n_{\text{eff}} = 1.7302 + j0.0223$, the $H_{TM,0}$ mode has an effective index of $n_{\text{eff}} = 1.5743 + j0.0094$, and the $H_{TM,1}$ mode has an effective index of $n_{\text{eff}} = 1.7992 + j0.0163$.

Analogously, the related modes in Figure 27(c), TE_0, A_0, $H_{TE,0}$ and $H_{TE,1}$, are illustrated in Figure 29. The TE_0 mode has an effective index of $n_{\text{eff}} = 1.6533$, the A_0 mode has an effective index of $n_{\text{eff}} = 1.7088 + j0.0238$, the $H_{TE,0}$ mode has an effective index of $n_{\text{eff}} = 1.7512 + j0.0213$, and the $H_{TE,1}$ mode has an effective index of $n_{\text{eff}} = 1.6273 + j6.1 \times 10^{-4}$.

The dispersion of the four propagating supermodes ($H_{TM,0}$, $H_{TM,1}$, $H_{TE,0}$ and $H_{TE,1}$) is plotted in Figure 30 as the real and imaginary parts of the effective index versus the width w of the Au strip. The minimum of the coordinate of real(n_{eff}) is 1.46, which is the refractive index of the SiO_2 substrate. As I have mentioned, the real part of the effective index of a propagating mode must be greater than 1.46. Therefore, the $H_{TE,1}$ mode is cut off when $w < 180$ nm as shown in the figure. The imaginary part of the effective index accounts for the propagation loss.

The Real(n_{eff}) of $H_{TM,0}$ is greater than the Real(n_{eff}) of $H_{TM,1}$, and as w decreases, the difference becomes larger. The imaginary parts follows the same trend. This is because as w decreases, the light energy becomes more concentrated in the lossy metal region for $H_{TM,0}$, while the light energy becomes more concentrated in the dielectric region for $H_{TM,1}$. The mode profiles of both modes are illustrated in Figure 31, where $w = 60$ nm. When w approaches 0, both the real and imaginary parts of the effective index of $H_{TM,0}$ goes to infinity, which means that the phase velocity goes to 0 and $H_{TM,0}$ becomes more and more like a localized mode. When $w = 0$, the

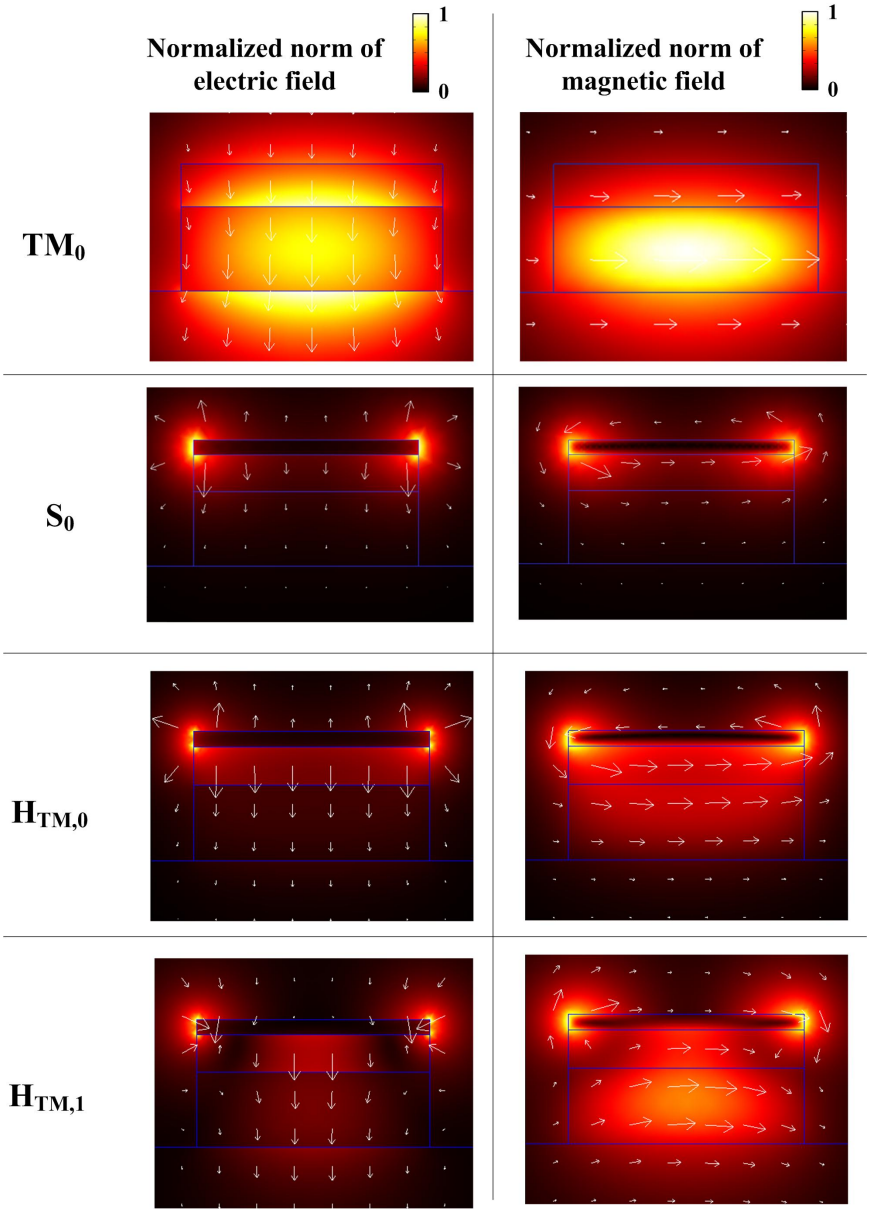

Figure 28: The normalized electric and magnetic mode profiles of TM_0, S_0, $H_{TM,0}$ and $H_{TM,1}$. The width w of the Au layer is 620 nm. The wavelength λ is 800 nm.

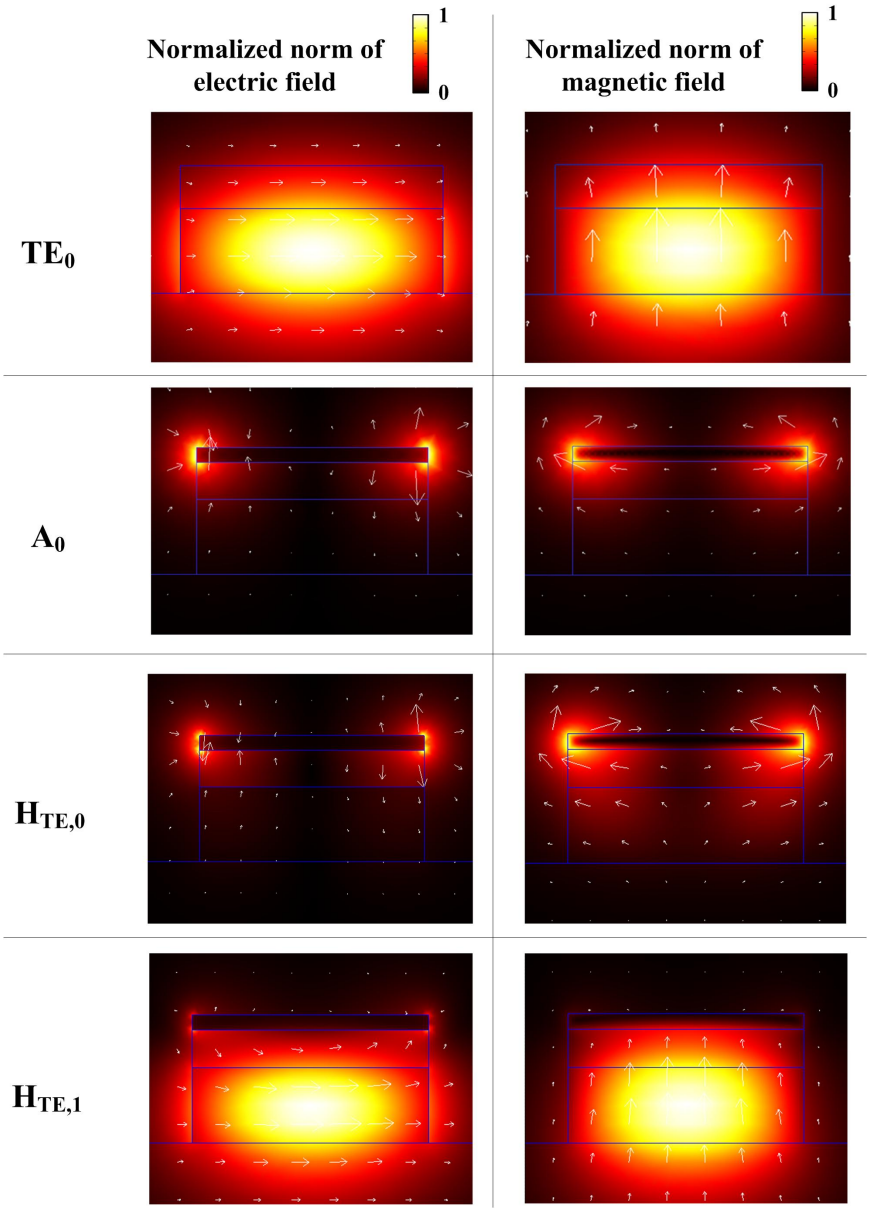

Figure 29: The normalized electric and magnetic mode profiles of TE_0, A_0, $H_{TE,0}$ and $H_{TE,1}$. The width w of the Au layer is 620 nm. The wavelength λ is 800 nm.

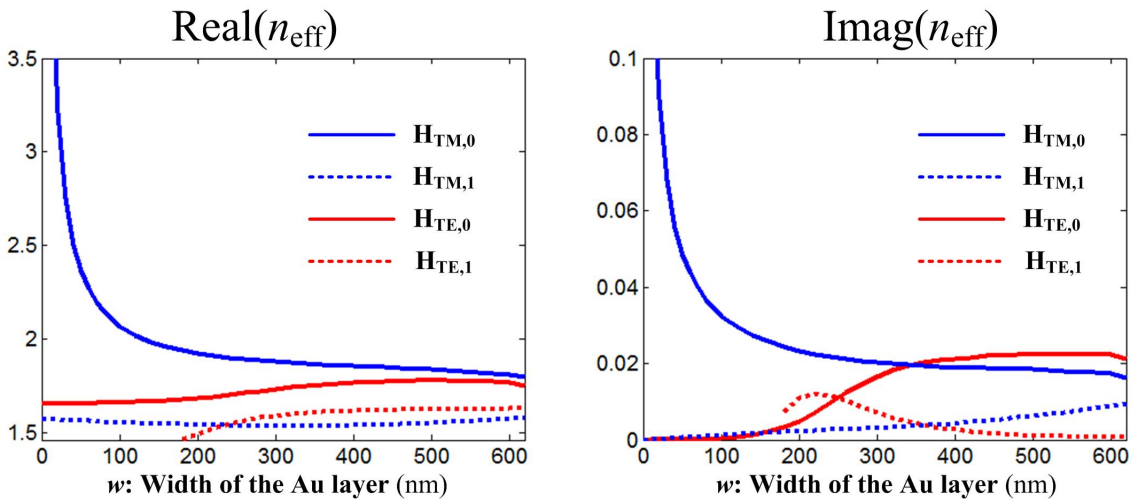

Figure 30: Dispersion characterization of the four supermodes ($H_{TM,0}$, $H_{TM,1}$, $H_{TE,0}$ and $H_{TE,1}$) with respect to the width w of the Au strip. The wavelength λ is 800 nm.

metal strip vanishes and the $H_{TM,1}$ mode is actually the purely photonic mode TM_0. Note that localization of propagating modes is one of the main mechanisms in our triangle-shaped PLCs.

Using the same method of analysis, I can see that the $H_{TE,0}$ mode evolves into the purely photonic mode TE_0 as w approaches 0. When $w < 180$ nm, the $H_{TE,1}$ mode is cut off. This is the reason that I can not take use of the supermodes $H_{TE,0}$ and $H_{TE,1}$ in our application of light concentration based on triangle-shaped metal tapers. The $H_{TE,0}$ mode has its applications in a dual structure, as will be discussed in Section 5.4.

The supermodes in the hybrid waveguide can be excited by the modes in the corresponding bare (or purely photonic) waveguide. More specifically, the incident mode TM_0 in the bare waveguide can excite two supermodes ($H_{TM,0}$ and $H_{TM,1}$) of the hybrid waveguide. The superposition of these two supermodes at the input end should have the light energy more concentrated in the dielectric region to match the incident TM_0 mode. Since they have different effective indices, as can be seen from the dispersion diagram in Figure 30, the two supermodes undergo a beat effect with light energy bouncing back and forth between the dielectric region and the metal

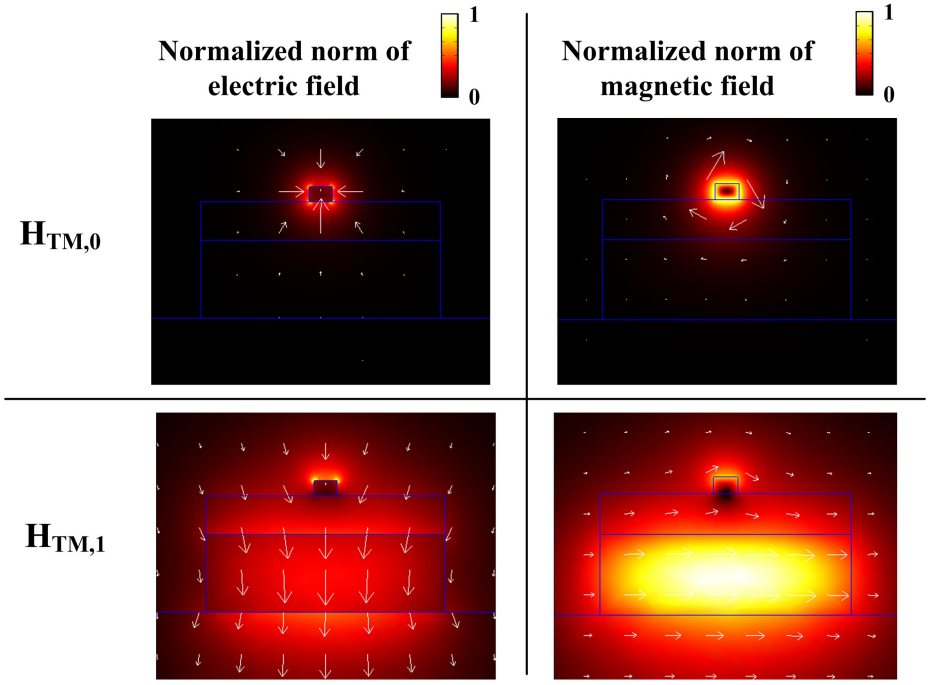

Figure 31: The normalized electric and magnetic mode profiles of $H_{TM,0}$ and $H_{TM,1}$. The width w of the Au strip is 60 nm. The wavelength λ is 800 nm.

region. For a specific width w of the Au strip, we have

$$\mathrm{BL}(w) = \frac{\lambda}{\mathrm{Real}(n_{\mathrm{eff}}(\mathrm{H}_{\mathrm{TM},0}(w)) - n_{\mathrm{eff}}(\mathrm{H}_{\mathrm{TM},1}(w)))}, \tag{24}$$

where $\mathrm{BL}(w)$ is the beat length. In particular, at a distance equal to half of the beat length from the input end, the light energy is coupled mainly into the metal region.

5.3 Silicon-Nitride-based Plasmonic Light Concentrators

The ultra-compact PLCs introduced in Section 5.1 take use of three effects: mode beat, nanofocusing and weak resonance. The efficiency of a PLC depends on the interplay among the three effects. I will demonstrate these effects by analyzing the performance of a Si_3N_4-based PLC, which is a triangle-shaped Au taper integrated on a Si_3N_4 ridge waveguide.

For the dielectric part, I use the same size parameters as in Section 5.2: the Si_3N_4 ridge of width 620 nm and thickness 200 nm, and the SiO_2 buffer of width 620 nm and thickness 100 nm. The thickness of the Au triangle is 40 nm. The ambient material

is also water. The coordinate system is set up as in Figure 26. In particular, the coordinate origin is chosen such that the plane $X = 0$ cuts through the middle of the Si_3N_4 ridge vertically, the plane $Y = 0$ coincides with the boundary between the Si_3N_4 layer and the SiO_2 substrate, and the plane $Z = 0$ goes through the center of the curved tip.

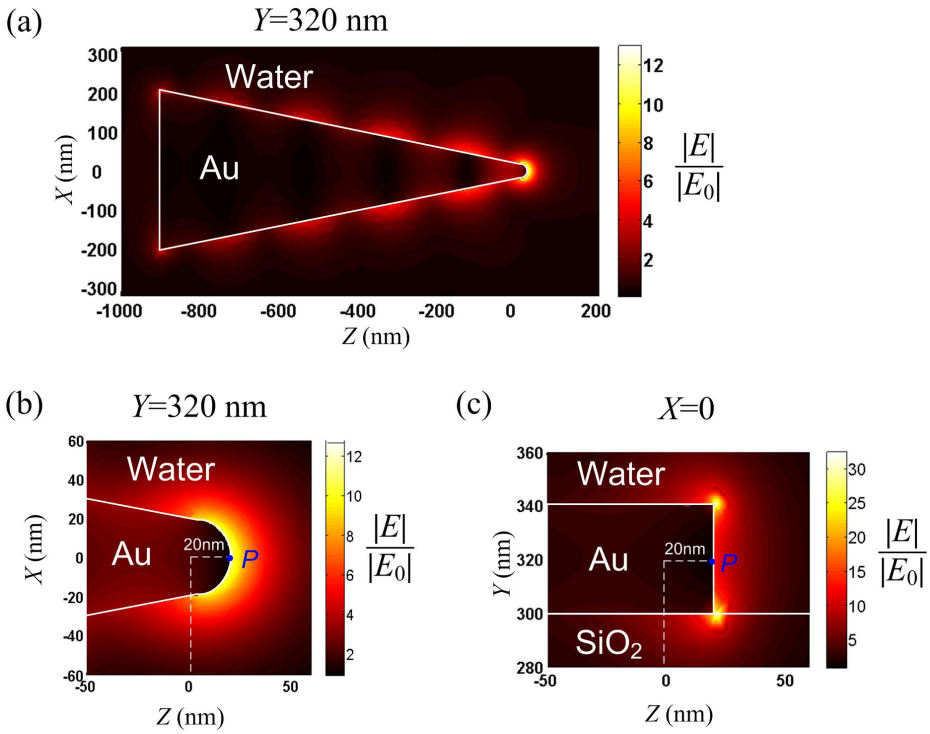

Figure 32: Normalized electric field patterns in the planes horizontally ($Y = 320\,\text{nm}$) and vertically ($X = 0$) cutting through the Au layer. The length L of the Au triangle is 900 nm, and the width W is 400 nm. The FCF is 12.6 with he radius of curvature a at the tip being 20 nm.

As shown in Figure 32, I compute the electric field patterns in the horizontal ($Y = 320\,\text{nm}$ in (a) and (b)) and vertical planes ($X = 0$ in (c)) using a 3D FEM simulation (COMSOL Multiphysics). Here $Y = 200\,\text{nm} + 100\,\text{nm} + 20\,\text{nm}$, which comes from the sum of the thickness of the Si_3N_4 layer, the thickness of the SiO_2 buffer layer and half of the thickness of the Au layer. The Au triangle has dimensions of $L = 900\,\text{nm}$, $W = 400\,\text{nm}$ and $a = 20\,\text{nm}$.

Let $|E_0|$ be the average norm of the incident electric field in the Si_3N_4 region,

which is calculated from the corresponding bare waveguide (the Au layer is removed). Only the TM_0 mode (vertical polarization) is carried in this bare waveguide. Let us consider a cross-section plane D of the bare waveguide. Since the bare waveguide is homogeneous in Z direction, I can simply choose A as the plane $Z = 0$ without lose of generality. Note that D extends to infinity in both X and Y direction, while I reduce the actual calculation within a bounded region. Let P_A denote the total power flow through A. Then I have

$$P_A = \int_D \bar{\mathbf{S}}_z = \int_D \mathrm{Re}(\frac{1}{2}(\mathbf{E} \times \mathbf{H}^*)_z) = \frac{n_{\mathrm{Si_3N_4}}}{2\eta_0}|E_0|^2 A_{\mathrm{Si_3N_4}}, \tag{25}$$

where $\bar{\mathbf{S}}$ is the time-averaged Pynting vector, $\eta_0 = \sqrt{\mu_0/\epsilon_0} \approx 120\pi$ is the wave impedance of free space, $n_{\mathrm{Si_3N_4}}$ is the refractive index of Si_3N_4, and $A_{\mathrm{Si_3N_4}}$ is the area of the cross section of the Si_3N_4 slab. Note that $n_{\mathrm{Si_3N_4}} = 2$ and $A_{\mathrm{Si_3N_4}} = 620\,\mathrm{nm} \times 200\,\mathrm{nm}$ with our choice of parameters. This equality assumes that the total power flow through D is evaluated by a plane-wave approximation with the electric field E_0 homogeneously distributed within the Si_3N_4 region. Therefore, E_0 represents what I call "the average electric field in the bare waveguide" and its norm can be computed by the formula

$$|E_0| = \sqrt{\frac{2\eta_0}{n_{\mathrm{Si_3N_4}} A_{\mathrm{Si_3N_4}}} \int_D \bar{\mathbf{S}}_z}. \tag{26}$$

The electric field patterns shown in Figure 32 are normalized to $|E_0|$. The light field becomes highly concentrated at the metallic tip. To evaluate the field concentration induced by the PLC, I introduce a field concentration factor (FCF) as the normalized electric field norm at the apex point (point P in Figure 32 (b) and (c)) in the horizontal plane cutting through the Au layer. In particular, the FCF is 12.6 in this case. Note that the FCF depends on the radius of curvature a. While reducing a can afford higher FCF, I need to choose a large enough for a good estimation on real fabrications. Here I let $a = 20\,\mathrm{nm}$, and write $\mathrm{FCF}(a = 20\,\mathrm{nm}) = 12.6$.

As mentioned above, the field concentration is governed by three effects: mode

beat, nanofocusing and weak resonance. I have analyzed in Section 5.2 that the incident mode TM_0 in the bare photonic waveguide can excite two supermodes, $H_{TM,0}$ and $H_{TM,1}$, in the corresponding hybrid waveguide with a metal (Au) strip integrated on top. The triangle-shaped PLC can be considered as a taper with the width w of the Au strip gradually going down to 0. Therefore, I can still use the two supermodes for the Au taper in our analysis. The mode beat between the two supermodes can transfer light energy quickly from the dielectric region to the metal region, and the triangle taper performs plasmonic nanofocusing at the same time. A certain amount of the light energy will be reflected at the tip. Thus I will also see some resonance. This weak resonance also affects how much energy can be concentrated into the tip. By adjusting the size parameters of the Au taper, I can coordinate the three effects and optimize the efficiency of the PLC.

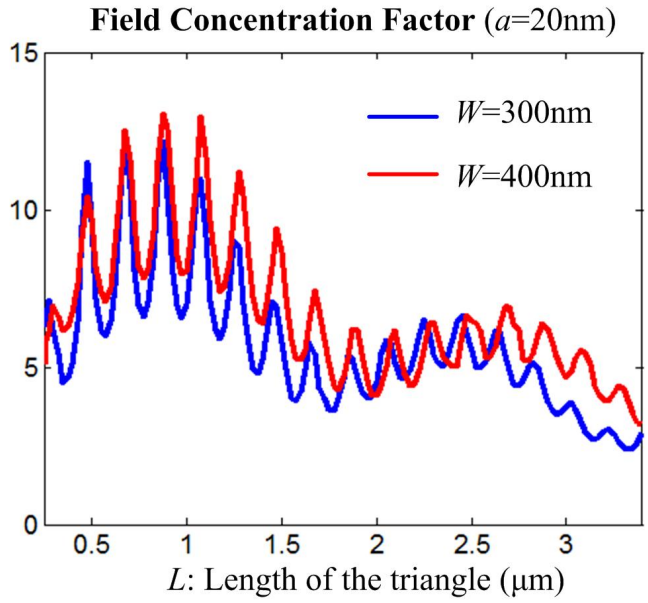

Figure 33: FCF vs Length L of the Au triangle. The width W is 300 nm for the blue curve and 400 nm for the red curve. The wavelength λ is 800 nm. The radius of curvature a at the tip is 20 nm.

Figure 33 shows how the FCF varies with respect to the length L of the Au triangle, while the radius of curvature a is always assumed to be 20 nm. The wavelength λ is

800 nm. The blue curve is for $W = 300\,\text{nm}$, and the red curve is for $W = 400\,\text{nm}$. These curves are composed of two oscillatory parts, the slow variations corresponding to the mode-beat effect and the ripples of high oscillation frequency corresponding to the resonance effect. Both of them can be clearly seen from the figure.

I use Equation (24) to estimate the beat length for this triangular structure, where w is set to be $W/2$ which is about the average width of the triangle. For the blue curve, I have $W = 300\,\text{nm}$ and $w = 150\,\text{nm}$. Therefore, the real part of $n_{\text{eff}}(\text{H}_{\text{TM},0}(150\,\text{nm}))$ is 1.9694, and of $n_{\text{eff}}(\text{H}_{\text{TM},1}(150\,\text{nm}))$ is 1.5475 from Figure 30. By Equation (24),

$$\text{BL}(150\,\text{nm}) = \frac{800\,\text{nm}}{1.9694 - 1.5475} = 1896\,\text{nm}\,.$$

Analyzing analogously on the $W = 400\,\text{nm}$ case (the red curve), I get $w = 200\,\text{nm}$, $\text{Real}(n_{\text{eff}}(\text{H}_{\text{TM},0}(200\,\text{nm}))) = 1.9216$, $\text{Real}(n_{\text{eff}}(\text{H}_{\text{TM},1}(200\,\text{nm}))) = 1.5413$, and $\text{BL}(200\,\text{nm}) = 2104\,\text{nm}$. Note that the beat length for the $W = 400\,\text{nm}$ case is a little bit larger than the beat length of the $W = 300\,\text{nm}$ case. The beat lengths can also be estimated from the figure by approximately locating the the first minimums of slow variation parts. These two methods of beat-length estimations agree with each other very well. It is quite convenient to use the first method for a real design, because the second method is a lot more time-consuming and lacks numerical accuracy. When L is about half of the beat length, the light energy transfers from the dielectric region to the metal region most efficiently, which results in a higher FCF, as can be seen from the figure. This is actually a principle of design. More precisely, the tapering evolution also induces energy coupling between the two supermodes, which is different from the case for hybrid waveguides. In other words, the ratio of energy stored in the two modes will change at different locations along the metal taper. Moreover, only the $\text{H}_{\text{TM},0}$ mode becomes localized as the metallic tip.

The ripples on the curves come from to the resonance effect. Although the structure is not resonance-based, the resonance effect inevitably kicks in and affects the efficiency of our structure adequately. To calculate the free spectral range (FSR), I

should only consider the effective index of the $H_{TM,0}$ mode. The formula is

$$\mathrm{FSR}(w) = \frac{\lambda}{2\mathrm{Real}(n_{\mathrm{eff}}(H_{TM,0}(w)))}. \tag{27}$$

For example, in the case of $W = 400\,\mathrm{nm}$, I have $w = 200\,\mathrm{nm}$, $\mathrm{Real}(n_{\mathrm{eff}}(H_{TM,0}(200\,\mathrm{nm}))) = 1.9216$, and $\mathrm{FSR}(200\,\mathrm{nm}) = 208\,\mathrm{nm}$. This corresponds to about 15 peaks for the red curve, a good matching with an actual counting on the figure. The FCF is usually the highest, when L is chosen to be at a resonance peak close to half of the beat length. Moreover, L can be further reduced to make the PLC supercompact, while still get a high FCF. For example, the FCF is still larger than 10 with $L = 500\,\mathrm{nm}$ for both curves.

I also use the finite difference time domain (FDTD) analysis to do simulations for the structure. Figure 34 shows the spectra of transmission, reflection and transmission+reflection for (a) $L = 1\,\mu\mathrm{m}$ and (b) $L = 2\,\mu\mathrm{m}$. Set $W = 400\,\mathrm{nm}$ and $a = 20\,\mathrm{nm}$ as usual. The wavelength range is $600\,\mathrm{nm} \sim 1100\,\mathrm{nm}$. Note that the bare waveguide supports higher order TM modes when the wavelength is less than 700 nm.

Let us consider the $L = 1\,\mu\mathrm{m}$ case first. As having been computed, when $W = 400\,\mathrm{nm}$, the beat length is about $2.1\,\mu\mathrm{m}$ at the wavelength of 800 nm. Further computations show that the beat length is stable over the wavelength range. Therefore, $1\,\mu\mathrm{m}$ is around half the beat length, when the PLC is expected to be most efficient. Let the transmission be T, and the reflection be R. Then $1-T-R$ indicates the power consumption on the metal structure due to the internal material loss and the radiative loss. As shown in Figure 34(a), the resonance corresponds to the drops in the transmission spectrum and peaks in the reflection spectrum. At the resonance, the field is more concentrated in the metal region, which lowers down the transmission and the overall $T + R$. At the same time, the higher field discrepancy at the metallic tip causes larger reflection. It is noticeable that the reflection part contributes less significantly to the overall $T + R$ than the transmission part, and therefore the profile of the $T + R$ spectrum is basically determined by the transmission spectrum. When

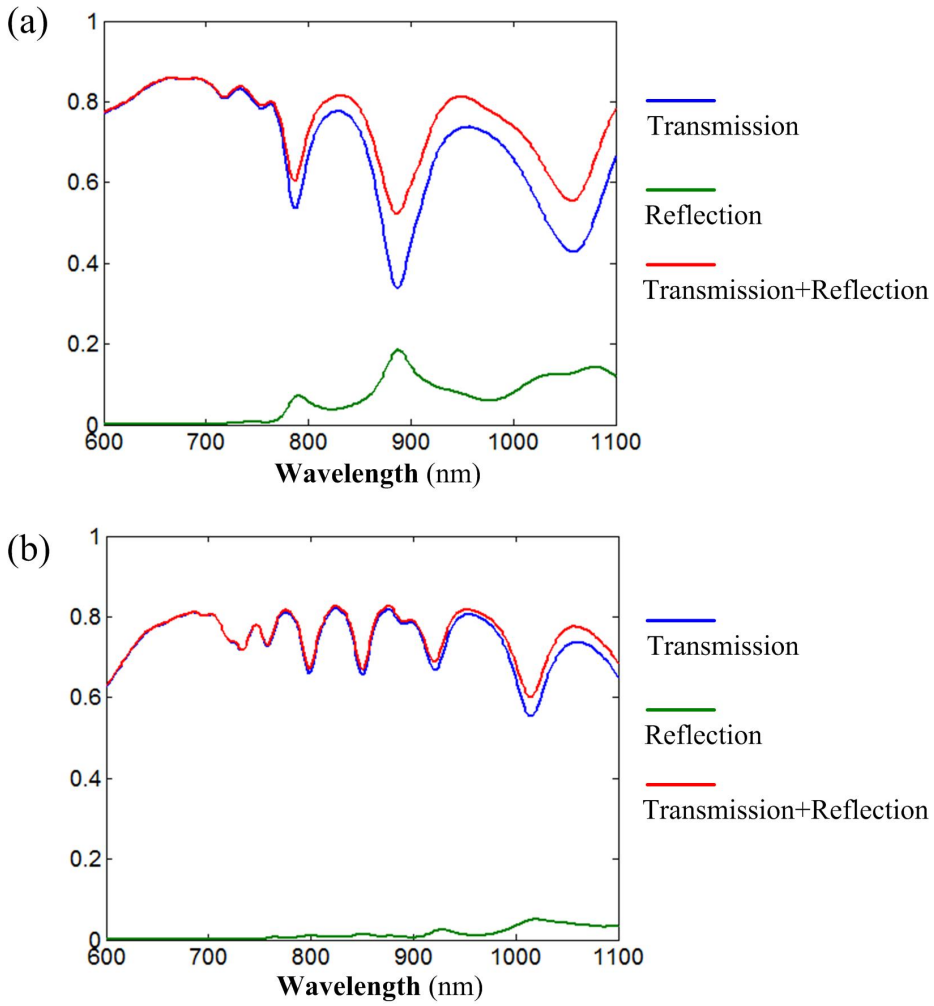

Figure 34: Spectra of transmission, reflection and transmission plus reflection for the Au triangle length (a) $L = 1\,\mu$m and (b) $L = 2\,\mu$m. The width W of the triangle is 400 nm. The radius of curvature a at the tip is 20 nm.

the structure is off resonance, $T + R$ is about 0.8, which means a certain amount of power is still coupled into the the metal region. This is quite different from a typical spectrum of a (plasmonic) resonator, which can reach a value very close to 1 when the structure is off resonance. Figure 34(b) shows the spectra in the $L = 2\,\mu$m case. The spacing between two successive drops in the transmission spectrum is clearly less than that of the $L = 1\,\mu$m case. Moreover, since $2\,\mu$m is close to the beat length, the PLC is expected to be less efficient. As a result, the overall reflection is a lot smaller than in the $L = 1\,\mu$m case.

In Figure 35, comparisons are made between the transmission spectrum and the FCF spectrum for three groups of metal triangle lengths. The first group (Figure 35(a)) has lengths $0.4\,\mu$m, $0.425\,\mu$m and $0.45\,\mu$m, the second group (Figure 35(b)) has lengths $1\,\mu$m, $1.025\,\mu$m and $1.05\,\mu$m, and the third group (Figure 35(c)) has lengths $2\,\mu$m, $2.025\,\mu$m and $2.05\,\mu$m. Set $W = 400\,$nm and $a = 20\,$nm as usual. Recall that by definition, FCF($a = 20\,$nm) is the normalized norm of the electric field at the point $(0, 320\,\text{nm}, 20\,\text{nm})$ in our coordinate system. When the wavelength is less than 700 nm, the bare photonic waveguide supports higher order TM modes and the hybrid structure supports more modes other than $\mathrm{H}_{\mathrm{TM},0}$ and $\mathrm{H}_{\mathrm{TM},1}$. Our analytic model using two supermodes is no longer valid in this case. As a result, the field concentration effect is tremendously suppressed. For wavelengths larger than 700 nm, the vertical dashed lines indicate that a local minima of the transmission corresponds almost exactly to a local maxima of the FCF, which means that the plasmonic structure is at resonance. Note that when L is small, the resonance wavelengths are more sensitive to a change ΔL of L.

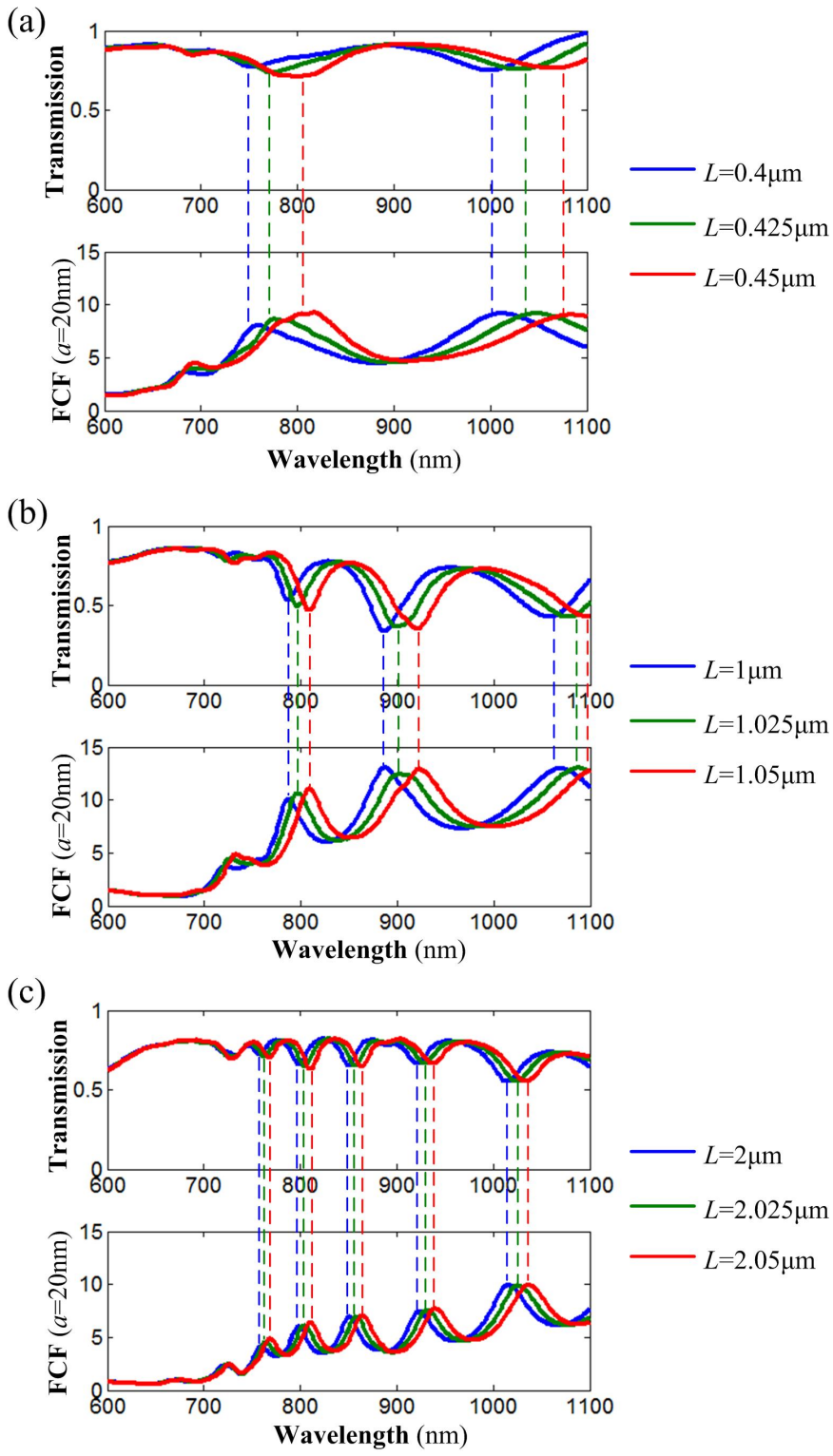

Figure 35: Spectra of transmission and field concentration factor for lengths of Au triangle (a) 0.4 μm, 0.425 μm and 0.45 μm, (b) 1 μm, 1.025 μm and 1.05 μm, and (c) 2 μm, 2.025 μm and 2.05 μm. The width W of the triangle is 400 nm. The radius of curvature a at the tip is 20 nm.

5.4 Silicon-based Plasmonic Light Concentrators

I will discuss two types of PLCs integrated on silicon in this section. One is based on tapering a strip hybrid photonic-plasmonic waveguide, which is analogous to the Si_3N_4-based PLCs discussed in Section 5.2 and 5.3, and the other one is based on tapering a slit hybrid waveguide, which can be considered as a dual structure to the former one. Accordingly, I call the first type tapered-strip PLCs, and the second type tapered-slit PLCs.

Figure 36 shows the mode analysis for a strip hybrid waveguide. The Si ridge has dimensions 500 nm $\times$250 nm, the SiO_2 buffer has dimensions 500 nm $\times$100 nm, and the Au strip has dimensions $w \times 50$ nm. The ambient material is air. Assume the working wavelength λ is 1550 nm. At this wavelength, the refractive index of Si is 3.48, the refractive index of SiO_2 is 1.45, and the permittivity of Au is about $-115 + j11$.

The corresponding purely photonic waveguide only support the fundamental TM mode (TM_0) and the fundamental TE mode (TE_0). Using the same analysis as in Section 5.2, the TM_0 mode can only couple with the symmetric modes of the corresponding purely plasmonic waveguide. As a result, under the aforementioned dimensions, a light incidence of the TM_0 mode can possibly excite two propagating supermodes, $H_{TM,0}$ and $H_{TM,1}$. The real parts of the effective indices of $H_{TM,0}$ and $H_{TM,1}$ are plotted in Figure 36(b). The $H_{TM,1}$ mode is a propagating mode when w is less than 90 nm, and becomes an evanescent mode (cut off) when w is larger than 90 nm. This is quite different from the case of the Si_3N_4-based hybrid waveguide I discussed in Section 5.2, where $H_{TM,1}$ is a propagating mode in the whole range of the width of the Au strip. Figure 36(c) shows the electric mode profiles of the $H_{TM,0}$ mode with $w = 500$ nm and $w = 50$ nm, and the $H_{TM,1}$ mode with $w = 0$ and $w = 50$ nm. Note that $H_{TM,1}(w = 0)$ is just the purely photonic mode TM_0. The $H_{TM,0}$ mode becomes more and more localized as w approaches 0.

Figure 37 shows the mode analysis for a slit hybrid waveguide. The dielectric

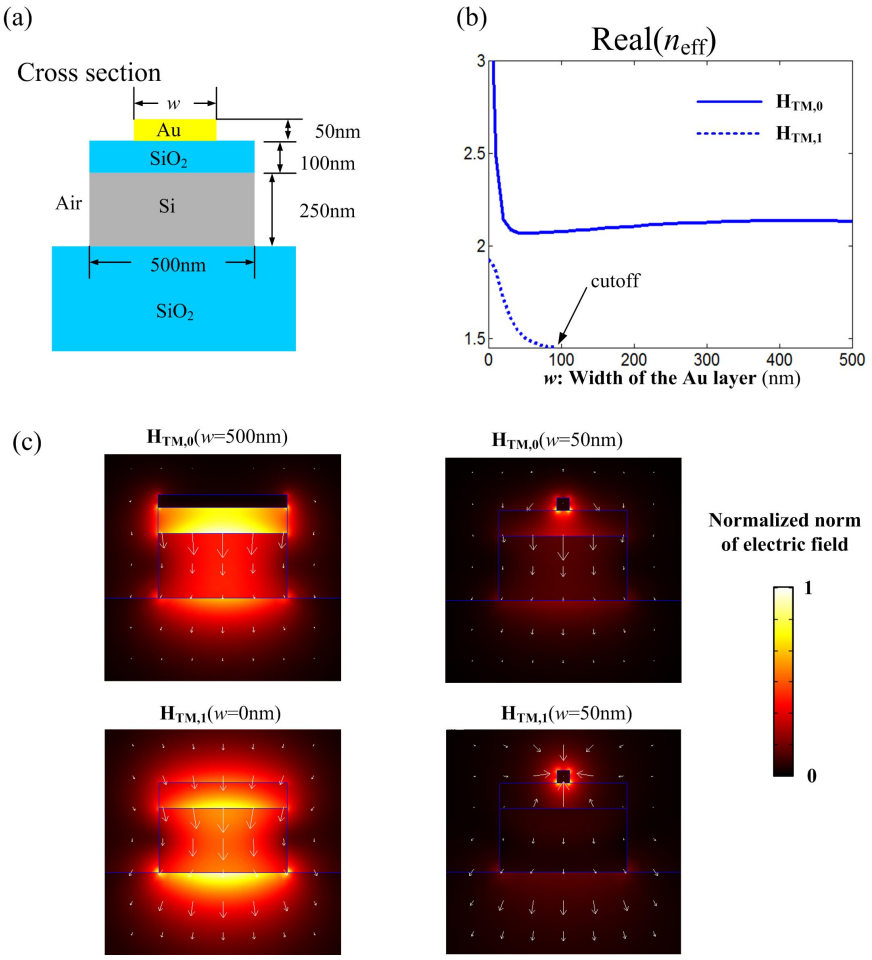

Figure 36: (a) The cross section of a strip hybrid waveguide. The size parameters are indicated. (b) Dispersion characterization of two supermodes, $H_{TM,0}$ and $H_{TM,1}$, with respect to the width w of the Au strip. The wavelength is 1550 nm. (c) The electric field profiles of the $H_{TM,0}$ mode with $w = 500$ nm and $w = 50$ nm, and the $H_{TM,1}$ mode with $w = 0$ and $w = 50$ nm.

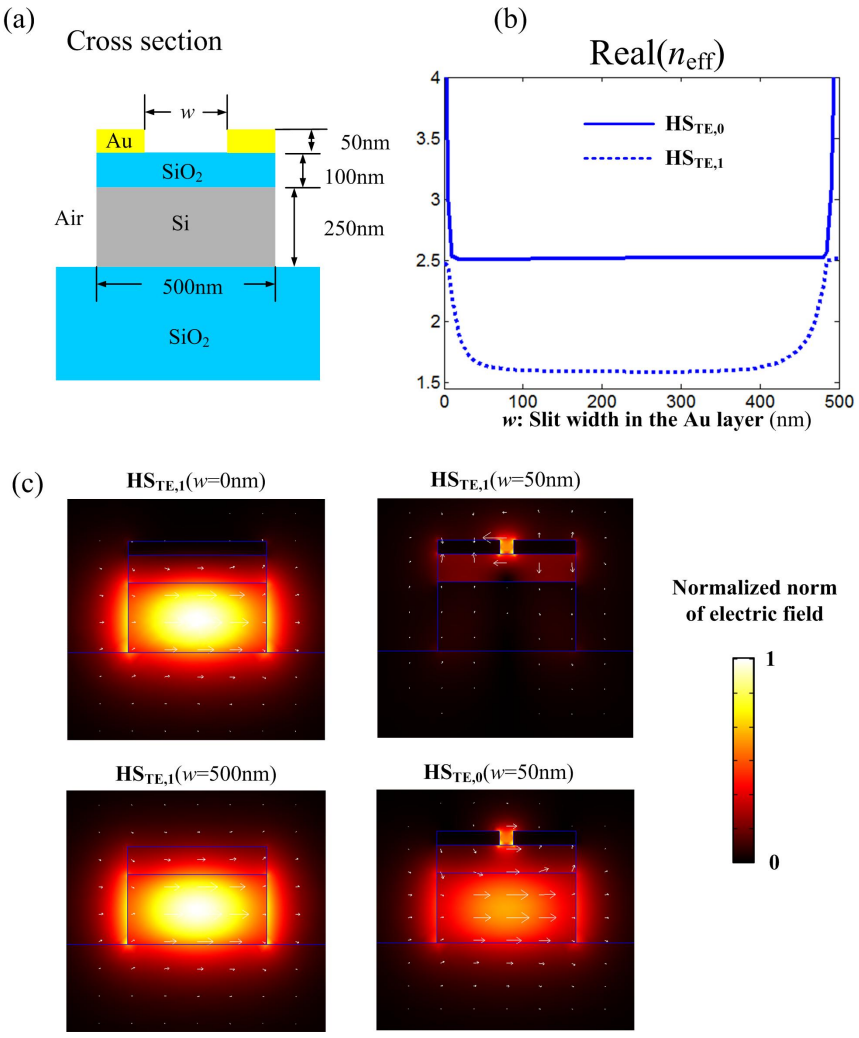

Figure 37: (a) The cross section of a slit hybrid waveguide with the size parameters indicated. (b) Dispersion characterization of two supermodes, $\mathrm{HS}_{\mathrm{TE},0}$ and $\mathrm{HS}_{\mathrm{TE},1}$, with respect to the slit width w. The wavelength is 1550 nm. (c) The electric field profiles of the $\mathrm{HS}_{\mathrm{TE},0}$ mode with $w = 0$ and $w = 50$ nm, and the $\mathrm{HS}_{\mathrm{TE},1}$ mode with $w = 500$ nm and $w = 50$ nm.

part has the same dimensions as in the strip hybrid waveguide, and the Au layer has thickness 50 nm. The full width of the Au layer is 500 nm, and the width of the opening is w. I still assume the ambient material to be air and the working wavelength to be 1550 nm.

I only consider the TE_0 mode of the corresponding purely photonic waveguide. Note that when $w = 0$, the slit hybrid waveguide has no opening and coincides with the strip hybrid waveguide with full width of the Au strip. Following the same analysis as in Section 5.2, I see that only the $H_{TE,0}$ mode is supported as a propagating mode in this case. This is quite different from the case of the Si_3N_4-based hybrid waveguide, where both $H_{TE,0}$ and $H_{TE,1}$ are propagating modes. Therefore, two supermodes ($HS_{TE,0}$ and $HS_{TE,1}$) that can be coupled with the incident TE_0 mode will be generated by opening a slit in the Au layer. Figure 37(b) shows the the real parts of the effective indices of $HS_{TE,0}$ and $HS_{TE,1}$, and Figure 37(c) shows the electric mode profiles of the $HS_{TE,0}$ mode with $w = 50$ nm, and the $HS_{TE,1}$ mode with $w = 0$, $w = 50$ nm and $w = 500$ nm. Note that $HS_{TE,1}(w = 0)$ is identical to the $H_{TE,0}$ mode for the strip hybrid waveguide with full width of the Au strip, and $HS_{TE,1}(w = 500\,\text{nm})$ is identical to the purely photonic mode TE_0. The $HS_{TE,0}$ mode becomes more and more localized, when w approaches either 0 or 500 nm.

Recall that the efficiency of an ultra-compact Si_3N_4-based PLC is mainly determined by three effects (mode beat, nanofocusing and weak resonance), as discussed in Section 5.3. This is also true for both types of Si-based PLCs discussed in this section. In particular, for a tapered-strip PLC, the incident purely photonic mode is TM_0, and the two beating supermodes are $H_{TM,0}$ and $H_{TM,1}$; for a tapered-slit PLC, the incident purely photonic mode is TE_0, and the two beating supermodes are $HS_{TE,0}$ and $HS_{TE,1}$.

Figure 38 shows the normalized electric field patterns in the plane $Y = 375$ nm for two PLCs of different types. The first one is a triangle-shaped tapered-strip PLC

with $L = 900\,\text{nm}$ and $W = 300\,\text{nm}$. The radius of curvature at the tip is 20 nm. The second one is a tapered-slit PLC with length 800 nm. The width of the larger opening at the input end is 300 nm, and the width of the small opening at the output end is 30 nm. Field concentration factors (FCF) can also be defined as the normalized norm of the electric field at point $(0, 375\,\text{nm}, 0)$. In both cases, I choose the length of the Au structure close to half of the beat length according to the principle of design in Section 5.3. As shown in Figure 38(a), the FCF is about 15.2, and in Figure 38(b), the FCF is about 12.5.

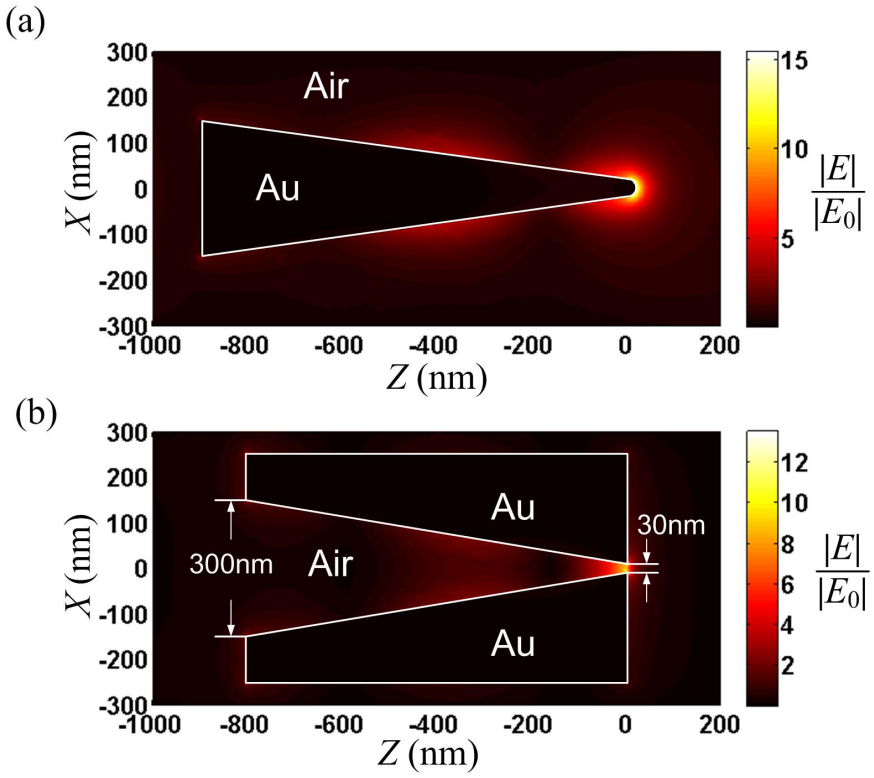

Figure 38: Normalized electric field patterns in the plane $Y = 375\,\text{nm}$ which horizontally cuts through the Au layer for (a) a tapered-strip PLC and (b) a tapered-slit PLC. The wavelength is 1550 nm.

CHAPTER VI

EXPERIMENTAL DEMONSTRATIONS OF ON-CHIP PLASMONIC LIGHT CONCENTRATION

The work present in this chapter is in collaboration with my colleague Maysamreza Chamanzar and with Aniello Apuzzo and Sylvain Blaize from Laboratoire de Nanotechnologie et d'Instrumentation Optique (LNIO) at Université de Technologie de Troyes (UTT). Experimental characterizations are performed on two Si-based samples we fabricated, including scattering and near-field detections.

6.1 Design and Fabrication

The samples I designed for test has the dimensions as shown in Figure 39 including both types of PLCs (tapered strips and tapered slits). As shown in Figure 39 (a1) and (b1), the width of the bare waveguides is designed to be 500 nm and the height is 220 nm, and the SiO_2 buffer layer has thickness of 20 nm and also has width of 500 nm. The Au layer of the plasmonic pattern has thickness 30 nm. In design, the width W of the tapered triangle is 300 nm while patterns of different lengths L are fabricated (Figure 39 (a2)). Also, the tip of a tapered triangle is rounded up with a radius of 20 nm. For the tapered slits, an initial outer width W_{out} is 400 nm, an initial inner width W_{in} of 300 nm, and the gap width at the tip is 50 nm. Also, there are several different values of length L for different patterns. The reason that W_{out} has value 400 nm which is smaller than the width of the Si waveguide underneath is for the consideration of the two-step fabrication described below. Such a difference won't affect the functionality of the waveguide.

The fabrication is carried out in the the Nanotechnology Research Center (NRC)

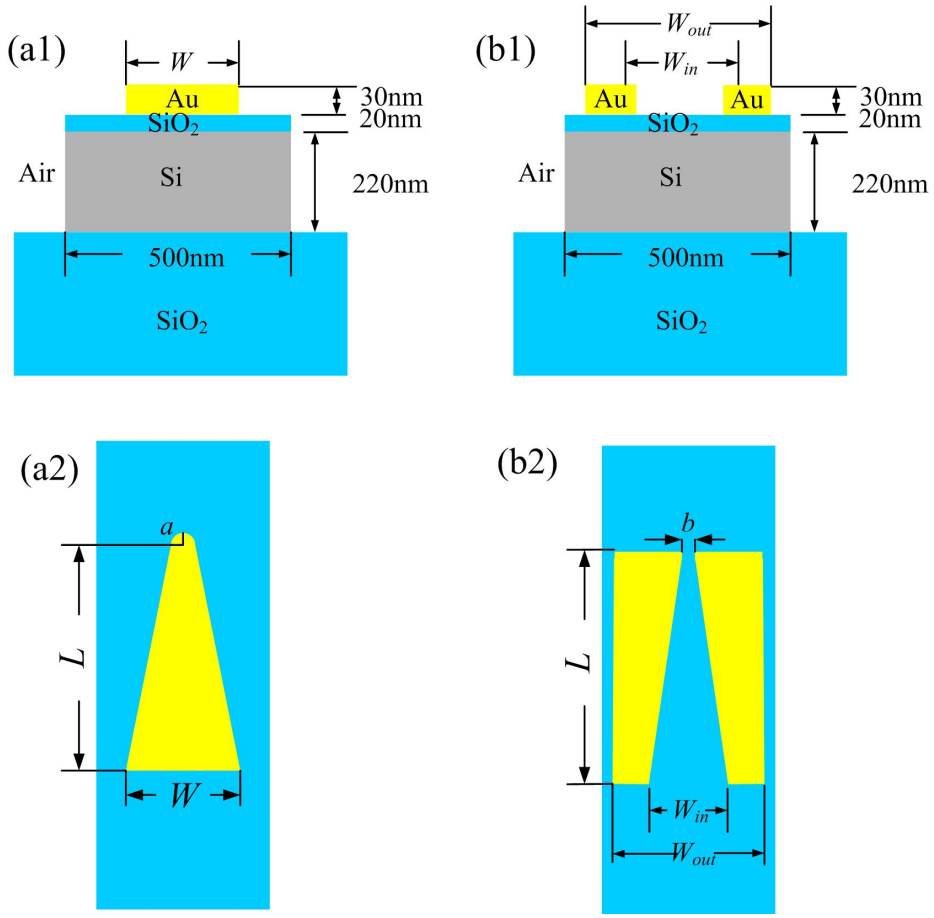

Figure 39: (a1) (a2): The dimensions of the Si waveguides and plasmonic tapered triangles. In design, the triangles has width W of is 300 nm, several different values of length L, and radius a of curvature at the tip is 20 nm. (b1) (b2): The dimensions of the Si waveguides and plasmonic tapered slits. In design, the tapered slits has an initial outer width W_{out} of 400 nm, an initial inner width W_{in} of 300 nm, several different values of length L, and the gap distance at the tip b is 50 nm.

at Georgia Institute of Technology by my colleague Maysamreza Chamanzar. Because the hybrid device has two parts: the photonic structures (waveguides) and the plasmonic structures, the fabrication procedure also consists of two major steps of electron beam lithography (EBL), one for defining the photonic structure patterns and the other for defining the plasmonic patterns respectively. The fabrication process is on a 2 μm buried oxide (BOX) layer.

The first step of electron beam lithography is carried out to define the triangle plasmonic layer in polymethyl methacrylate (PMMA) electron beam resist. Then 2 nm titanium and 30 nm gold are evaporated on the sample and lift off is carried out in 1165 microposit remover bath. In the next step, the waveguides were defined using e-beam lithography and ICP etching.

Two duplicated samples were fabricated based on the same design. However, alignment between the two steps is critical and different qualities among fabrications of different samples can happen. Actually, the alignment of one of the samples is not as good as the other. Figure 40 shows the scanning electron micrograph (SEM) of the sample with a good alignment where the plasmonic patterns are well centered on the Si waveguides (called 'Sample I'), and Figure 41 shows the SEM of the sample with a shifted alignment where the plasmonic patterns are shifted from the center of the Si waveguides (called 'Sample II'). Experimental characterizations are performed on both samples.

As shown in Figure 40, we can see that the fabrication imperfections of the plasmonic patterns happen mostly on two sides: one is the roughness of the outer boundaries of the patterns and the other is non-flatness of the top surface of the plasmonic patterns. Both irregularities will affect the efficiency of light concentration. The dimensions of the fabricated structures are close to the design, although do not match perfectly. The overall quality is satisfactory.

For Sample II, since the patterns are all shifted (Figure 41) about 60 $\sim$ 80 nm

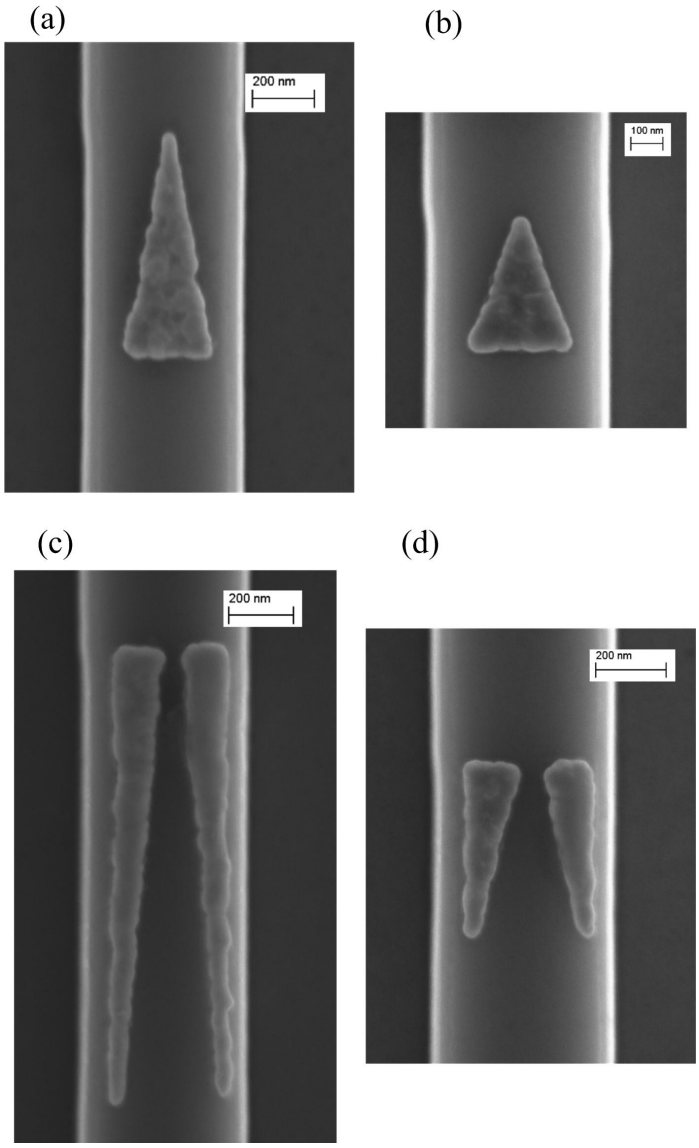

Figure 40: Some plasmonic patterns on Sample I. (a) and (b): tapered triangles; (c) and (d): tapered slits

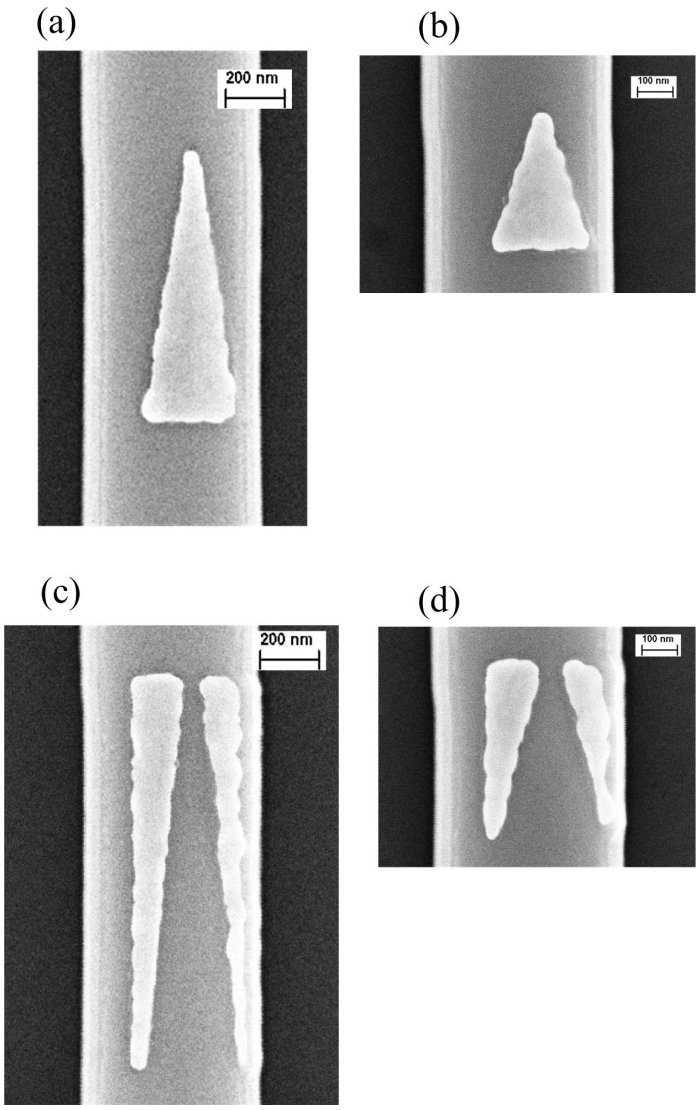

Figure 41: Some plasmonic patterns on Sample II. (a) and (b): tapered triangles; (c) and (d): tapered slits

from the central line of the Si waveguide underneath, we can also expect the near-field patterns and concentration efficiencies of the plasmonic patterns will be affected. Theoretical analysis is performed to study the influence of misalignments. As shown in Figure 41 (a) and (b), the tapered triangles still well sit on the waveguides underneath, and the simulations will show that the concentration efficiencies won't be affected much. However, as shown in Figure 41 (c) and (d), one side of the tapered slits actually collapse which will make those patterns unusable.

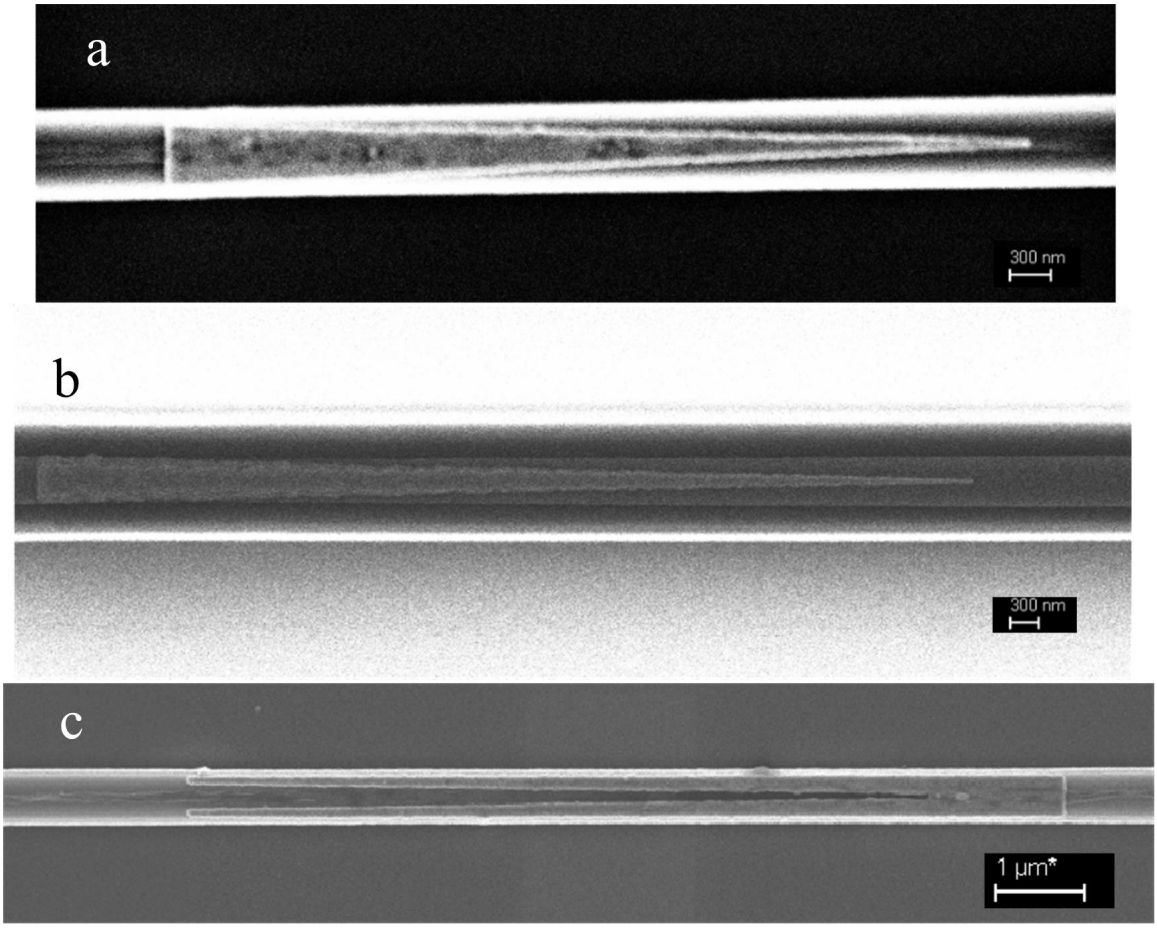

Figure 42: Some fabricated patterns on other samples (not sample I or II). (a) and (b) long tapered Au triangles and (c): a long tapered slit.

Figure 42 shows some patterns we have fabricated other than samples I and II. Generally speaking, these are long tapered strips and slits. These structures have good fabrication qualities with acceptable roughness on the pattern boundaries.

6.2 Mode Analysis

In this section, I will focus on analyzing the modes of the hybrid photonic-plasmonic waveguides corresponding to the tapered strips, since near-field measurements are performed on these patterns.

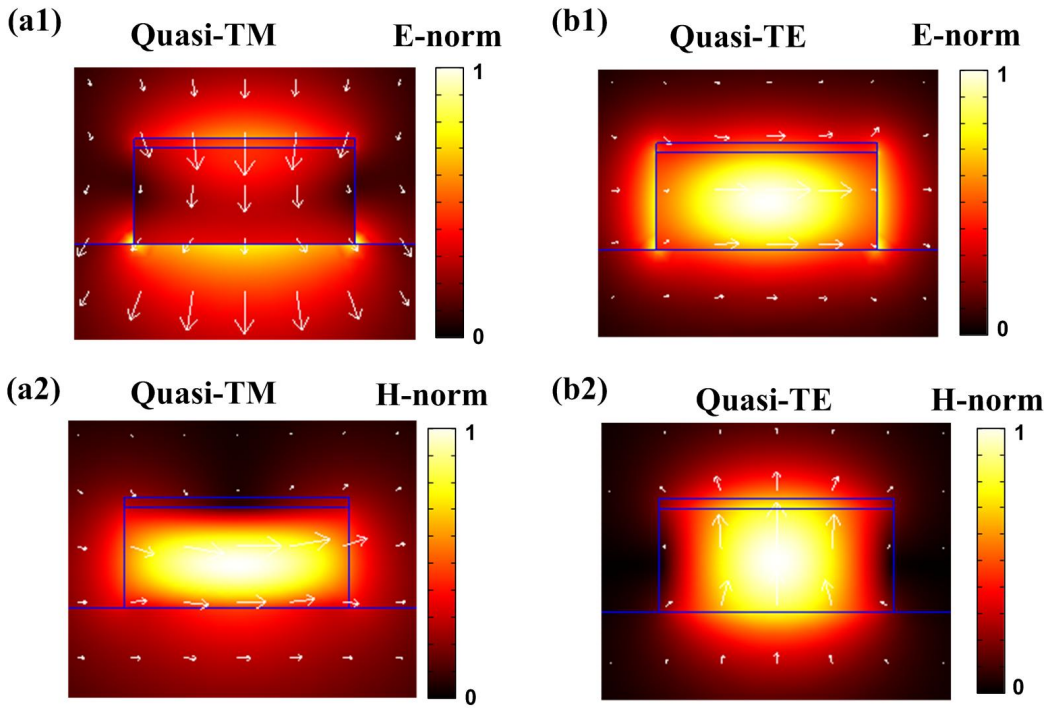

Figure 43: (a) and (b): The normalized electric and magnetic fields of the fundamental quasi-TM mode of the bare waveguide. (c) and (d): The normalized electric and magnetic fields of the fundamental quasi-TE mode of the bare waveguide. The wavelength is 1550 nm. The arrows demonstrate the electric field lines for (a) and (c), and magnetic field lines for (b) and (d).

Figure 43 shows the normalized amplitudes of the electric and magnetic field of the bare waveguide where only the fundamental quasi-TM and quasi-TE mode exist as propagating modes. The dimensions of the bare waveguide are as designed, i.e., silicon (500 nm $\times$220 nm) and silicon dioxide (500 nm $\times$20 nm).

The mode effective index for the quasi-TM mode is 1.61, and the mode effective index for the quasi-TE mode is 2.40. The values of the mode effective indices will be different if the dimensions of the waveguide are not authentic to the design. Here are

some examples. If the width is changed to 480 nm, then the mode effective indices for quasi-TM and quasi-TE modes will be 1.59 and 2.36, respectively. If the width is changed to 460 nm, then the mode effective indices for quasi-TM and quasi-TE modes will be 1.57 and 2.31, respectively. If the width is changed to 520 nm and thickness of Si is changed to 250 nm, then the effective indices are 1.88 and 2.54. Roughly speaking, the effective index of either quasi-TM or quasi-TE mode will increase if the dimensions of the cross section of the bare waveguide increase.

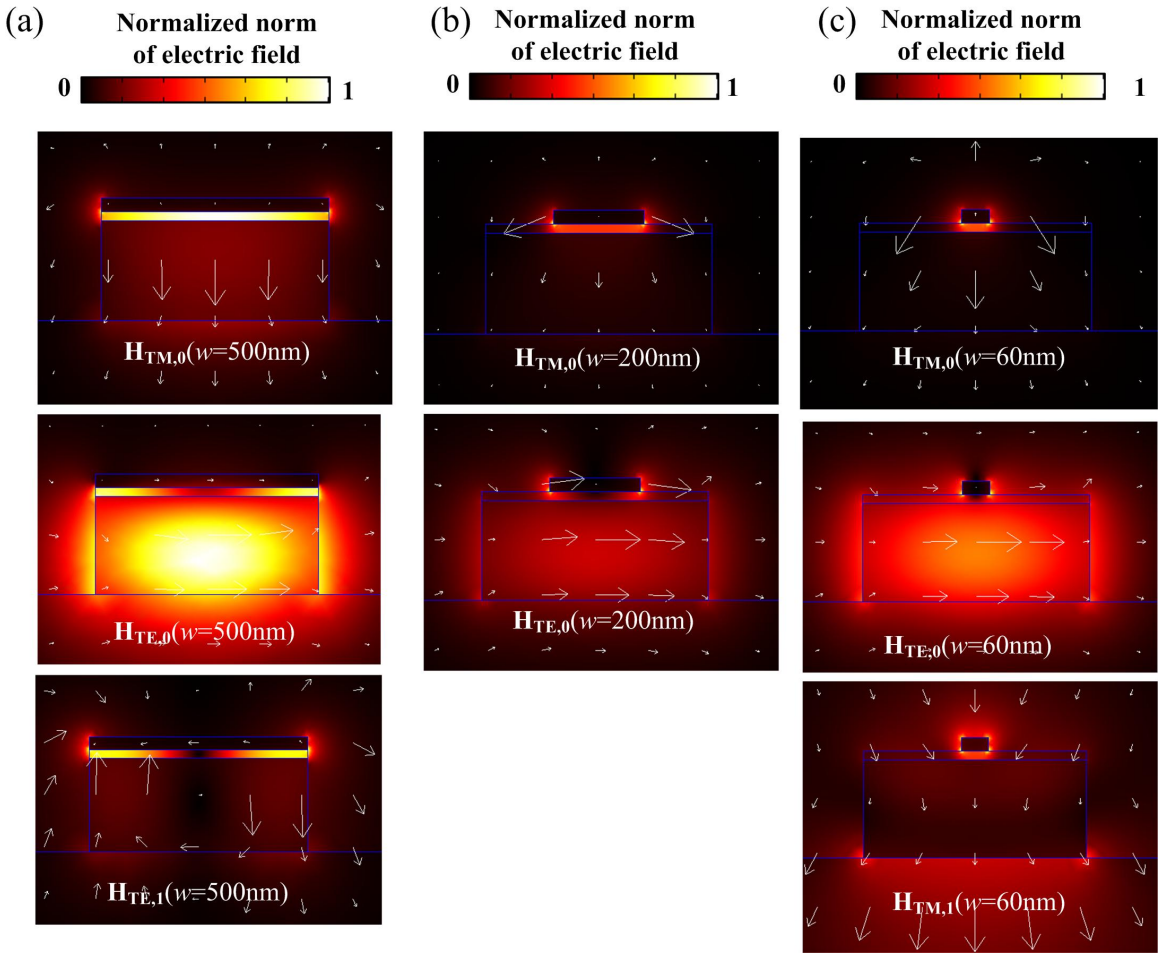

Figure 44: (a) The mode profiles for the propagating supermodes $H_{TM,0}$, $H_{TE,0}$ and $H_{TE,1}$ when the width w of the Au layer is 500 nm. b) The mode profiles for the propagating supermodes $H_{TM,0}$, $H_{TE,0}$ when $w = 200$ nm. c) The mode profiles for the propagating supermodes $H_{TM,0}$, $H_{TE,0}$ and $H_{TM,1}$ when $w = 60$ nm.

Figure 44 shows the E-field profiles of the propagating photonic-plasmonic supermodes $H_{TM,0}$, $H_{TE,0}$ and $H_{TE,1}$ when the width w of the Au layer is 500 nm, 200 nm or 60 nm. The modes $H_{TM,0}$ and $H_{TE,0}$ are propagating modes for all the widths. As shown in Figure 44(a), when $w = 500$ nm, $H_{TE,1}$ is a propagating mode while $H_{TM,1}$ is not; in Figure 44(b), when $w = 200$ nm, neither $H_{TM,1}$ nor $H_{TE,1}$ is a propagating mode; in Figure 44(c), when $w = 60$ nm, $H_{TM,1}$ is a propagating mode while $H_{TE,1}$ is not.

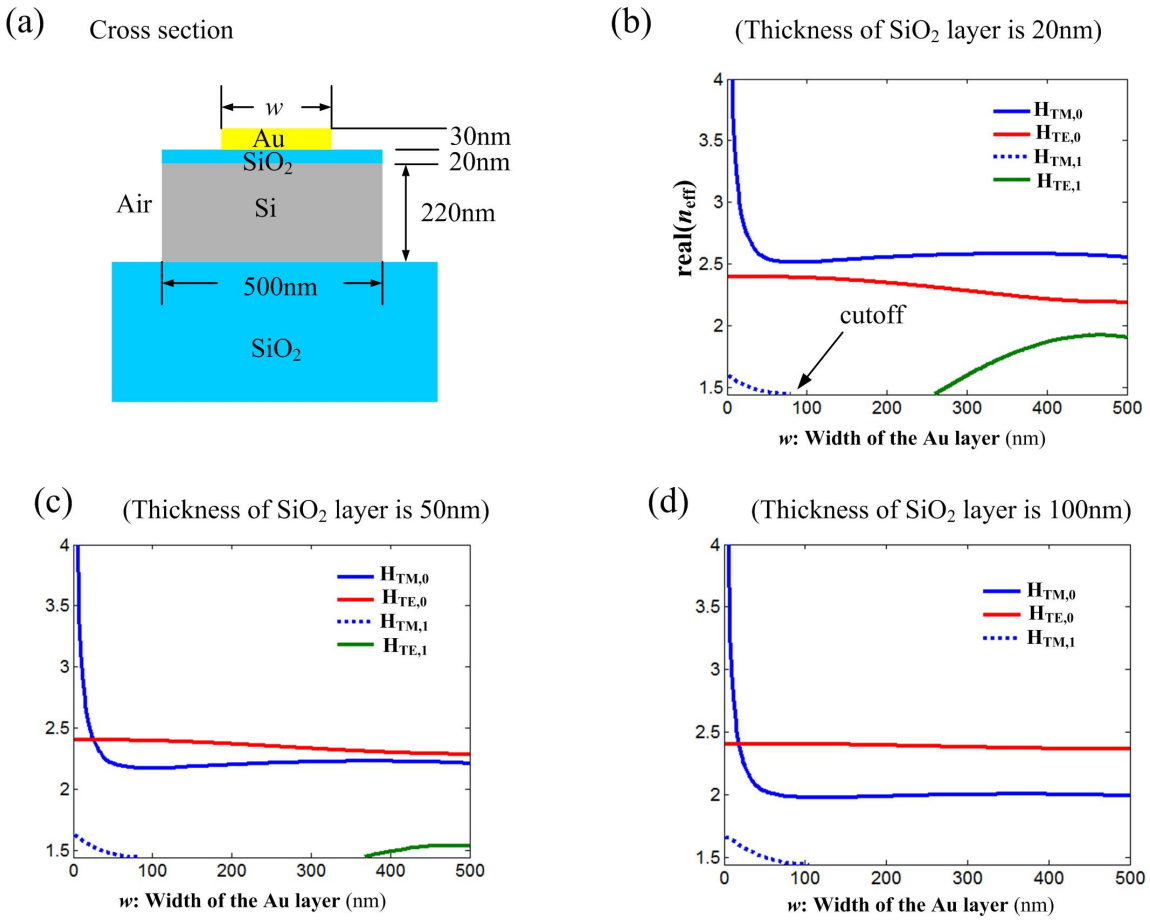

Figure 45: a) The cross section of the corresponding strip hybrid waveguide with varied width w of the Au layer. b) The dispersion characterization of supermodes $H_{TM,0}$, $H_{TM,1}$, $H_{TE,0}$ and $H_{TE,1}$ with respect to w. c) Dispersion characterization when the thickness of the oxide layer is adjusted to 50 nm. d) Dispersion characterization when the thickness of the oxide layer is adjusted to 100 nm.

The dispersion diagrams of the four supermodes with respect to the width w of

the Au layer are plotted in Figure 45(b) where the oxide buffer layer has a thickness of 20 nm (the same as the fabricated samples). For w in a region from 80 nm and 260 nm, the $H_{TM,1}$ and $H_{TE,1}$ modes are not supported as guided modes. As the width w further decreases, the $H_{TM,1}$ mode, which is a higher order quasi-TM mode, appears. As the width w tends to zero, the effective index of the $H_{TM,0}$ increases to infinity, which means it is more confined around the plasmonic region, whereas the $H_{TM,1}$ mode stays around the dielectric waveguide. When $w = 0$, $H_{TM,1}$ becomes the fundamental quasi-TM mode in the bare waveguide.

Figure 45(b) and (c) show the dispersion diagrams of the supermodes when the thickness of the oxide layer is increased to 50 nm and 100 nm respectively. One can observe that the effective indices of the $H_{TM,1}$ mode and $H_{TE,0}$ mode does not change much for different thicknesses of the oxide layer, while the $H_{TM,0}$ mode and $H_{TE,1}$ mode have effective indices that are quite sensitive to the oxide layer thickness. The reason that the $H_{TM,1}$ mode and $H_{TE,0}$ mode are relatively not quite affected by the thickness change is that they are closer to the purely photonic modes (the fundamental quasi-TM and quasi-TE modes) of the corresponding bare waveguide.

For the incident fundamental quasi-TM of the Si waveguide at 1550 nm, only the $H_{TM,0}$ and $H_{TM,1}$ supermodes can be excited at the input of the plasmonic nanotaper (i.e., at $W = 300$ nm). As soon as these supermodes are excited, they propagate through the plasmonic nanotaper and they couple through a directional coupling mechanism. Recall that the beat length BL is defined as the length over which the relative phase of the supermodes differ by 2π, which is inversely proportional to the real part of the difference between their effective indices and can be obtained as $BL(w) = \lambda/\text{real}(\triangle n_{\text{eff}}(w))$, where λ is the operation wavelength. BL decreases as the light propagates along the triangle since the effective index of $H_{TM,0}$ increases as the width of the triangle nanotaper decreases. Finally, the effective index of $H_{TM,0}$ increases asymptotically to infinity and thus the BL approaches zero at the apex of

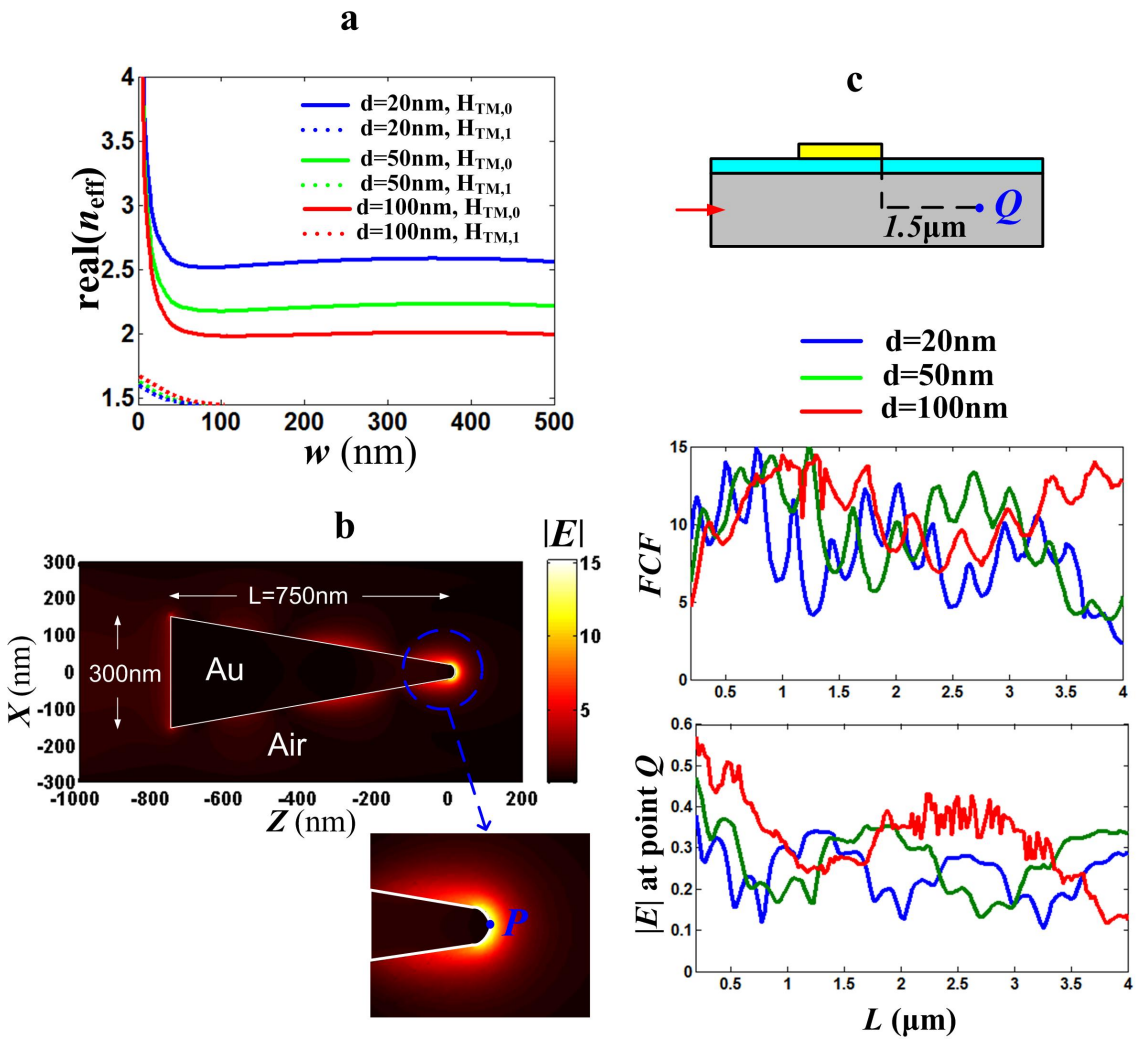

Figure 46: (a) Dispersion diagrams of the supermodes $H_{TM,0}$ and $H_{TM,1}$ for the hybrid waveguides with different thickness d of the silicon dioxide layer ($d = 20$ nm for blue curves, $d = 50$ nm for green curves and $d = 100$ nm for red curves). (b) Electric field profile in the middle plane of the gold layer with a zoom at its apex. The field is normalized to the average electric field amplitude in the corresponding bare waveguide. The field concentration factor (FCF) is the normalized field amplitude at the apex point 'P'. The thickness of the silicon dioxide layer is 20 nm. The tapered triangle has width 300 nm and length 750 nm. c) The field concentration factor (FCF) and the E-field amplitude at point 'Q' verses the length L of the nanotaper. The width of the taper is fixed at 300 nm. The thicknesses of silicon dioxide layer are 20 nm, 50 nm and 100 nm for curves of color 'blue', 'green' and 'red', respectively.

the triangle nanotaper, where the group velocity asymptotically approaches to zero. As a result, the electromagnetic energy is focused at the apex of the nanotaper in a very small volume.

Based on the dispersion diagrams in Figure 46(a) for the $H_{TM,0}$ and $H_{TM,1}$ modes, the average beat length of the nanotaper with 20 nm-thick, 50 nm-thick and 100 nm-thick oxide layer is estimated to be around $BL(w = 150\,\text{nm}) = 1.4\,\mu\text{m}, 1.8\,\mu\text{m}$ and $2.4\,\mu\text{m}$. Using the design principle introduced Section 5.3 which says the PLC is most efficient when its length is around half of the beat length, we can expect that the $FCF - L$ curve for each has a maximum around $L = 0.7\,\mu\text{m}, 0.9\,\mu\text{m}$ and $1.2\,\mu\text{m}$ for oxide layer thickness $20\,\text{nm}, 50\,\text{nm}$ and $100\,\text{nm}$ respectively, which is verified in Figure 46(c) (the slow variation in each of the curves). In addition, in Figure 46(c), the electrical field amplitude at point 'Q' is computed as a monitor of light transmission in the photonic waveguide, and one can observe that the FCF is maximum when the strength of the electric field is minimum at point 'Q'. This correlation implies higher consumption of the input optical power and hence lower optical transmission. Moreover, the ripples on the curves of FCF come from weak resonances between the forward wave propagating and the reflected wave at the apex of the nanotaper.

6.3 Field Simulations of Mixed TM-TE inputs

In this section, simulations of different ratios of mixed TM-TE inputs are shown and discussed. Two types of plasmonic nanotapers are discussed, i.e., $L = 750\,\text{nm}$ triangle and $L = 900\,\text{nm}$ shifted triangle, corresponding to the fabricated patterns in Figure 40(a) and 41(a), respectively.

For $L = 750\,\text{nm}$, Figure 47 and 48 show the profiles in the middle plane of the Au layer of the the electric field amplitude $|E|$, the amplitude (E_x, E_y and E_z) and phase (φ_x, φ_y and φ_z) of all three components of the electric field for purely TM input and TE input, respectively.

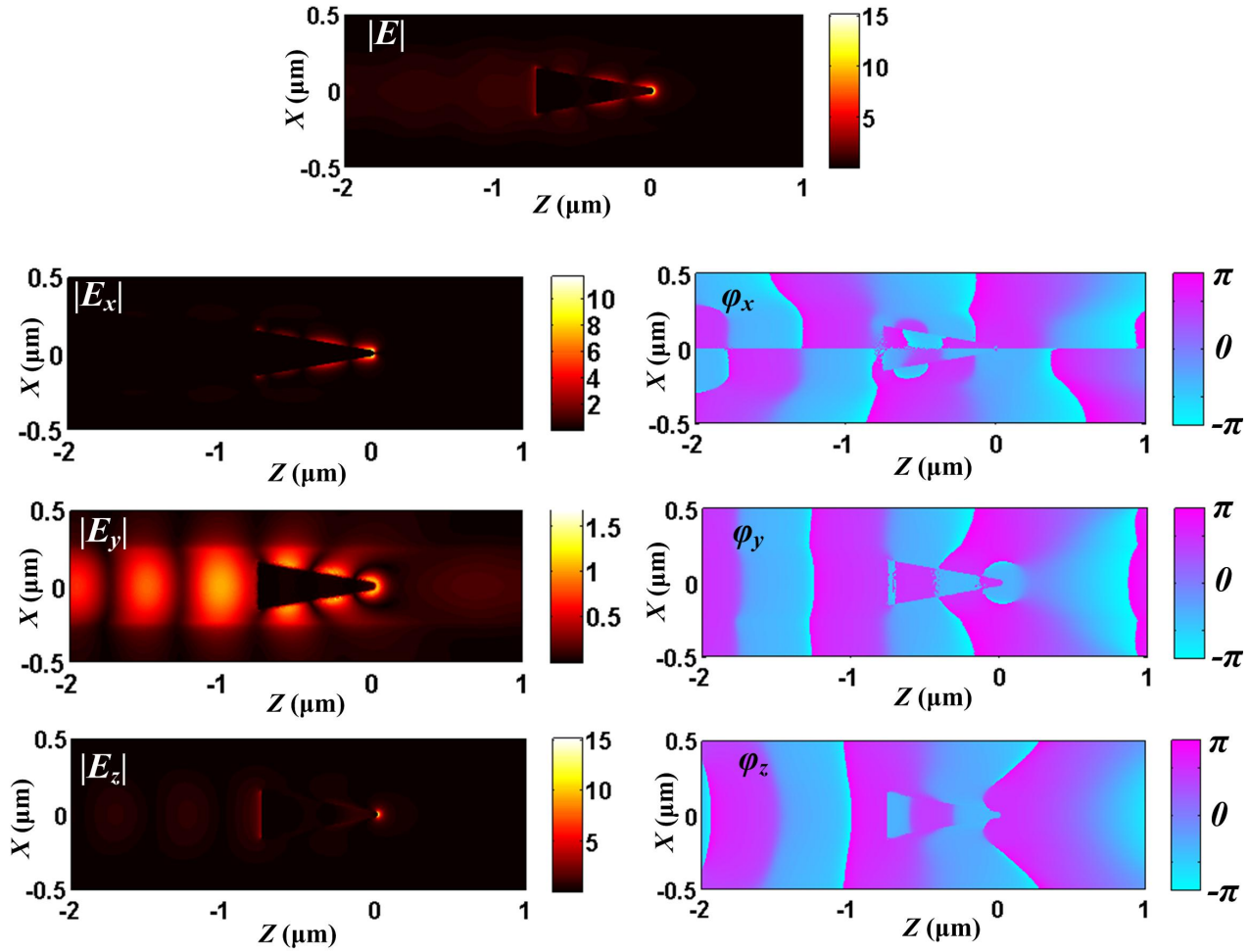

Figure 47: The upper panel is the electric field amplitude profile in the middle plane of the Au layer with a TM input. The amplitude (E_x, E_y and E_z) and phase (φ_x, φ_y and φ_z) of all three components of the electric field are shown in the following panels. The length L of the nanotaper is 750 nm.

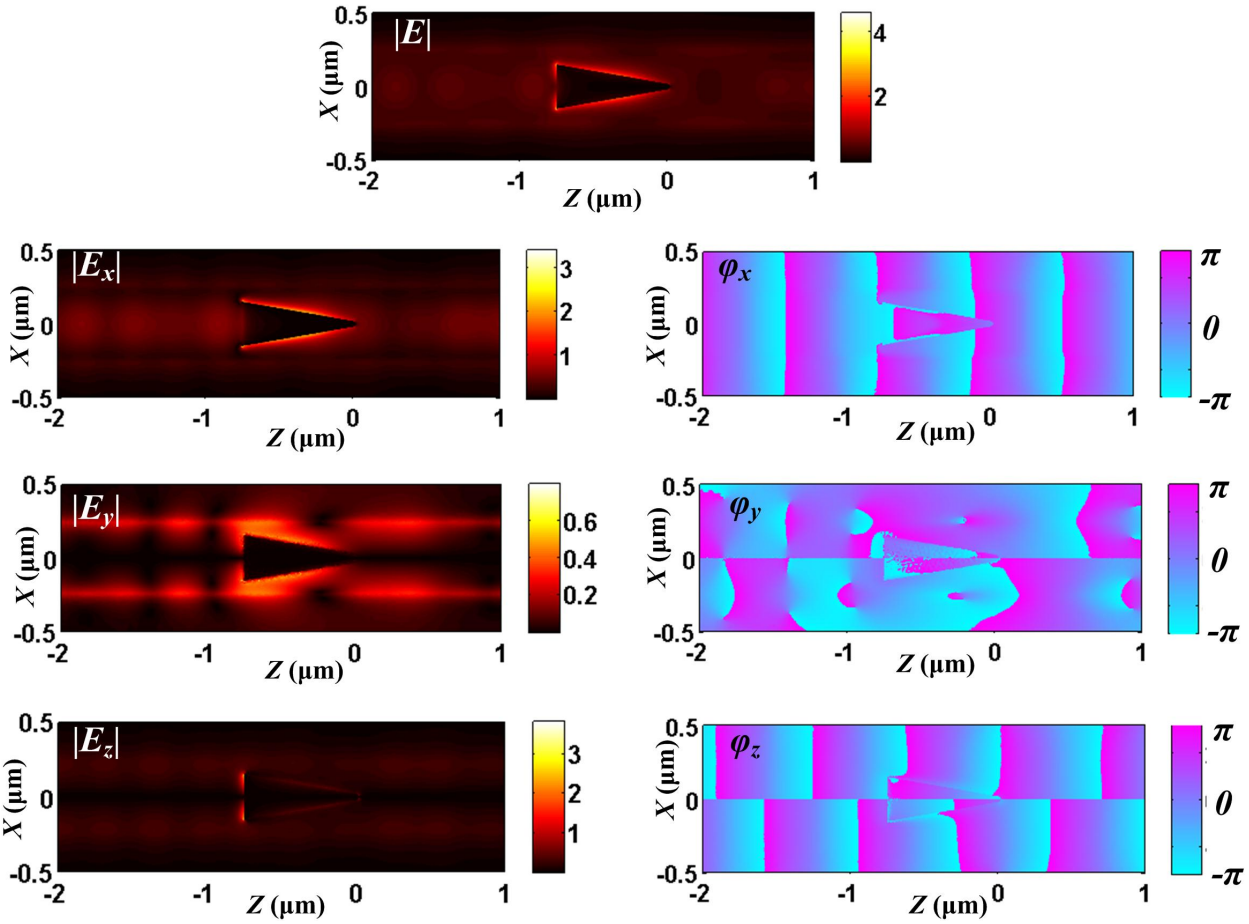

Figure 48: The upper panel is the electric field amplitude profile in the middle plane of the Au layer with a TE input. The amplitude (E_x, E_y and E_z) and phase (φ_x, φ_y and φ_z) of all three components of the electric field are shown in the following panels. The length L of the nanotaper is 750 nm.

As expected, only the TM input induces nanofocusing and the strongest focused field component is E_z. It is interesting to notice that the plasmonic nanotaper distorts the phase of the guided waves.

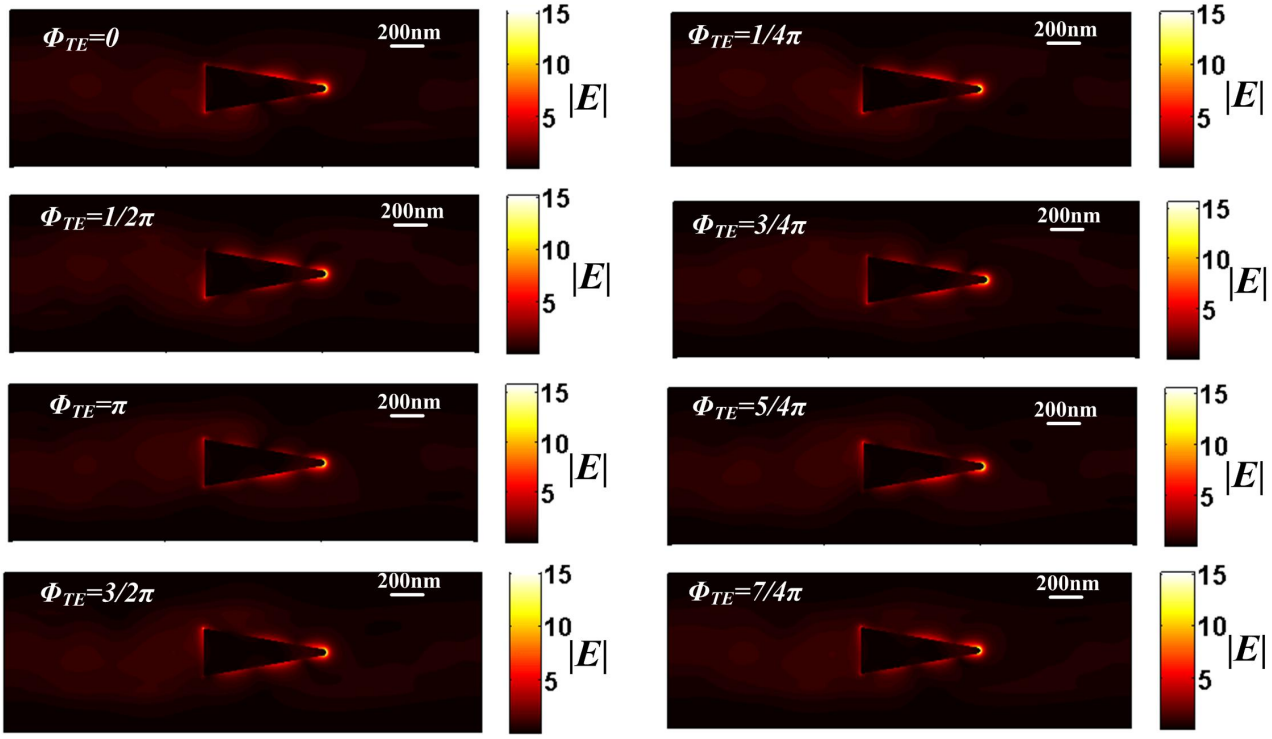

Figure 49: Interference patterns of E-field amplitude for a mixed TM and TE input with fixed phase φ_{TM} of TM input being 0 and varied phase φ_{TE} of TE input. The amplitude ratio of TM and TE inputs is $1:1$.

Now, let us consider a mixed input of TM-TE amplitude ratio $1:1$ and different relative phases. As shown in Figure 49, for phase differences spread over $[0, 2\pi]$ $(0, \pi/4, \pi/2, 3\pi/4, \pi, 5\pi/4, 3\pi/2, 7\pi/4)$ at a certain reference point, one can see that the field distributions along the two sides of the tapered triangle become a little asymmetric. However, the maximum amplitude of normalized E-field around the apex is still around 15, which does not change much from a pure TM input.

Since the energy coupling of the TM input into the metallic layer is a lot stronger than the TE input, the interference patterns around the plasmonic nanotaper are shown in Figure 50 when the TM-TE amplitude ratio changes $1:3$ which makes

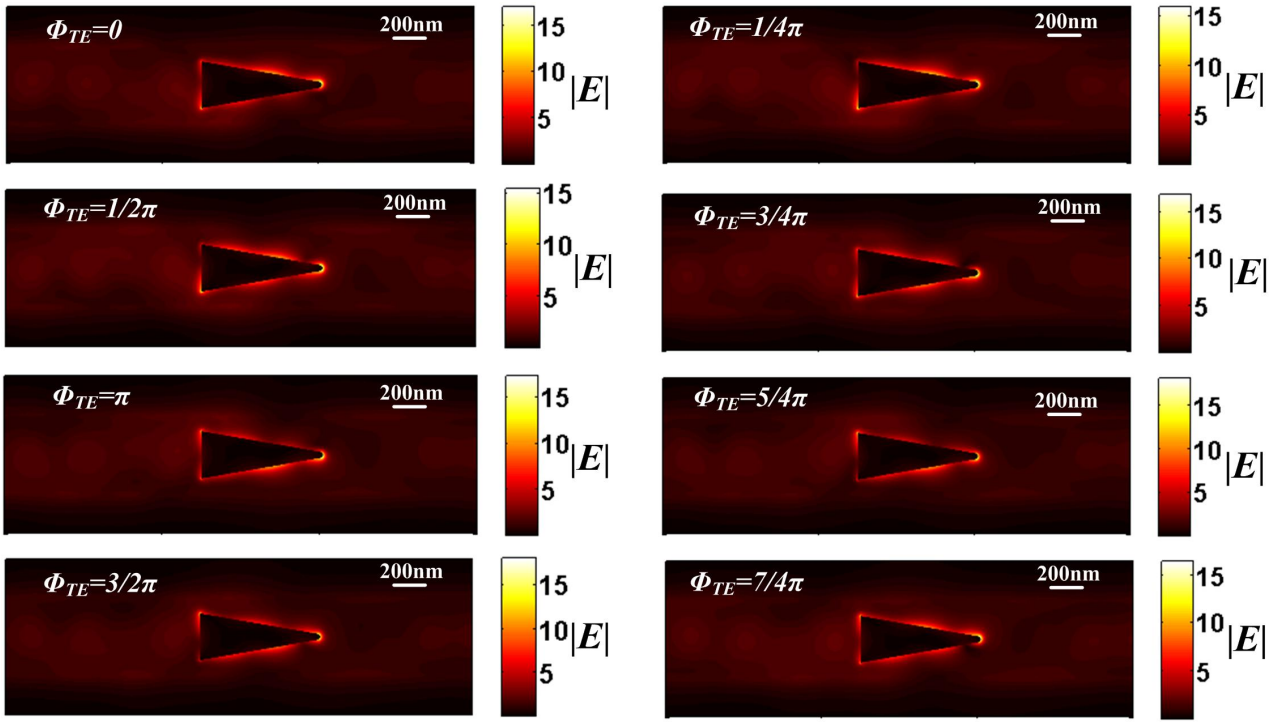

Figure 50: Interference patterns of E-field amplitude for a mixed TM and TE input with fixed phase φ_{TM} of TM input being 0 and varied phase φ_{TE} of TE input. The amplitude ratio of TM and TE inputs is $1:3$.

their plasmon excitations more balanced. As a result, the asymmetry along the two sides of the tapered triangle becomes more prominent for each different relative phase of the quasi-TM and quasi-TE inputs. In addition, the maximum amplitude of E-field around the apex becomes more unstable (e.g., when $\varphi_{TE} = 3/2\pi$, the maximum value can be around 17.).

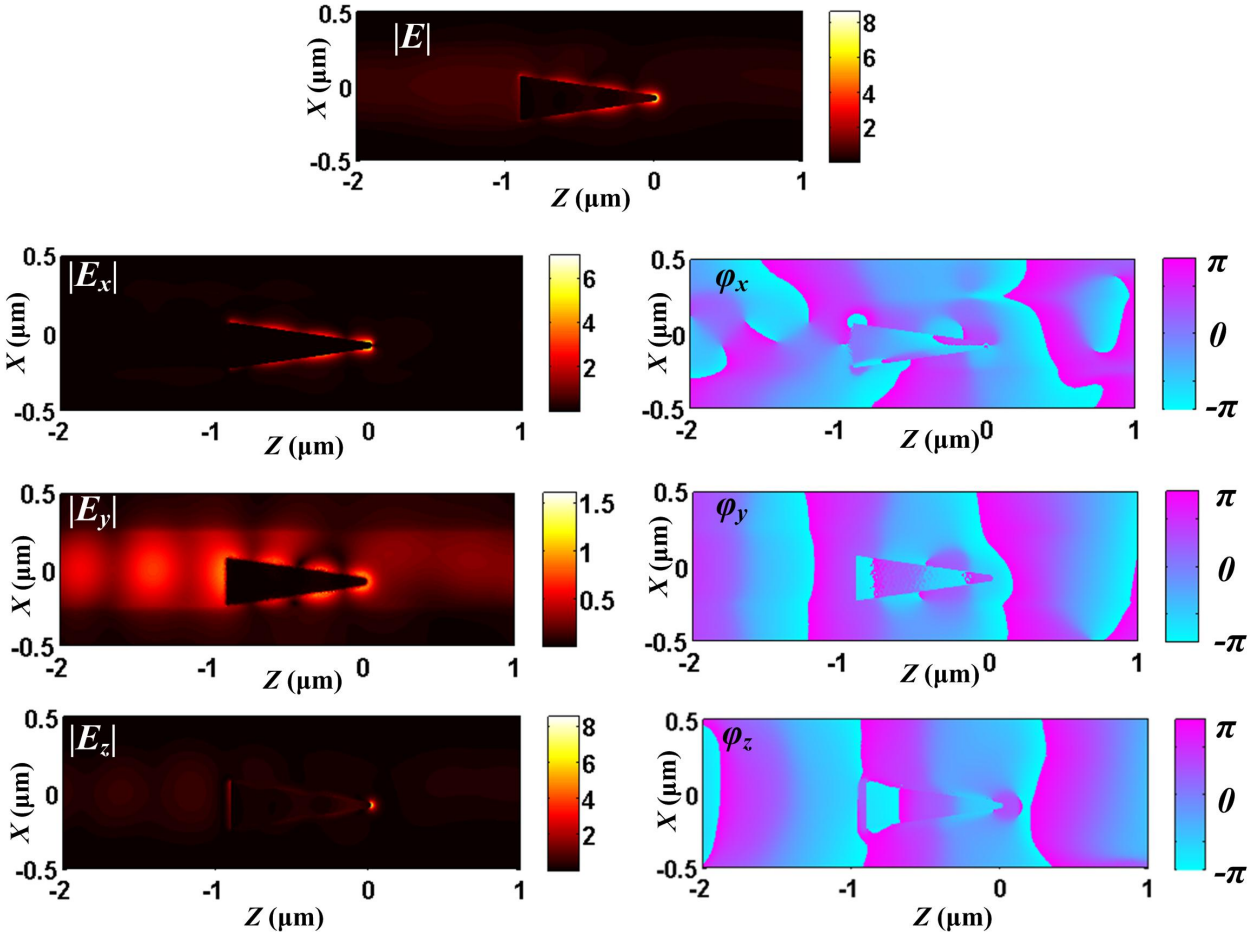

Figure 51: The upper panel is the electric field amplitude profile in the middle plane of the Au layer with a TM input. The amplitude (E_x, E_y and E_z) and phase (φ_x, φ_y and φ_z) of all three components of the electric field are shown in the following panels. The plasmonic nanotaper is shifted in the X direction of $80nm$ and has length $L = 900\,\text{nm}$.

For the shifted nanotaper of $L = 900\,\text{nm}$, Figure 51 and 52 show the profiles of $|E|$, E_x, E_y and E_z, φ_x, φ_y and φ_z of the electric field for purely TM input and TE input, respectively. Since the fabricated structure is shifted from the central line

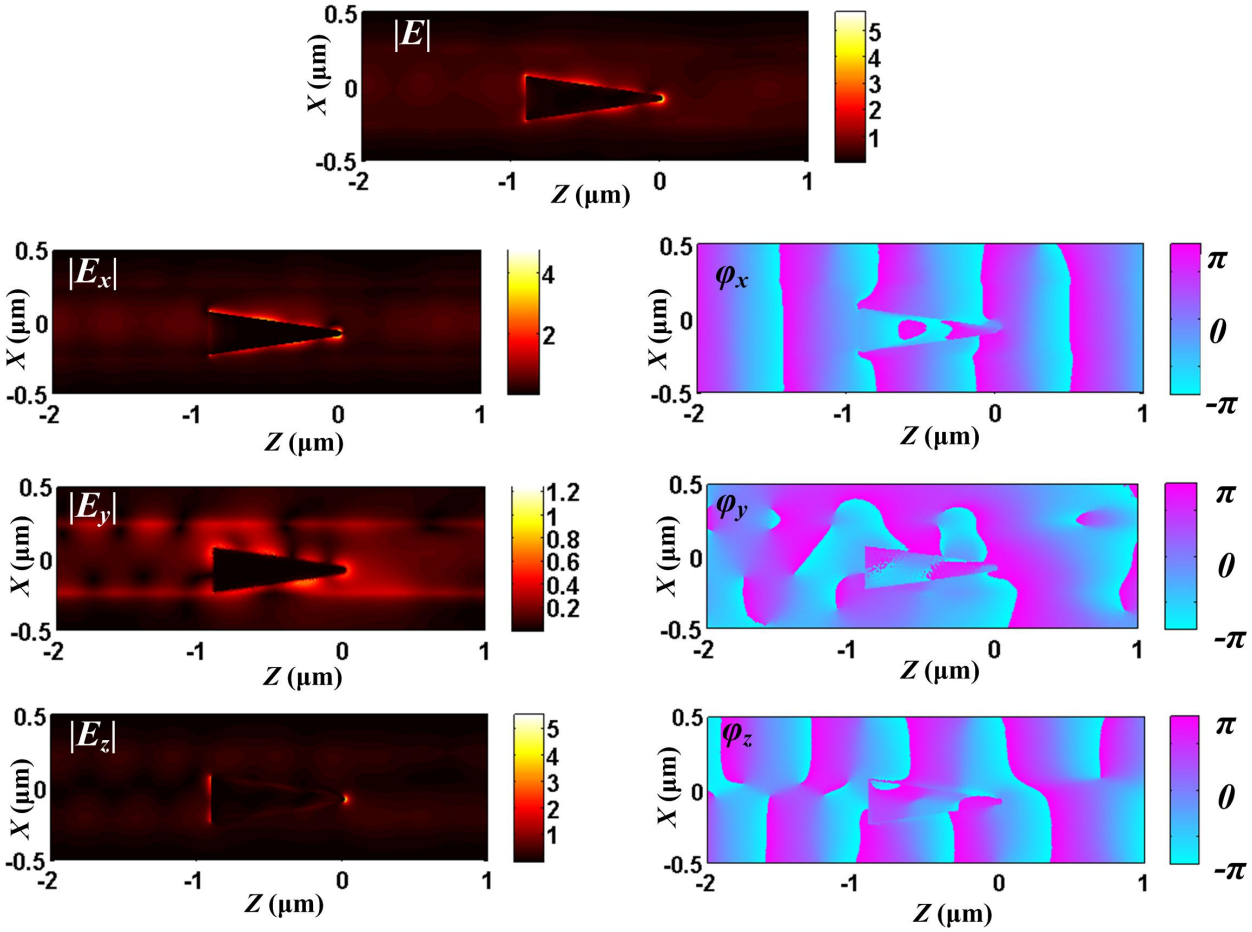

Figure 52: The upper panel is the electric field amplitude profile in the middle plane of the Au layer with a TE input. The amplitude (E_x, E_y and E_z) and phase (φ_x, φ_y and φ_z) of all three components of the electric field are shown in the following panels. The plasmonic nanotaper is shifted in the X direction of $80nm$ and has length $L = 900\,\mathrm{nm}$.

of the waveguide, the mode coupling becomes more complicated. With a quasi-TM input from the barewaveguide, TE-like supermodes will also be excited, and vice versa. The excited patterns from both polarizations of inputs are asymmetric, and in particular, a hot spot at the apex of the taper can be generated from a quasi-TE input with the maximum amplitude of E-field of about 5.5. For comparison, a purely quasi-TM input can generate a maximum amplitude of E-field of about 8.4.

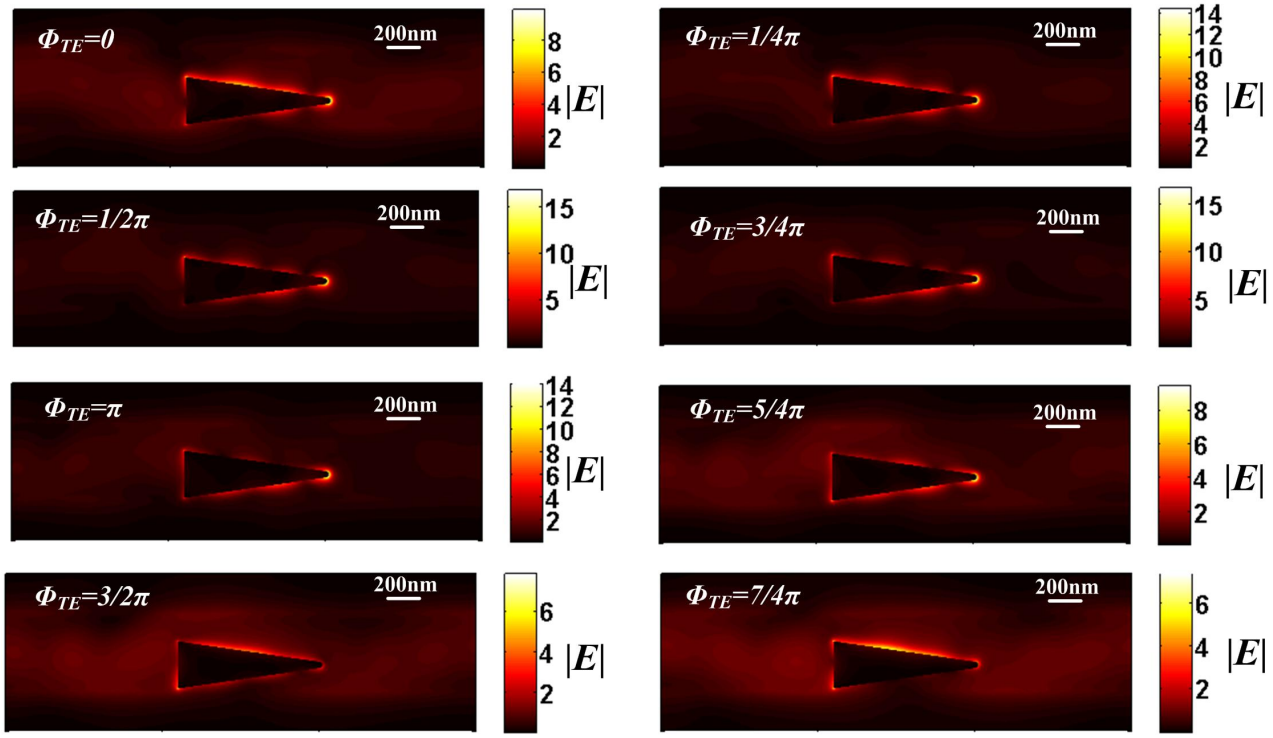

Figure 53: Interference patterns of E-field amplitude for a mixed TM and TE input with fixed phase φ_{TM} of TM input being 0 and varied phase φ_{TE} of TE input. The amplitude ratio of TM and TE inputs is $1 : 1.5$. The plasmonic nanotaper is shifted in the X direction of 80 nm and has length $L = 900$ nm.

Figure 53 shows the interference patterns on the nanotaper with a mixed input of TM-TE amplitude ratio $1 : 1.5$ and different relative phases. It can be seen that the maximum amplitude varies in a wide range ($7 \sim 14$) because both the quasi-TM and quasi-TE input can induce field concentration at the apex.

Figure 54 shows the FCF curves for different X-shift of the plasmonic pattern for values from 0 to 100 nm with a purely quasi-TM input. The FCF decreases and shifts

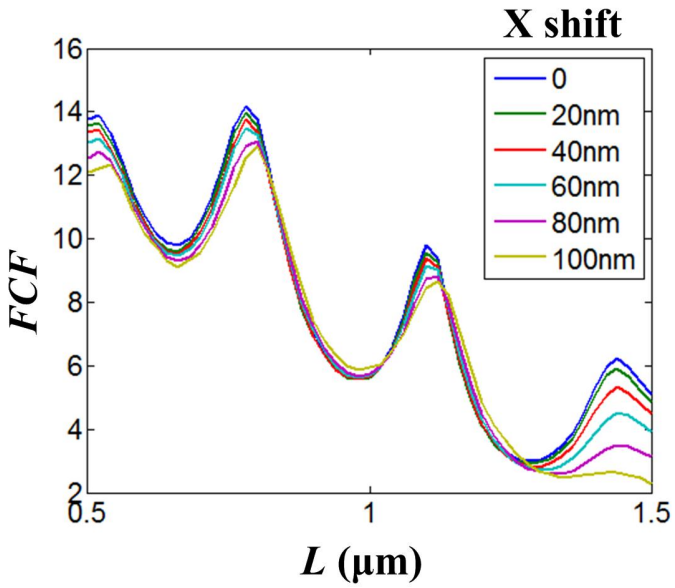

Figure 54: The FCF versus L curves for several values of X-shift of the pattern from the central line of the waveguide. The input is purely quasi-TM

as the X-shift of the plasmonic pattern increases, while the actually differences are small. This means the PLCs presented here are tolerant to the fabrication imperfection on alignment of the plasmonic patterns.

6.4 Experimental Demonstration of the Si-based Plasmonic Light Concentration using the NSOM System

Near-field scanning optical microscopy (NSOM) technique breaks the far field diffraction limit by exploiting the properties of evanescent waves. It is employed as a powerful tool for the investigation of the near-field optics in integrated optics devices. Historically, the original idea of imaging optical near-field was proposed to use the scattered light from a small particle or collected light through a tiny aperture to overcome the diffraction limit of conventional microscopy techniques [52]. These approaches lead to two main operation modes of current near-field imaging techniques: aperture-based mode and apertureless mode. Currently available NSOM systems fall into the category of scanning probe microscopy (SPM), whose probing tips are either metal-coated tapered optical fibers (aperture-based mode) or coated atomic

force microscopy (AFM) tips (apertureless mode). The AFM technique is also used to provide feedback control on probe scanning and keep the NSOM tip distance with the photonic structure surface constant. NSOM techniques have been used to image near-field intensity of the optical mode profile in different integrated optic devices, including waveguides [53], optical resonators [54], and plasmonic devices [55]. Recently, some people use NSOM systems to experimentally demonstrate the newly discovered plasmonic nanofocusing effects [40, 42, 44].

6.4.1 The NSOM systems used for measurements

NSOM measurements of our plasmonic samples were performed both in aperture-based mode in the photonics group at Georgia Institute of Technology and in apertureless mode in Laboratoire de Nanotechnologie et d'Instrumentation Optique at Université de Technologie de Troyes.

The NSOM system in our group is developed and modified from a commercially available NSOM system (Multi view 2000, Nanonics Inc.) to work in aperture operation mode. Figure 55 shows a schematic and a picture of this NSOM system. The input light comes from a tunable laser (HP7560, HP-Agilent) with tuning range $1520\,\text{nm} \sim 1580\,\text{nm}$ (optical communication wavelengths). Figure 55(c) is an SEM of an NSOM probe which is a tapered fiber tip coated with gold where there is an aperture of diameter about 200 nm on the tip. A fiber polarization controller is used to adjust the polarization. Light is coupled into a waveguide with a plasmonic light concentrator integrated on top, and NSOM signals are collected around the plasmonic pattern with tip-scanning controlled by a feedback system. A lock-in amplifier (Stanford Research Systems) is used to enhance sigal-to-noise ratio (SNR) from the optical detection of the NSOM signal. Both the AFM signal and NSOM signal are collected and data-processed to provide the topography and near-field images of the structure simultaneously.

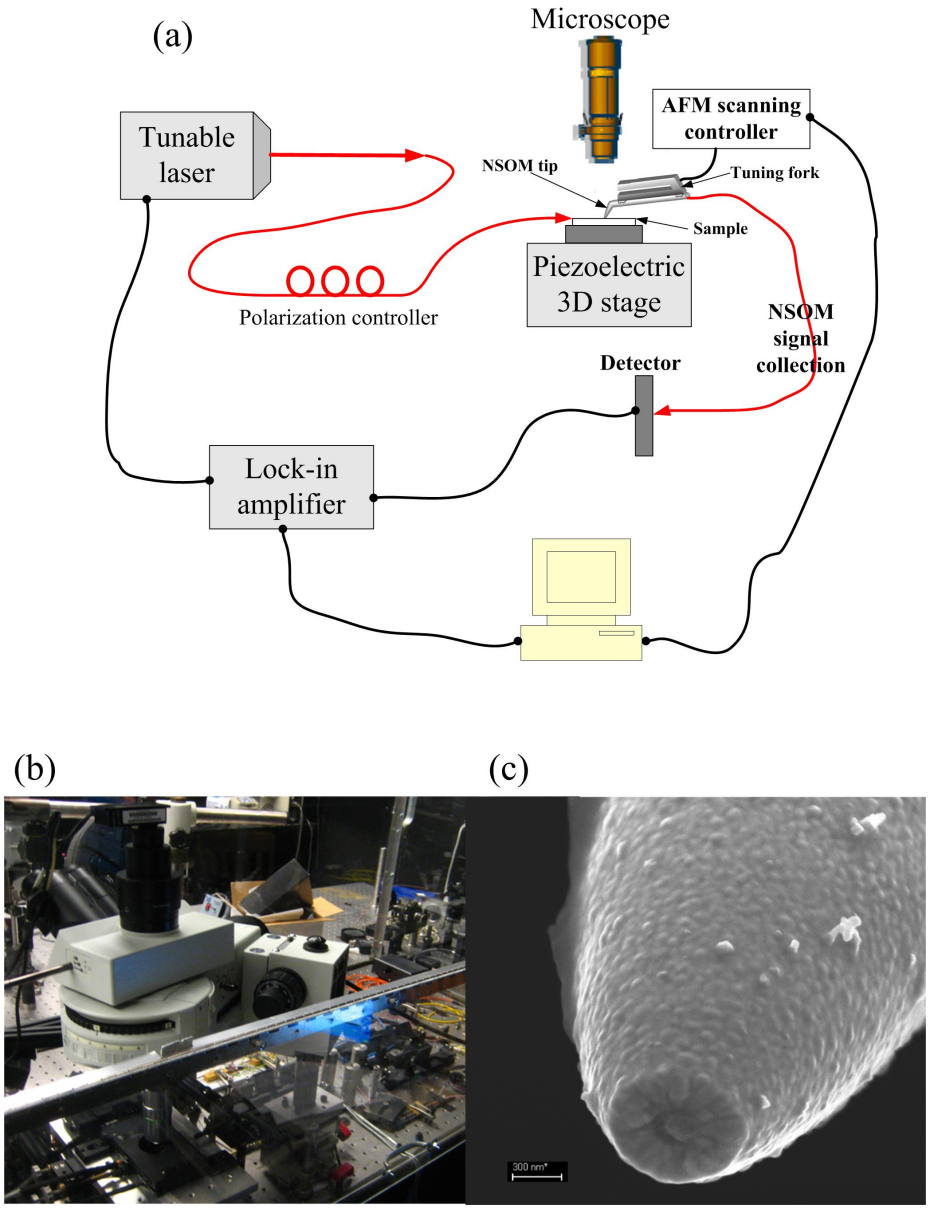

Figure 55: (a) Schematic of the characterization setup for near-field measurement. (b) A picture of the working NSOM system. (c) an SEM of an NSOM probe tip.

The plasmonic nanotaper is excited with a light input into the waveguide of input power about several milliwatts. The NSOM probe will scan the topological surface in the area around the plasmonic pattern, and the aperture of the probe will collect light intensity information at each pixel when working in collection mode.

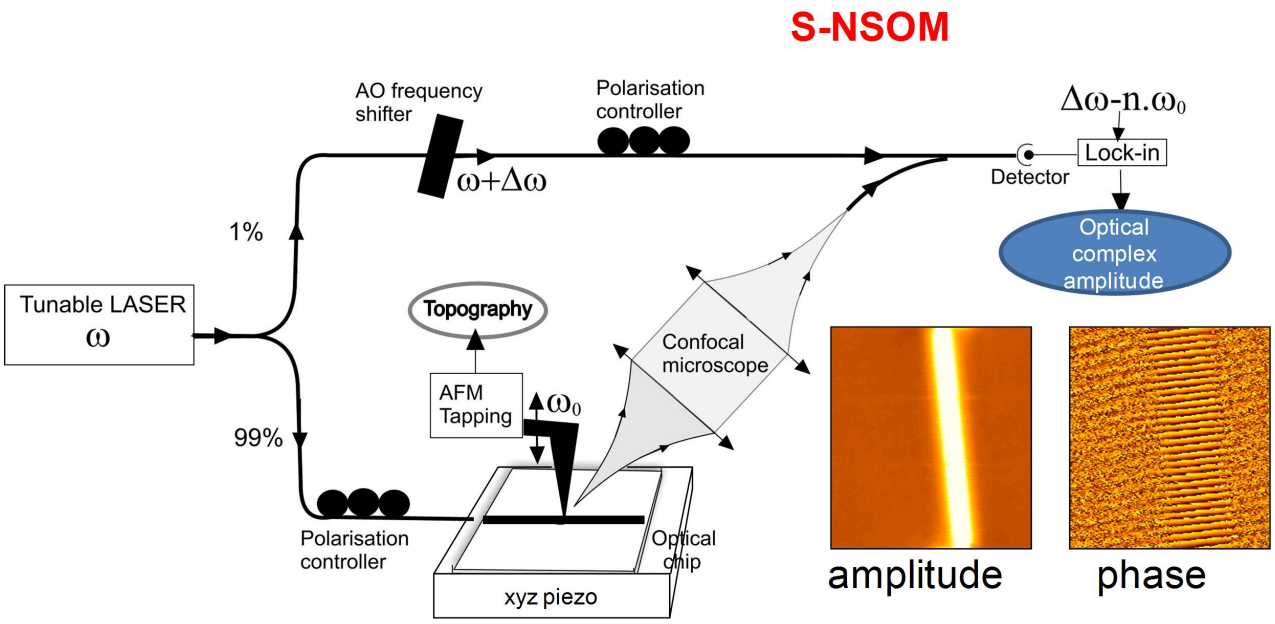

Figure 56: Schematic of the s-NSOM system. (Reproduced by courtesy of Aniello Apuzzo)

The NSOM system in LNIO at UTT is working in a heterodyne apertureless mode with an AFM tip as the NSOM probe. A silicon atomic force microscope (AFM) probe with a nominal apex diameter of 15 nm was used to locally probe the optical near field. Therefore, the resolution is a lot higher than the NSOM system at Georgia Tech. The experimental setup is equipped with polarization controllers and tapered lensed polarization-maintaining fibers to precisely control the polarization of the incident light. In addition, this system can work either as an s-NSOM ("s" stands for "scattering") or a p-NSOM ("p" stands for "perturbation"). In Figure 56, the system is tuned into scattering mode. The scattered light of the near field induced by the AFM tip is collected by a confocal microscope. And in Figure 57, the system

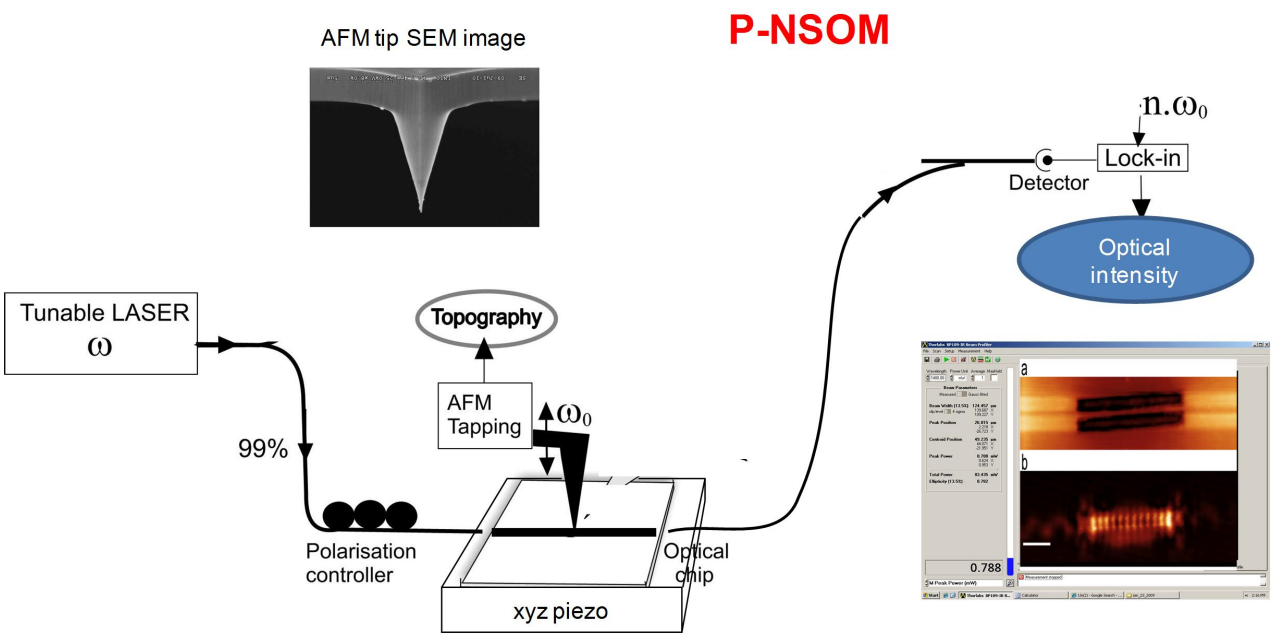

Figure 57: Schematic of the p-NSOM system. (Reproduced by courtesy of Aniello Apuzzo)

is tuned into perturbation mode, where the perturbation of the AFM tip on the near field is captured by directly measuring the transmission of the waveguide.

6.4.2 Experimental results

Figure 58 shows a measurement of near field on a PLC using the aperure-based NSOM system. Figure 58(a) is a top scattering pattern captured by a high definition IR camera. Because of some small roughness of the Si waveguide, one can see some light spots on the input region of the waveguide to the PLC (Figure 58(a)). The high intensity bright spot right upon the PLC shows that light energy transfers from the Si waveguide into the PLC. In contrast, after the PLC, the scattering from the Si waveguide is quite weak, which means a low transmission. Such a phenomenon is also confirmed by the near-field measurement (Figure 58(b)).

Now let us turn to discuss in more details the results from the heterodyne apertureless NSOM system whose resolution is a lot higher. The following work in this section is done in collaboration with Maysamreza Chamanzar, Aniello Apuzzo, Rafael

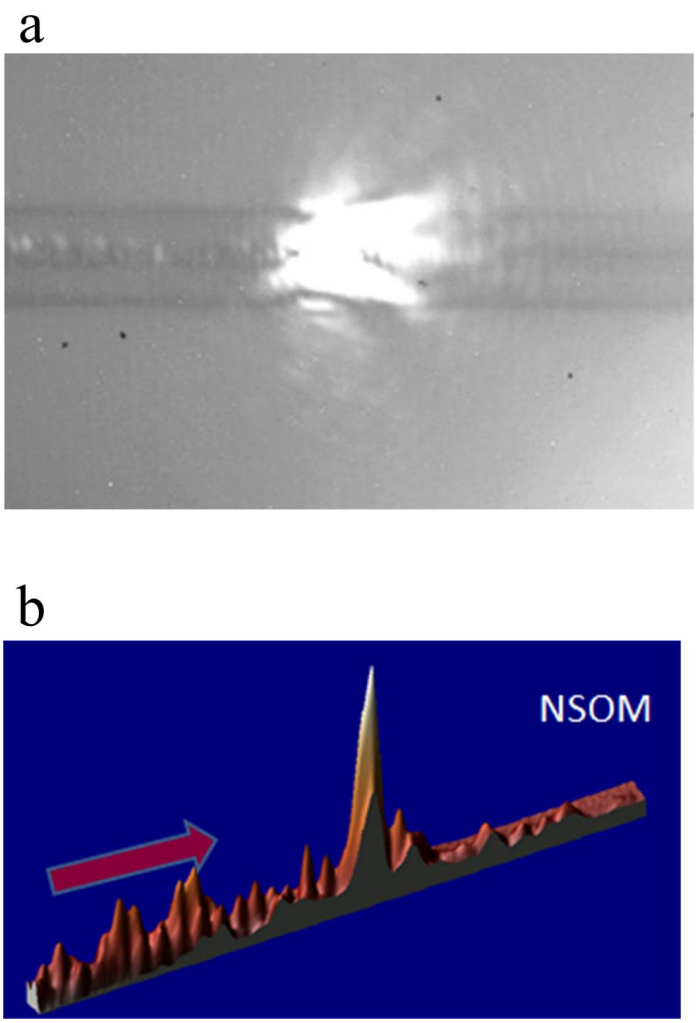

Figure 58: (a)Top scattering pattern of a PLC. (b) Near field measurement of light intensity by the aperture-based NSOM. The operation wavelength is 1550 nm.

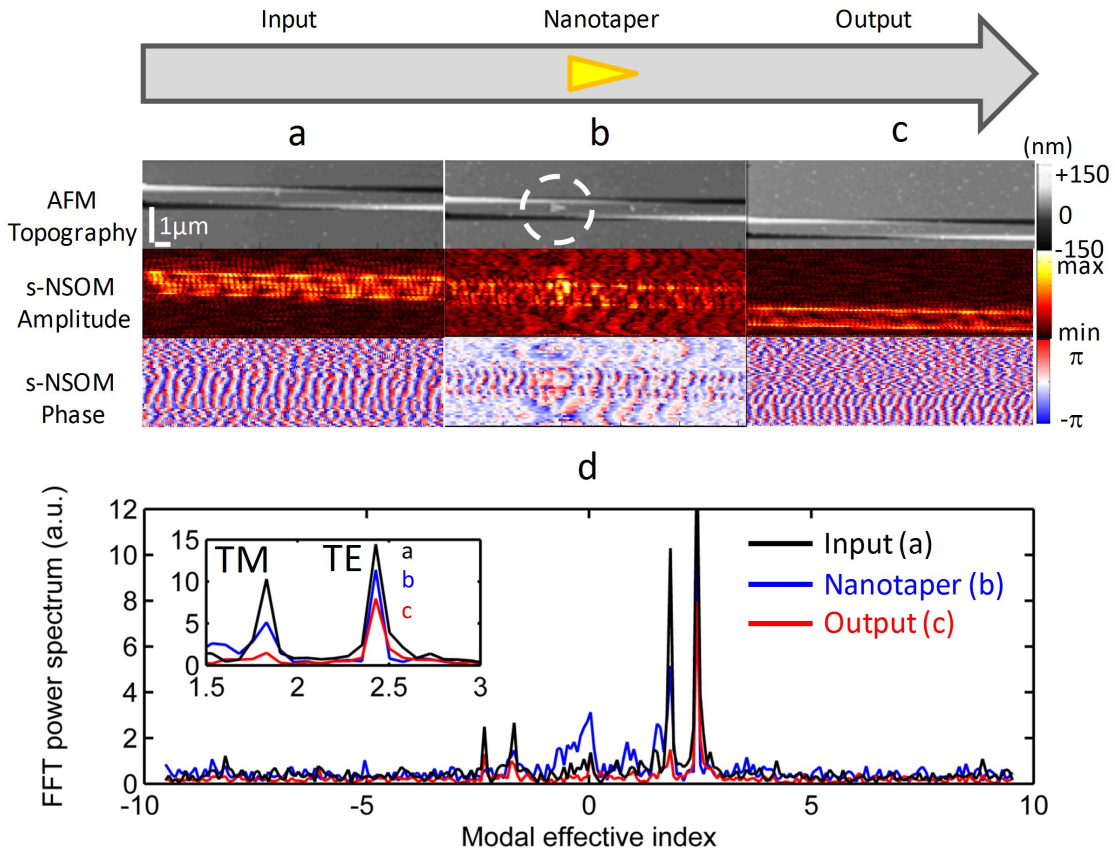

Figure 59: Measured optical near field along the integrated PLC under a light excitation at 1550 nm with an uncontrolled polarization. The upper panel represents the integrated PLC on a Si waveguide. (a) AFM topography of the Si waveguide in the input zone before the plasmonic nanotaper. Optical amplitude and phase NSOM images showing the multimodal behavior of the waveguide. (b) AFM topography around the plasmonic triangle (inside the white circle). 2D NSOM mapping of the hybrid coupler reveals a strong interaction between the triangle nanotaper and the Si waveguide (c) AFM topography of the bare waveguide taken immediately after the coupling zone. The light pattern is a clear manifestation of a TE-like propagating mode. (d) FFT spectra of the complex electric field profile as function of the modal effective index. Black, blue and red curves are referred to the three different zones, where the NSOM measurement was performed: on the input zone of the waveguide, on the hybrid structure region, and on the output part of the waveguide. The inset shows only the forward propagating modes, where it can be seen that the TM-like and TE-like modes are consumed differently in three parts of the sample.

Salas-Montiel and Sylvain Blaize [58].

In order to observe the behavior of the electromagnetic modes propagating along the structure, we first removed the polarizers to excite the PLC structure with elliptical light at the wavelength of 1550 nm. The experiments were conducted for a pattern with a plasmonic nanotaper of about 750 nm. We scanned the electromagnetic modes along the structure at three different locations, in the input waveguide (Figure 59(a)), in the nanotaper zone (Figure 59(b)), and in the output waveguide (Figure 59(c)), respectively.

Figure 59(a) reveals a lightwave pattern characterized by a field highly concentrated both on the edges and on the top center of the bare waveguide. This observation indicates that both the fundamental TM-like and TE-like modes propagate in the Si waveguide. As a result, the two co-propagative modes induce a longitudinal periodic pattern in the near field profile that is also clearly visible. In addition, we observe very short longitudinal oscillations due to interferences between propagative and contra-propagative waves produced by reflections from the PLC and from the waveguide output facet.

The beating pattern produced by TM-like and TE-like modes is also visible in the phase image (shown in the bottom row of Figure 59(a), (b), and (c)), where we note a distortion of the wavefronts, and also many phase singularities at some points where the field vanishes due to destructive interferences of different modes. As expected, we observe an enhancement of the optical near field signal at the PLC location indicated by the white dashed circle in the topography image (Figure 59(b) middle row). Moreover, part of the incident light also couples to radiative modes as confirmed by the presence of concentric wavefronts in the phase map in Figure 59(b). An interesting observation from the amplitude and phase maps is that the interference mode beating is more pronounced in the input region and vanishes at the output region (Figure 59(c)). Also, it can be seen from Figure 59(c) that light is mostly

confined at the edge of the waveguide, implying the existence of TE-like modes at the output region. This plot shows that the TM-like mode is mostly coupled to the plasmonic nanotaper and is "consumed", whereas the TE-like mode passes through the plasmonic nanotaper region with minimum interaction. It was expected from our theoretical analysis that the fundamental TM-like mode in the Si waveguide has a stronger coupling to the plasmonic nanotaper.

To quantify these qualitative observations, we performed a spatial Fourier analysis of the complex electric field along the direction of propagation using fast Fourier transform (FFT) to obtain the mode propagation constants. As shown in Figure 59(d), the black curve shows the fundamental harmonics of the TM-like and TE-like modes in the input region before the plasmonic nanotaper with the effective index values of $n_{\mathrm{TM}} = 1.83$ and $n_{\mathrm{TE}} = 2.43$, respectively. These values agree with the simulation results of $n_{\mathrm{TM}} = 1.6105$ and $n_{\mathrm{TE}} = 2.3977$. The forward propagating modes are indicated by positive effective index values and the backward propagating guided modes are indicated by negative effective index values. The amplitudes of the FFT spectra show the power spectral density of the modes. It is evident from the inset of Figure 59d that the power of the fundamental TM-like photonic mode (TM_0) is significantly decreased after passing through the plasmonic nanotaper due to the coupling to the plasmonic modes compared to the power of the fundamental TE-like mode. The transmittance, defined as the ratio of the output power to the input power for the TM_0 mode (inset of Figure 59d) can be obtained as $T_{\mathrm{TM}} = 2\%$. In order to estimate the PLC intrinsic reflectance R_{TM} we have to take into account the reflection coming from the waveguide output facet, say R_{output}. Then, from the overall reflection R_{input} measured from Figure 59a in the input waveguide, we obtain $R_{\mathrm{TM}} = R_{\mathrm{input}} - R_{\mathrm{output}} = 6\%$. Therefore, the power lost by the PLC (scattering and absorption), amounts to $P_{\mathrm{Extinction,TM}} = 92\%$. In an analogous way, the experimental transmittance and reflectance for TE-like incidence are estimated to be $T_{\mathrm{TE}} = 32\%$

and $R_{\mathrm{TE}} = 2\%$ respectively, leading to $P_{\mathrm{Extinction,TE}} = 66\%$. The strong extinction of the TM incidence confirms that this mode strongly interacts with the PLC as expected from the simulations.

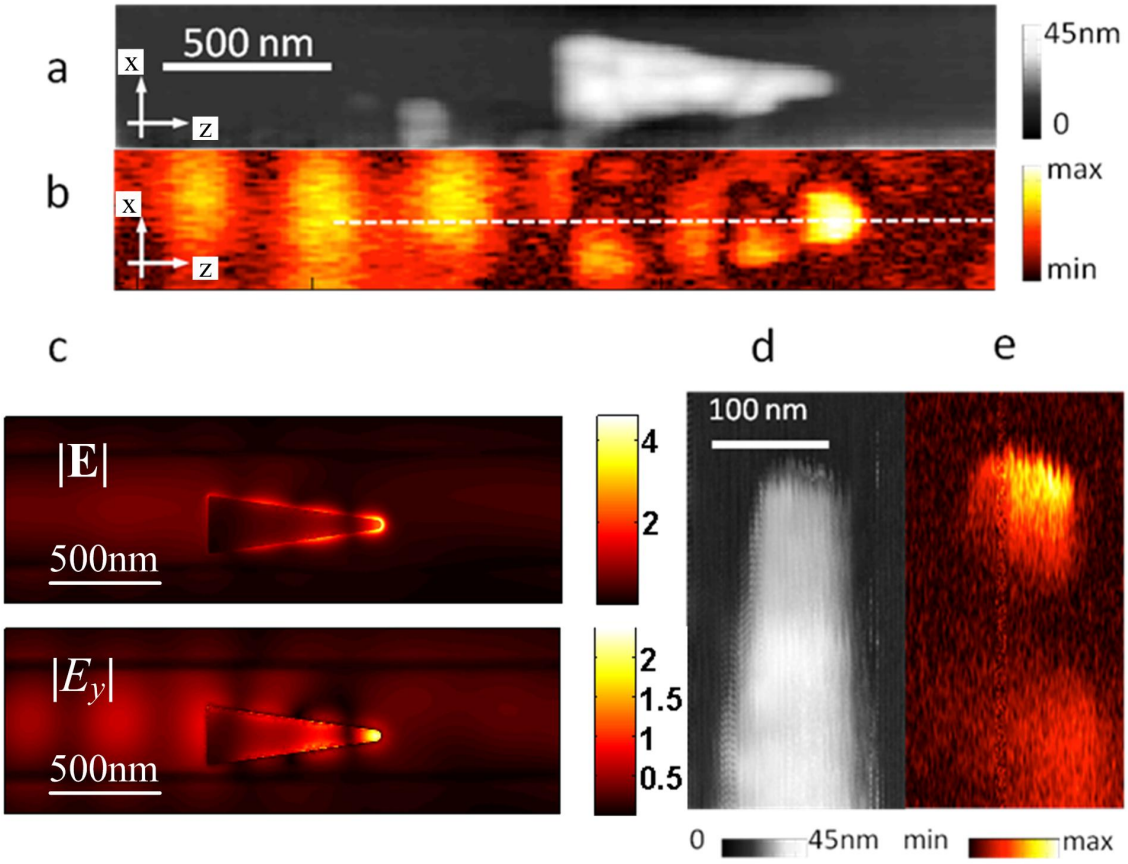

Figure 60: Measured optical near field along the integrated PLC under TM-like photonic mode excitation:(a) AFM topography and (b) optical near field amplitude around the PLC on silicon waveguide. (c) Simulated profiles ($|\mathbf{E}|$ and $|E_y|$) of electrical field amplitude on the surface 20 nm above the geometric surface around the plasmonic pattern. (d) AFM topography and (e) high-resolved NSOM images of the PLC at the tip of the triangle.

To go further in the experimental investigation, we fixed a TM-like incidence, and we performed a higher resolution NSOM scan over a small area on top of a plasmonic nanotaper (Figure 60). This nanotaper pattern under measurement has some shift from the central line of the waveguide. However, it barely affects the concentration efficiency as demonstrated in the FCF curves in the Figure 54. Figure 60(b) and

60(e) clearly demonstrates the strong nanofocusing of light at the apex of the PLC.

In addition, a standing wave pattern in a region just before the PLC can be observed as a result of the interference between the forward and backward TM-like modes originating from the reflections caused by the mismatch between the photonic waveguide mode and the hybrid modes in the PLC region. It can be seen that the amplitude profile has a strong peak at the apex. To obtain the effective mode volume of the concentrated electric field, we have measured the lateral profiles as well. The longitudinal confinement along the z-axis profile can be characterized by the full width at half maximum of the squared electric field profile as $\triangle z_{\mathrm{FWHM}} = 130\,\mathrm{nm}$ and similarly the lateral confinement along the perpendicular direction (not shown) can be obtained as $\triangle x_{\mathrm{FWHM}} = 100\,\mathrm{nm}$. The experimental results indicate that the effective area of the focused spot at a plane on top of the plasmonic nanotaper is thus $A_{\mathrm{eff}} = \triangle z_{\mathrm{FWHM}} \triangle x_{\mathrm{FWHM}} = 0.013\ \mu\mathrm{m}^2$. This value is a direct measure of the effective mode area and is thus a confirmation of sub-wavelength concentration of electromagnetic radiation. The experimental effective volume ($V_{\mathrm{eff}} = A_{\mathrm{eff}} \bullet \triangle y$) of the electric field energy density around the apex of the nanotaper could not be measured since precise scanning of the near fields along the y-axis ($\triangle y$) is not easily possible. An estimation of the field confinement along the vertical direction, however, can be carried out using the method discussed in [56]. The calculated effective volume is thus $V_{\mathrm{eff,cal}} = 0.00086\ \mu\mathrm{m}^3$, a mode volume that is 177.5 times lower than the limit of diffraction in all three dimensions ($V_{\mathrm{eff,cal}} = 0.00563(\lambda/(2n(\mathbf{r}_{\mathrm{max}})))^3$). Therefore, we estimate the vertical extent of the concentrated mode to be $\triangle y = 70\,\mathrm{nm}$. Here, $n(\mathbf{r}_{\mathrm{max}})$ is the value of the index of refraction at the position maximum of the squared electric field. Through this calculation, we calculated the effective area at several xy-planes and we found that the maximum electric field energy density is confined into the oxide layer ($n(\mathbf{r}_{\mathrm{max}}) = 1.45$). Furthermore, the calculated effective area, taken at 20 nm from the surface of the gold nanotaper, is $A_{\mathrm{eff,cal}} = 0.0124\ \mu\mathrm{m}^2$, which agrees

with the experimental value.

The field concentration factor (FCF) is another figure of merit that quantifies the nanofocusing effect in the plasmonic structure. The direct measurement of FCF from our NSOM experimental results is not possible since the average electric field inside the Si core on a reference waveguide is not accessible. Moreover, it is hard to find a representative reference waveguide on the sample, since the coupling conditions vary from one waveguide to the other. However, we can measure the maximum field amplitude at the apex of the plasmonic triangle and compare it to the field on the surface of the same waveguide after the nanotaper tip along the dashed line in Figure 60(b), where the electric field amplitude is almost constant (the electric field at the point 400 nm after the nanotaper tip is actually picked as the reference). We define the ratio of these two fields as the enhancement factor (EF). The EF is then estimated from our experimental results to be ~ 12.5. For comparison, Figure 60c shows the simulation results of electrical field amplitude profiles simulated profiles ($|\mathbf{E}|$ and $|E_y|$) 20 nm above the surface of the metal, from which we can estimate an EF of 12.2 from the $|E_z|$ profile and 14.5 from the $|\mathbf{E}|$ profile. The experimental results and the theoretical estimations agree. The NSOM picks out more signal of E_y component than that of the other electrical field components, since the AFM tip is along the y -direction. The experimental results and the theoretical estimations agree well with a rough assumption on the average distance of the NSOM probe from the measured surface to be around 20 nm. It should be noted, however, that the scattering differential cross section of the NSOM probe is strongly influenced by its interaction with the structure. One consequence of this interaction is that the radiation pattern detected in the far field rapidly changes depending on the position of the probe relative to the sample and to the local field polarization [57]. In our simulations, we have focused on the behavior of the structure in the absence of the NSOM probe. Further research is needed in order to understand in detail the interaction between

the plasmonic nanotaper and the NSOM probe particularly at its apex and therefore, get a quantitative and reliable measurement of the field enhancement factor.

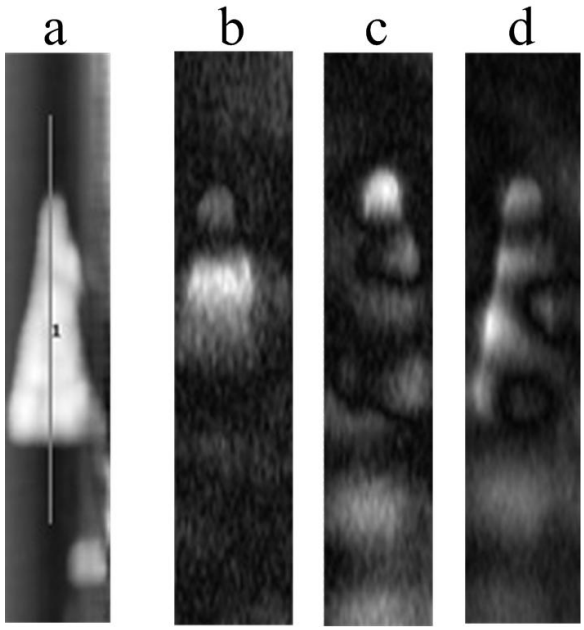

Figure 61: (a) An AFM of the plasmonic taper which is the same one as in Figure 60. (b) (c) (d) The p-NSOM images under several different input polarizations.

To compare the interference patterns on the plasmonic nanotaper with the existence of both quasi-TM input and quasi-TE input (Figure 53), we also took p-NSOM measurements for the same PLC under several different input polarizations, as shown in Figure 61.

CHAPTER VII

SOME APPLICATIONS OF ON-CHIP PLASMONIC LIGHT CONCENTRATORS

In this chapter, I propose two application of on-chip PLCs: one is on plasmonic nano-trapping, and the other is phase-induced local-field configuration.

7.1 Optical Trapping of Nano-particles

7.1.1 A review of optical trapping techniques

Compared to its invaluable ability in encoding and transmitting information about the world around us, light has a less prominent mechanical effect on material objects. Although this property of light has been known as early as when Maxwell's equations were discovered, optical forces used to be considered too weak for applications. In the 1980's, Ashkin and his colleagues demonstrated that optical forces can be used to confine or propel micro-objects [59]. This ground-breaking work inspired numerous followers to explore the possibilities of generating and taking use of optical forces with a combination of various techniques. This emerging field is called "optical trapping and manipulation" nowadays [60, 61].

Light scattering and absorption by an irradiated object result in an exchange of momentum between the incident photon and the object. An optical force is applied to the object due to its momentum change. When a micro-particle or a nano-particle whose refractive index is different from that of the ambient medium is placed very close to the focus point of a focused laser beam, two types of optical forces will be generated which can be considered separately in most cases. The first type of force is called scattering force, which comes from the radiation pressure of the light

that propels the particle in the direction of light propagation. The second type of force is called gradient force, which comes from the inhomogeneous distribution of light intensity. When the refractive index of the particle is higher than that of the ambient medium, the gradient force attracts the particle toward the location of the highest optical intensity. If the light beam is tightly focused with high enough power, then the gradient force can compensate the thermal force (Brownian motion) and the scattering force so that the particle is trapped in the region of high optical intensity. In particular, if the location of the beam focus is moving gradually, the particle will follow its movement as being tweezed. This makes the idea in Ashkin's original work [59], and the configuration is called an optical tweezer. In contrast, if the particle's refractive index is lower than that of the ambient medium, the gradient force pushes the particle away from the region of high optical intensity. In most experiments, the intensity of the incident light is in the range of a milliwatt (mW) up to a watt (W), and the generated optical force is in the range of tens of femtonewton (fN) up to tens of piconewton (pN).

After a development of more than 30 years, today's techniques for optical trapping and manipulation employ many novel configurations and lots of exciting applications have been found:

(1) Single-beam optical tweezers

The best-known tool of optical manipulation is still the optical tweezer invented by Ashkin and his colleagues, which is based on a single tightly focused beam. A protocol of how to set up an optical tweezer system is available in [63]. Nowadays such techniques have been commercially available [64].

(2) Dual-beam optical trap

This configuration is based on two counter-propagating moderately focused laser beams, which was also proposed by Ashkin in an earlier work [65]. One advantage of this configuration is that relatively low light intensity is required due to the

compensation of scattering forces between the counter-propagating beams. Modern adaptations of this configuration include low intensity 3D confinement dual-beam trapping [66, 67], dual-beam or multiple-beam fiber trapping schemes [68, 69] and optical stretchers [70].

(3)Rotation of micro-objects using optical forces

In addition to providing spatial confinements, optical forces can also transfer the angular momentum to the trapped objects and make them rotate. There are several different mechanisms to realize such light-induced rotations. The light itself can carry angular momentum. In particular, there are two kinds of light angular momentum. The first kind is called orbital angular momentum, which can be carried by Laguerre-Gaussian (LG) beams and be transferred to absorptive particles [71,72]. The other kind is called spin angular momentum, which can be carried by circularly polarized beams and be transferred to birefringent particles or shape-birefringent particles which are elongated along one axis [73–76]. Based on the same principle, a rotation of the polarization of a linearly beam will induce a rotation of the trapped birefringent particle [77–79]. Other techniques use objects with specially designed shapes [80,81] or tune the wave-front of the trapping beam by phase modulation [82].

(4)Trapping and manipulation using optical near-fields

An optical near-field is a non-propagating electro-magnetic field that exists very close to an optical interface and is usually in the form of an evanescent field/wave with light intensity decaying exponentially away from the interface. One conventional method of generating an evanescent wave from free space uses total internal reflection (TIR) at an interface between a glass prism and a medium (e.g. water) of lower refractive index. The gradient force caused by the intensity distribution of the evanescent wave attracts the particles to the surface, and the scattering force caused by the wave propagation can guide the particles along the wave propagation direction which is parallel to the surface. This is a technique of light-induced migration [83, 84]. By making

interference pattern on the surface, optical traps can be generated on the surface. Several optical sorting techniques (separation of particles of different nature) have been developed based on this principle [85–88]. Optical near-fields can also be generated by tapered optical fibers (nano-wires) [89, 90], waveguides, plasmonic structures and many integrated structures, which will be discussed more in the following parts.

(5) Trapping and manipulation with integrated optics

Techniques of optical trapping and manipulation using integrated optics started in the 1990's, when people found that the evanescent field of an optical waveguide could be used to trap and drive micro-particles [91]. Later on, further development of these techniques found applications in delivery, sorting and assembly of micro-particles and living cells [92–94]. These techniques fit naturally into the platform of optofluidics together with other "lab-on-a-chip" devices [95–97]. Using such an optofluidic platform, a remarkable recent achievement is a realization of trapping and transportation of nano-particles and biomolecules using slot waveguides [98]. To improve the trapping process efficiency, optical resonators are also included to enhance the optical field [99].

(6) Plasmon-induced trapping and manipulation

Among the optical trapping and manipulation techniques, those using plasmons are developed only recently. The first experimental observation of surface-plasmon-enhanced optical manipulation was reported in 2006, where the excited surface plasmon polaritons (SPP) in thin metal layers generated significant field enhancement to the near-fields, and thus the optical forces [100]. Trapping and manipulation of micro-particles can also be realized by near-fields generated by localized surface plasmons on patterned metallic surfaces [101] or around randomly distributed metallic nanoparticles [102].

Trapping of nano-particles is extremely challenging to conventional trapping techniques whose light confining abilities are restricted by the diffraction limit. Recall

that the magnitude of a trapping force is proportional to both the object volume and the light intensity gradient. Moreover, the thermal (or Brownian) motion becomes more prominent at nano-scale. Therefore, to generate an optical trapping force strong enough to compensate the thermal motion, the power of the trapping laser is required to be very high which can easily destroy the nano-objects. Plasmonic metallic structures are well-known for the unprecedented ability of breaking the diffraction limit and achieving large field enhancements in small volumes [104]. Therefore, in addition to the aforementioned applications of trapping and manipulation in the micro-scale, plasmonic techniques have tremendous potential in the area of nano-trapping. In recent years, several promising approaches using plasmons have been reported, all of which are based on metallic nano-structures including gap antennas [105, 108], nano-apertures made on gold films (using the so-called self-induced back-action effect) [106, 107], and gold nano-pillars [109].

7.1.2 Plasmonic Nano-Trapping based on-chip PLCs

The approach proposed here falls in the category of plasmonic nano-trapping. It is based on-chip PLCs discussed in the previous chapters, which is highly efficient in concentrating light from an photonic waveguide into nano-scale

I am going to demonstrate the ability of nano-trapping using the Si_3N_4-based PLC discussed for Figure 32 in Section 5.3.

When the radius of the particle is less than $1/20\lambda$, where λ is the light wavelength, a dipole model can be used to compute the optical force with reasonable accuracy. Let $\mathbf{E}$ be the complex electric field of a linearly polarized light beam, which can be expressed using the real amplitude $\mathbf{E}'$ and the real phase ϕ' as $\mathbf{E} = \mathbf{E}' \exp(i\phi')$. Denote the components of $\mathbf{E}$ by E_m and the components of $\mathbf{E}'$ by E'_m with m running through x, y and z. Let the polarizability α be expressed as

$$\alpha = \alpha_r + i\alpha_i = \frac{\alpha_0}{1 - \frac{2}{3}\frac{ik^3\alpha_0}{4\pi\epsilon_0\epsilon_1}} \simeq \alpha_0 + i\frac{|\alpha_0|^2 k^3}{6\pi\epsilon_0\epsilon_1}, \tag{28}$$

where ϵ_0 is the permittivity of vacuum, $\epsilon_1 = n_1^2$ is the relative permittivity of the ambient medium, $k = 2\pi n_1/\lambda_0$, and $\alpha_0 = 3\epsilon_0 V(\epsilon_2 - \epsilon_1)/(\epsilon_2 + 2\epsilon_1)$ with $\epsilon_2 = n_2^2$ being the relative permittivity of the particle and V being the volume of the particle. Then the optical force $\mathbf{F}$ acting on the particle has components

$$F_m = F_m^{grad} + F_m^{sca}, \tag{29}$$

where F_m^{grad} is a component of the gradient force and F_m^{sca} is a component of the scattering force. We have the following formulas:

$$F_m^{grad} = \frac{1}{4}\alpha_r \sum_{j=x,y,z} \frac{\partial_j (E_j'^2)}{\partial r_m} \tag{30}$$

and

$$F_m^{sca} = \frac{1}{2}\alpha_i \sum_{j=x,y,z} E_j'^2 \frac{\partial_j \phi'}{\partial r_m}. \tag{31}$$

Generally speaking, the gradient force is proportional to the product of the light intensity gradient and the volume of the particle. For larger objects, a general approach for force calculation is based on an integral of the Maxwell stress tensor [62].

Dielectric nano-particles used to be the most challenging object to be trapped because of their relative low contrast to the surrounding medium. Here I want to examine the performance of the PLC using a polystyrene nano-particle (refractive index 1.59) of diameter 20 nm. Note that in nano-scale, the scattering force can be overlooked. Therefore, I just consider the gradient force and use the potential well of trapping energy to describe the trapping ability. Suppose the power in the input bare waveguide is 1 mW. Figure 62 shows the potential well of trapping energy close to the metallic tip in the plane $Y = 320$ nm and $X = 0$. The force in the X-direction and Z-direction.

As shown in the figures, 1 mW of input power can generate a trapping energy of about $0.3k_BT$ (k_B is the Boltzmann constant and $T = 300K$ is a usually room temperature.) with a trapping spot of dimension about 10 nm. This is huge compared

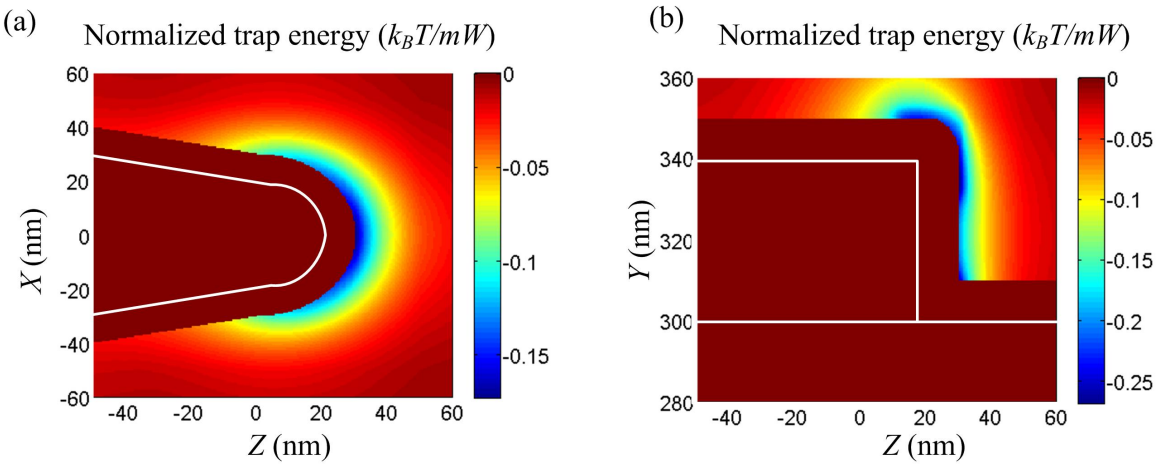

Figure 62: (a) Trap energy in the plane $Y = 320\,\text{nm}$. (b)Trap energy in the plane $X = 0$. The optical field computation comes from Figure 32.

to conventional approaches. In real fabrications, a tip radius is usually smaller than 20 nm. Therefore, we can expect higher trapping ability with smaller tip radius. And to achieve a trapping energy of $8k_BT$ (a criterion proposed by Ashkin), typically an input power of 10 mW should be enough.

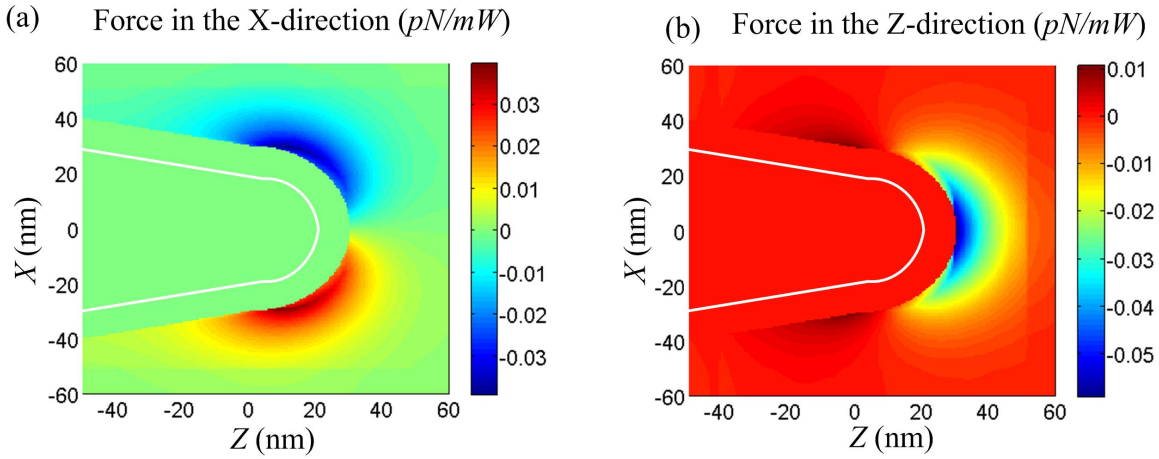

Figure 63: The force in the X-direction and Z-direction corresponding to the trap energy in Figure 62(a).

7.2 Phase-Induced Local Field Configuration

One of the biggest advantages of the plasmonic light concentrators in this dissertation is that our plasmonic device is directly mounted on top of a photonic waveguide while

the waveguide does not terminate. In other words, we can easily insert our device into optical circuits while the local concentrated optical field around the tip of the plasmonic taper is related to the optical transmission in the waveguide. Moreover, we can implement composite devices based on units made of individual plasmonic light concentrators.

In this section, we will discuss and analyze several composite structures based on individual PLCs. The first structure we will discuss is formed by two triangle-shaped plasmonic tapers facing each other mounted on top of one waveguide with two optical inputs into the two ends of the waveguide. The second structure we will discuss is formed by four plasmonic tapers mounted on two crossing waveguides with four inputs into the four ends of the waveguide.

For both structures, we are able to configure the local fields around taper tips by modulating the inputs into the two/four arms. If the inputs from different arm are incoherent, then the local field intensities are simply the sum of the intensities induced by each input. If the inputs are coherent, then the local field surrounding the tips is actually the result of interference of the local field induced by single-arm inputs. Therefore, we will be particularly interested in the effects of local field configuration by phase modulations of the two/four arms of inputs in the latter case. Moreover, we observe that such field configurations follow some logic behaviors.

7.2.1 Two-arm plasmonic tapers

As shown in Figure 64, our first structure is composed of two triangle-shaped plasmonic tapers mounted on a single photnonic waveguide. The two tapers are facing each other with a typical gap distance $< 100\,\text{nm}$. Since the two tapers are triangle-shaped (tapered-strip), the two inputs (left and right arms) are both set to TM-like mode. Generally speaking, the light concentration for the plasmonic taper on left is induced by the input from the left arm of the waveguide and the light concentration

for the plasmonic taper on right is induced by the input from the right arm of the waveguide.

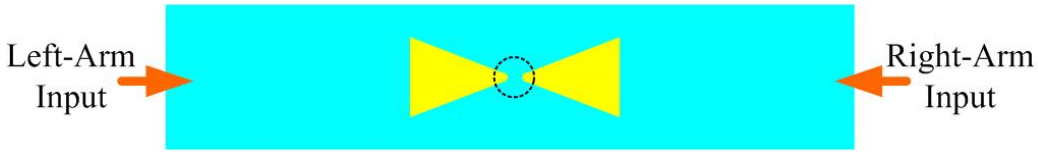

Figure 64: Schematic diagram of two-arm plasmonic tapers.

In the following, we will simulate and analyze the structure on a Silicon platform at wavelength 1550 nm. The dimensions of the waveguide follows from the previous chapter, i.e., the cross section of the silicon ridge having width of 500 nm and height of 220 nm, the silicon dioxide layer has thickness of 20 nm. We also assume the Au tapers to be ultra-compact. The thickness of the Au layer is 30 nm. The the width of the triangles is 300 nm and length of 400 nm. We set the radius of curvature at the tips to be 20 nm. We assume the gap distance (the distance between the two tip-ends of the tapers) to be 40 nm.

To demonstrate both the local near field around the taper tips and the optical transmission inside the waveguide, we will analyze optical fields in three planes: (1) plane 'A': the plane horizontally cutting through the Au layer (since the thickness of the Au layer is 30 nm, the distance between plane 'A' and the top plane of the Au layer is 15 nm), which represents the near field; (2) plane 'B': the plane 30 nm above the top layer of the Au layer, which represents both near field and scattering; and (3) plane 'C': the plane horizontally cutting through the silicon layer (since the thickness of the silicon layer is 220 nm, the distance between plane 'C' and the top plane of the Au layer is 110 nm), which represents the effect in the underlying photonic waveguide.

7.2.1.1 Single input from one arm

Before discussing the interfering patterns of the local field generated by two-arm inputs, we first discuss the case when the light input is only impinged into one arm.

Figure 65 shows the optical field profiles in the aforementioned three plane for a single optical input from the left arm or the right arm. This two-arm structure can be considered as two oppositely-facing PLCs. Roughly speaking, the left PLC concentrates the input light from the left arm to its taper tip and the PLC concentrates light from the right arm.

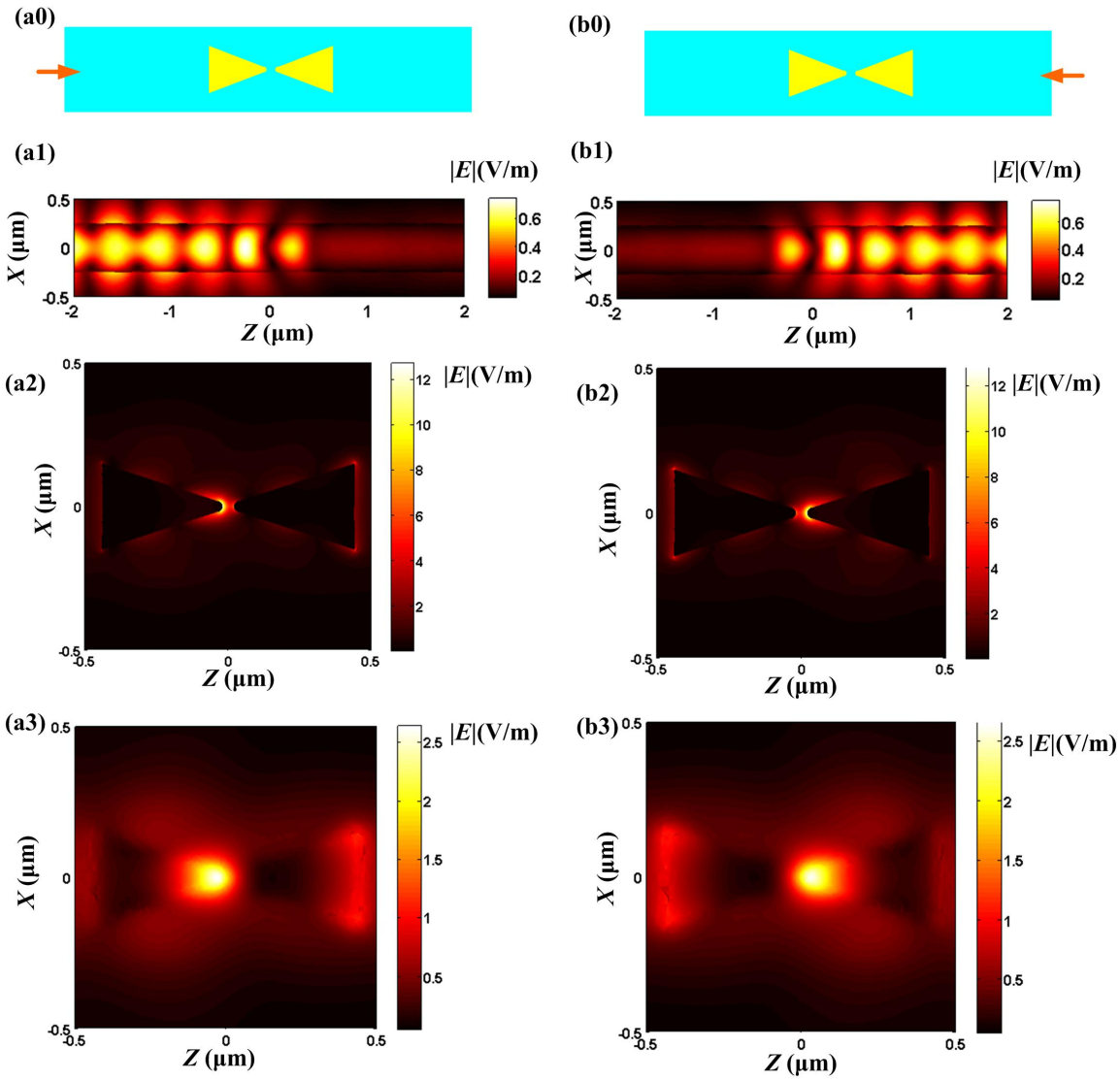

Figure 65: (a0) (a1) (a2) and (a3): light input from the left arm of the waveguide. (b0) (b1) (b2) and (b3): light input from the right arm of the waveguide. (a1) and (b1): optical field distributions in plane 'A' in the middle of the Au layer. (a2) and (b2): optical field distributions in plane 'B' above the Au layer. (a3) and (b3): optical field distributions in plane 'C' in the middle of the silicon layer.

Now let us consider the field of the left arm input in more details. Figure 66 shows the amplitude and phase of the z-component of the electric field in plane 'A' which is the middle plane of the Au layer. The reason we consider the z-component of the electric field is that it is the most prominent component around the tip of the plasmonic taper as a demonstration of field concentration, and analyzing the phase change of the z-component along the direction of wave propagation provides explanations to our further discussions on the interference patterns.

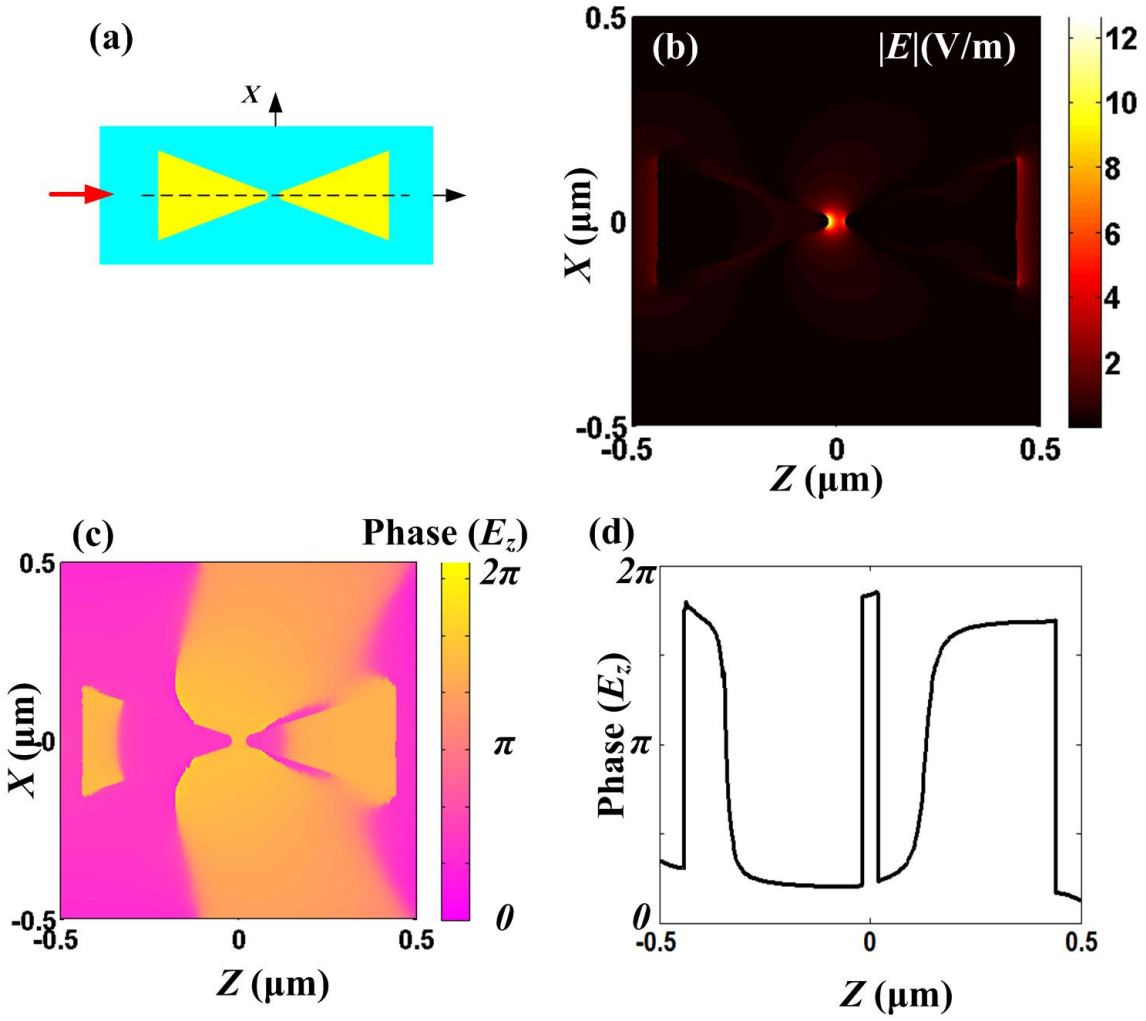

Figure 66: (a) Diagram of light input from the left arm of the waveguide. (b) Amplitude of the z-component of the electric field in plane 'A'. (c) Phase of the z-component of the electric field in plane 'A'. (d) Phase of the z-component of the electric field in plane 'A' along the dotted line in (a).

As shown in Figure 66 (c) and (d), the phase of E_z jumps up and down abruptly about $3/2\pi$ on the two boundaries of Au and air in the 40 nm gap. However, since the gap is so small, the phase of E_z does not change much in the 40 nm gap and can also be considered as a constant. By the same analysis, a symmetric input from the right arm will have the phase of E_z jumps inversely.

7.2.1.2 Phase induced configuration with inputs from both arms

In the above, we analyzed the phase change along the waveguide when there is only one arm of input. Now suppose we have both arms with inputs. If the two inputs of light are incoherent, the the light intensities are a simple summation of the light intensities induced by only one arm of input. This is a simple case, where we can configure the optical near field around the tips by the intensities of the two inputs.

A more interesting case is phase-induced configurations of the near field around the tips by changing the phase difference between the two input arms. There are many different ways of making phase modulation on waveguides, e.g., thermo-optically induced phase modulation. We can apply such phase modulations to one of the input arms. The local field pattern that is configured by the phase modulation is richer than the incoherent modulation of the optical intensities for each input.

Figure 67 shows the local field interfering patterns in plane 'A' when the phase of the left-arm input evaluated on a reference point in the input left arm is 0 and the phase of the right-arm input evaluated on the other reference point, which is a symmetric point of the first reference point, is Φ. Note that as long as the location of the two reference points are symmetric with opposite values of the z-coordinate, it does not really matter what exactly the z-coordinates of the reference points are as long as they are negations of each other. We have 8 value of Φ (0, $(1/4)\pi$, $(1/2)\pi$, $(3/4)\pi$, π, $(5/4)\pi$, $(3/2)\pi$ and $(7/4)\pi$) in this figure.

Let us first consider two opposite cases that $\Phi = 0$ and $\Phi = \pi$. As we have

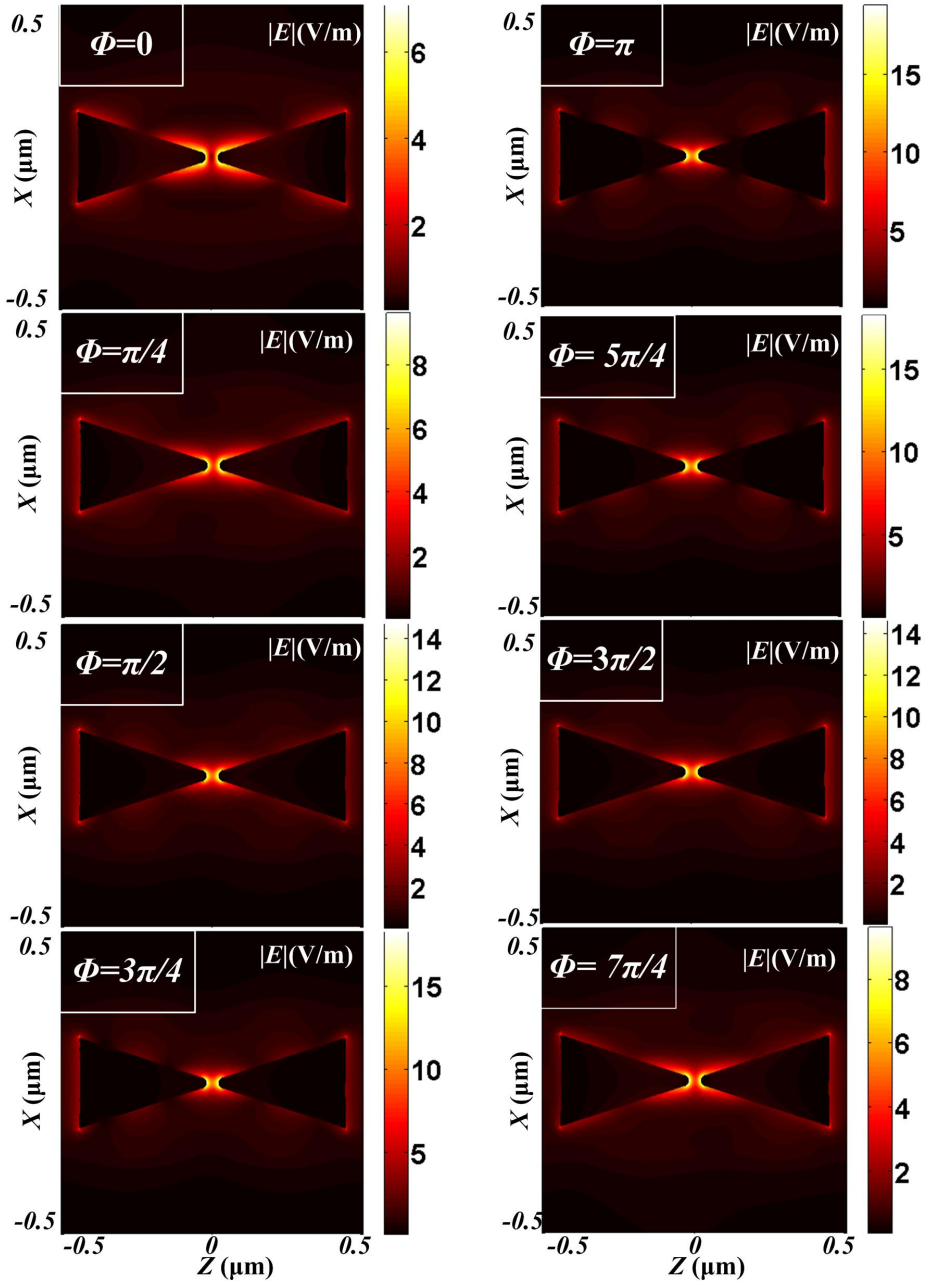

Figure 67: Local field profiles in plane 'A' for different relative phases between the inputs into the two arms.

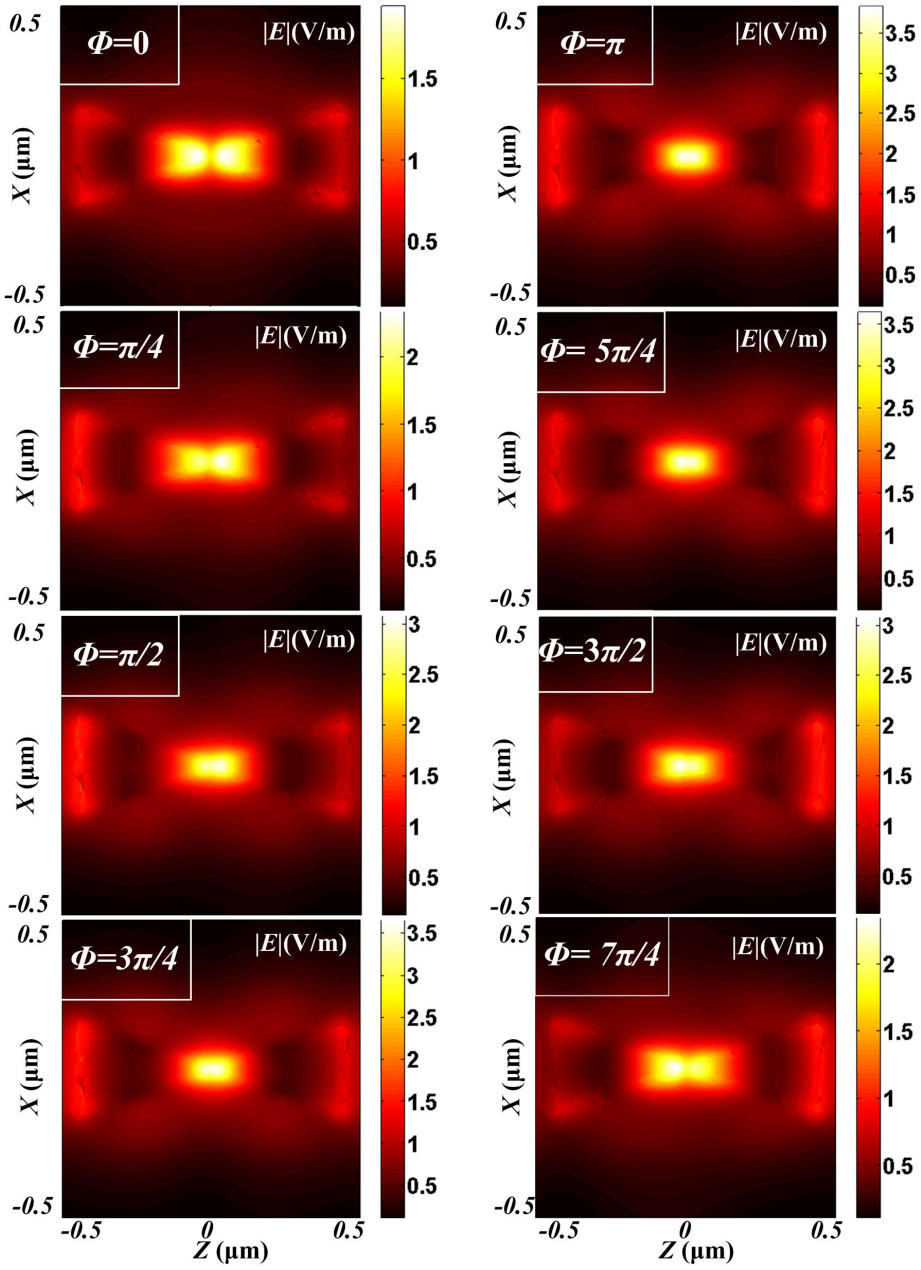

Figure 68: Local field profiles in plane 'B' for different relative phases between the inputs into the two arms.

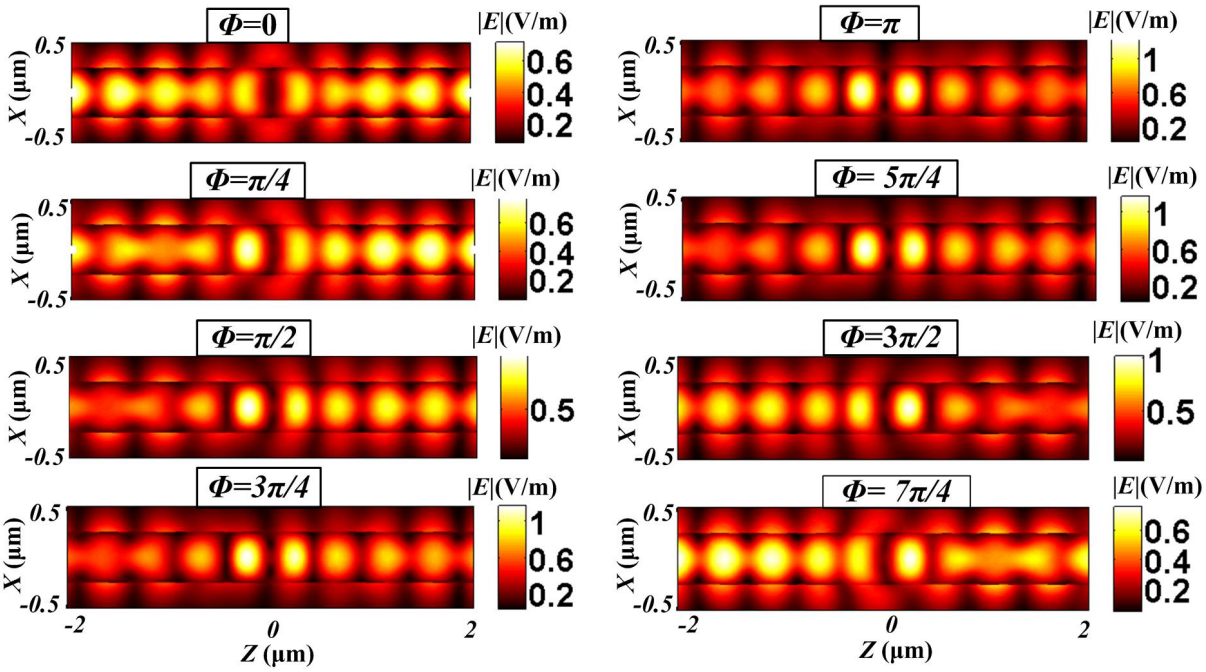

Figure 69: Local field profiles in plane 'C' for different relative phases between the inputs into the two arms.

discussed, the phase evolutions of E_z in Figure 66 show that in the whole 40 nm gap, the phase can be considered as a constant. If $\Phi = 0$, then the interference pattern in the gap is destructive. Descriptively speaking, the concentrated local field on each plasmonic tip is pushing each other away. The maximum value of the E-field amplitude from the colorbar reads 6.8. If $\Phi = \pi$, then the interference pattern in the gap is constructive. Descriptively speaking, the concentrated local field on each plasmonic tip is attracting each other in the gap region and the maximum value on the color bar is 18.5. It can be expected that such interference phenomena will be more prominent if the gap is even smaller (destructive becomes more destructive and constructive becomes more constructive). The patterns for the remaining values of Φ in Figure 66 are transitive status between the extremal state $\Phi = 0$ and the other extremal state $\Phi = \pi$. While not very easy to judge from just the patterns, it is more prominent by tracking the maximum values on the colorbars, which increases from a minimum value at $\Phi = 0$ to a maximum value at $\Phi = \pi$.

Figure 68 shows the field profiles in plane 'B' with various values of Φ as in Figure 67. Other than the maximum values in the colorbars, we can also observe that some patterns are asymmetric. For example, when $\Phi = \pi/4$, the bright spot in the pattern is stronger on the right than on the left, and when $\Phi = 7\pi/4$, the spot is stronger on the left.

Figure 69 shows the field profiles in plane 'C' which is the middle plane of the photonic waveguide. The patterns also follow the same rules. The pattern around $Z = 0$ for $\Phi = 0$ is weaker (destructive interference) than the pattern for $\Phi = \pi$ (constructive interference).

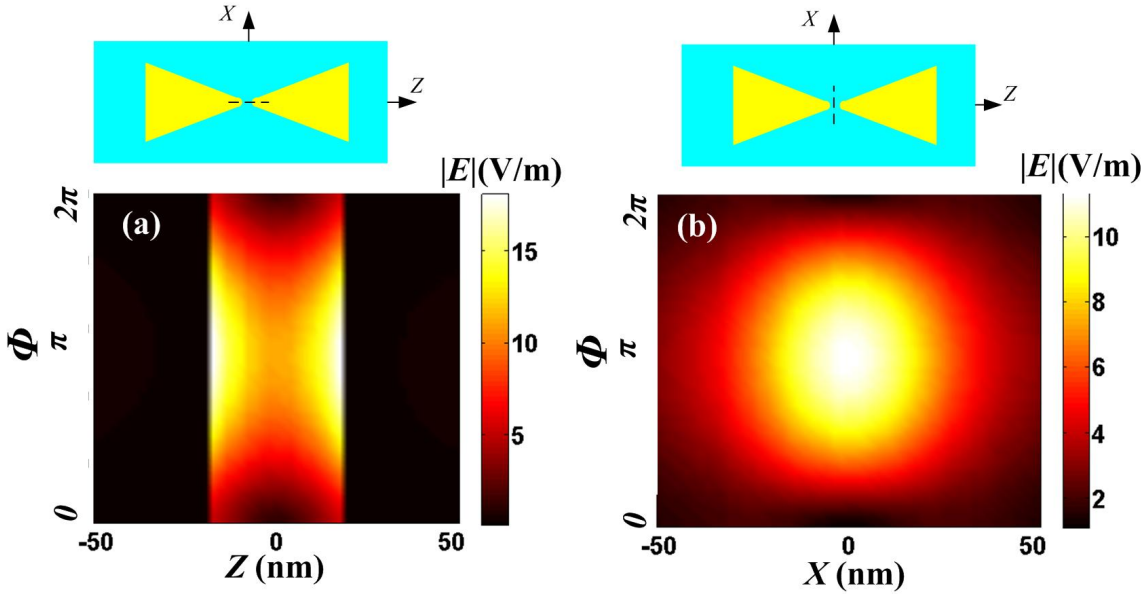

Figure 70: Field profiles around the gap in plane 'A' between taper tips with varying phase difference between the two input arms, (a) along the Z direction (following the dotted line in the schematic diagram above) and (b) along the X direction (following the dotted line in the schematic diagram above)

Figure 70 gives a more detailed analysis of the local pattern around the plasmonic tips in plane 'A' with Φ varying continuously from 0 to 2π. Figure 70(a) monitors the field profile along the Z direction and Figure 70(b) monitors the field profile along the X direction. Both of them show that the local pattern around the plasmonic tips is the strongest when $\Phi = \pi$ and weakest when $\Phi = 0$.

7.2.2 Four-arm plasmonic tapers

Our analysis in the previous section shows that we can realize local field configurations in an ultra small region ($\sim 100\,\text{nm} \times 100\,\text{nm}$) by amplitude or phase modulations on the two-arm inputs. In particular, the configuration induced by phase modulation has some binary logic behavior which makes it more interesting. In this section we will extend our analysis to two waveguides with four input arms. Similar binary logic behaviors still happen and we can have more refined modulation of the local filed around the plasmonic pattern.

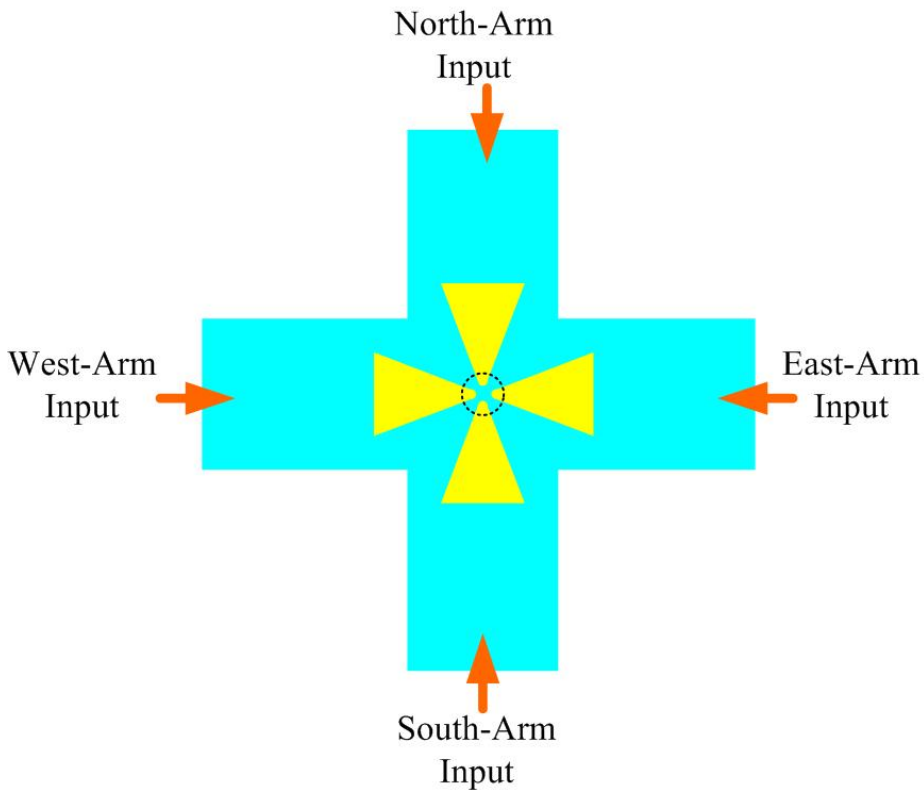

Figure 71: Schematic diagram of four-arm plasmonic tapers. Inputs are marked as east, west, south, and north arms.

Figure 71 illustrates the four-arm structure we will analyze. This four-arm structure can be considered as combining two of the two-arm structure in the previous section by crossing each other normally. We mark the four input arms by east, west, south and north respectively. We will divide our further study into four cases by the

number of inputs (one, two, three and four).

7.2.2.1 Single input from one arm (left arm)

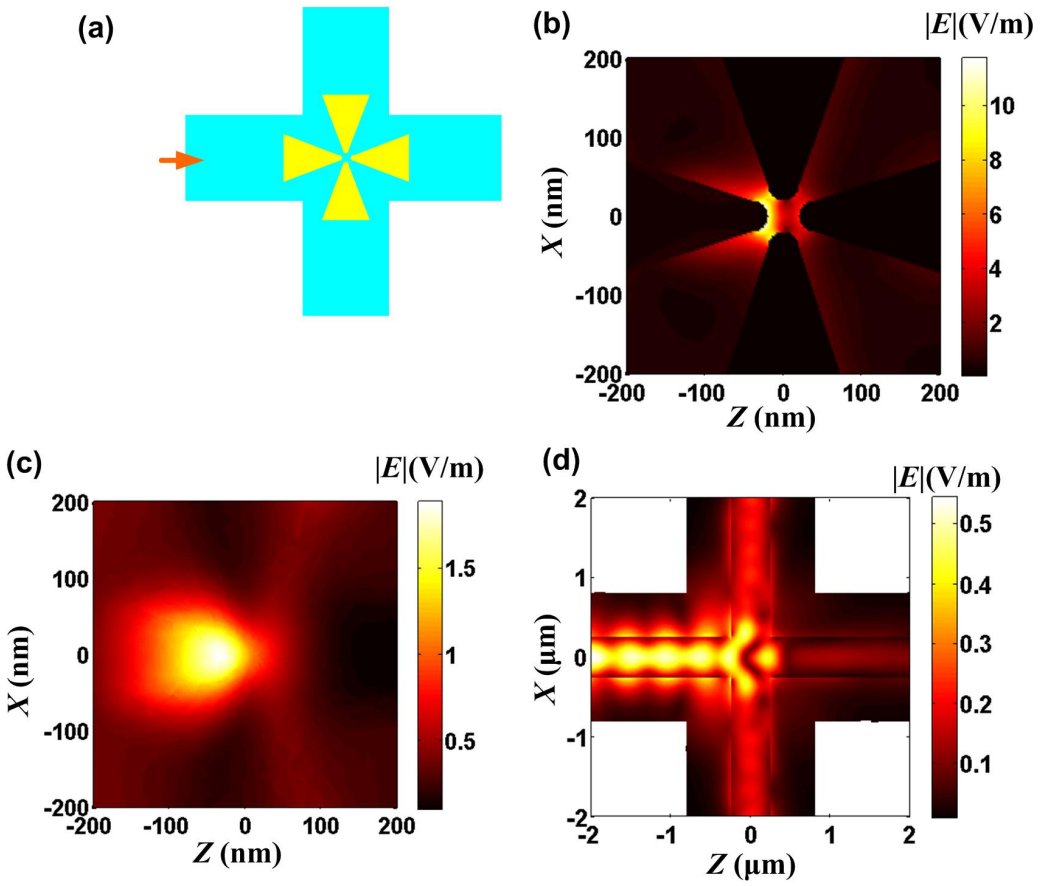

Figure 72: Single light input from the west arm. (a) The schematic diagram (b) Optical field distributions in plane 'A' in the middle of the Au layer. (c) Optical field distributions in plane 'B' above the Au layer. (d) Optical field distributions in plane 'C' in the middle of the silicon layer.

Figure 72 shows the field profiles in the three planes ('A', 'B' and 'C') when there is only one input from the west arm. The plasmonic taper on the left arm concentrates the light coming into the horizontal waveguide from the left arm. Since the plasmonic tips on the north and south arms are closer to the tip, we can see the local field extend from the west tip to the north and south tips prominently. We also can see that other than some transmission into the east arm in the same waveguide, the input light from the west arm also couples into the vertical waveguide, propagating to the north and

south arms. Based on the above phenomena, we conclude that one arm of light input can affect all the remaining arms both on the level of local field around the tips and on the level of light propagation in the photonic waveguides.

Therefore, we can expect that if there are more arms with inputs, then the patterns generated by single arms will interference each other. The seemingly complicated interference will still follow the 0-π binary logic behaviors as in the two arm case, since the one-arm input pattern shows that the phase around the tip area is still almost a constant and relative phase is 0 at two arm of inputs means destructive interference while relative phase is π at two arm of inputs means constructive interference. In the following analysis of interference pattern, we will focus on the cases when relative phases are 0 or π.

7.2.2.2 Local field configuration with inputs from two arms

In this subsection, there are two arms of inputs with the same amplitude and different relative phases. Figure 73 shows the case that the two arms of inputs are adjacent to each other (in particular, west arm and north arm). Figure 74 shows the case that the two arms of inputs are opposite to each other (in particular, west arm and east arm).

In Figure 73 (a0) (a1) (a2) and (a3), we suppose the phase Φ_W on a reference point on the west arm is 0 and the phase Φ_N on a corresponding reference point on the north arm is also 0. Note that we still follow the same rule of choosing the reference points by enforcing them to lie on the same plane with the same distance to the center of the structure. The actual distance does not matter. Now the binary logic is that a relative phase of 0 means destructive or repulsive interference. Therefore, we can observe from Figure 73 (a1) that there are two hot spots. One is in the gap between the tips on the west and south arms, and the other is in the gap between the tips on the north and east arms. The explanation follows exactly from the repulsive nature

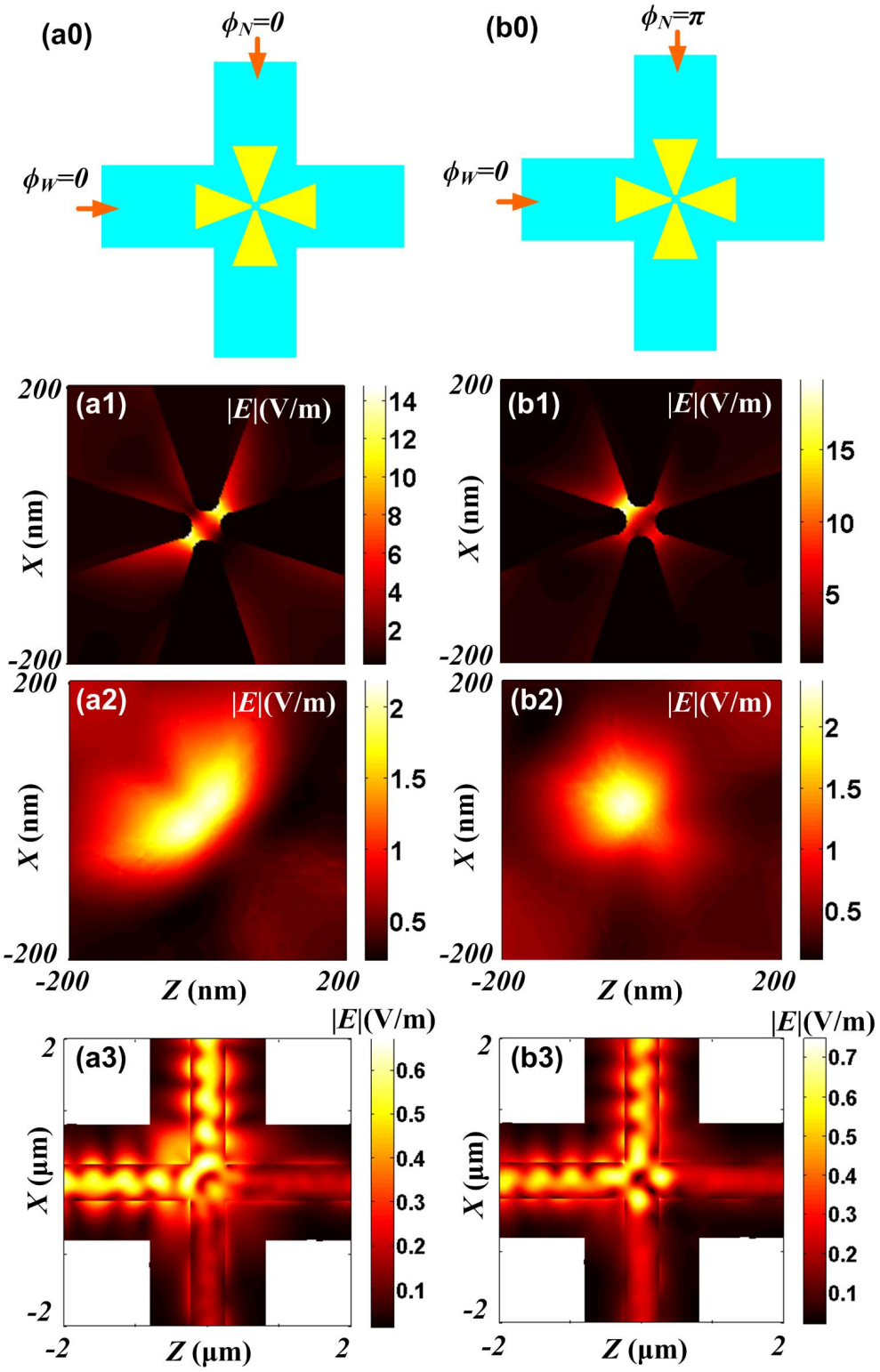

Figure 73: (a0) (a1) (a2) and (a3): two light inputs from the west and north arms with phase difference 0. (b0) (b1) (b2) and (b3): two light inputs from the west and north arms with phase difference π. (a1) and (b1): optical field distributions in plane 'A'. (a2) and (b2): optical field distributions in plane 'B'. (a3) and (b3): optical field distributions in plane 'C'.

of patterns generated by single arms when the relative phase is 0.

Now we may guess that the interference pattern will be an constructive or attractive pattern when the relative phase is π. This is exactly true as can be seen from Figure 73 (b0) (b1) (b2) and (b3) when Φ_W is still 0 but Φ_N changes to π. In Figure 73 (b1), there is only one strong hot spot between the west and north arms which means the interference is attractive.

Comparing Figure 73 (a2) and (b2), we observe that the an repulsive interference means a more diffusive pattern of scattering (Figure 73 (a2)) and an attractive interference means a more converging pattern of scattering (Figure 73 (b2)).

Now let us look at the case when the two arms of inputs opposite two each other on the same waveguide, i.e., the west arm and the east arm (Figure 74). The phase Φ_W of the reference point on the west arm is still fixed to 0, while we have the phase Φ_E of the reference point on the east arm being 0 for Figure 73 (a0) (a1) (a2) and (a3), and π for Figure 73 (b0) (b1) (b2) and (b3). Still, when the relative phase between the two arms is 0, the local field pattern around the tips is generated by repulsive interference, which can be seen from hollow spot in the the pattern of Figure 74 (a1) and the gap between two bright spot in the scattering pattern of Figure 74 (a2). Conversely, when the relative phase is π, we will have the local field pattern generated by attractive interference, while the maximum values of the amplitude of the electric field in the colorbars of Figure 73 (b1) and (b2) are much larger than the corresponding values in Figure 73 (a1) and (a2) respectively.

In Figure 73 (a3) and (b3), we can also see that the couplings to the north and south arms along the vertical waveguide are also affected by the inputs from the two arms. It appear that the couplings are stronger for $\Phi_E = \pi$ (attractive interference) than for $\Phi = 0$ (repulsive interference), which means the couplings to the vertical waveguide follow the same trend of variation as the local field around the tips for different relative phases.

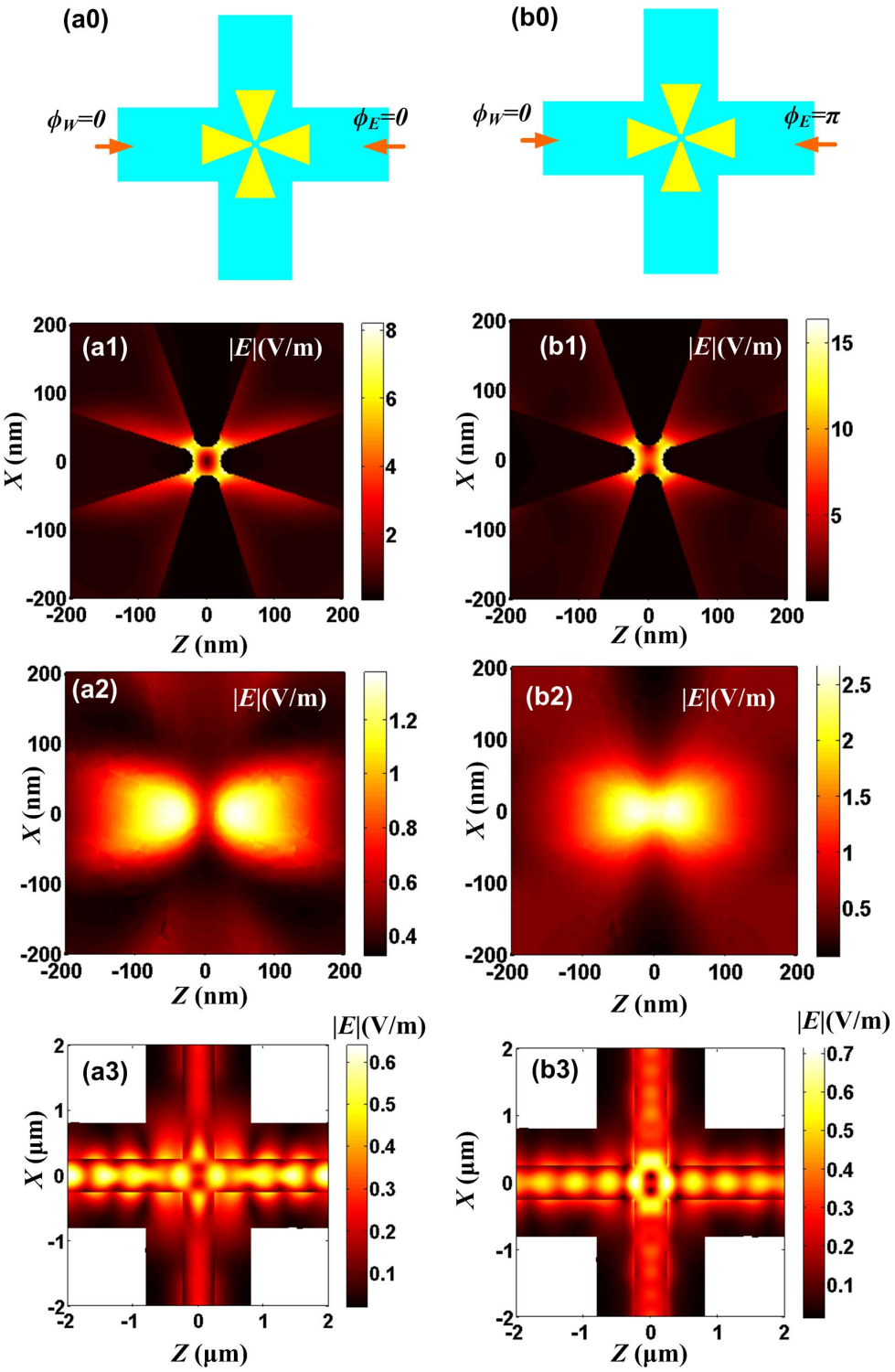

Figure 74: (a0) (a1) (a2) and (a3): two light inputs from the west and east arms with phase difference 0. (b0) (b1) (b2) and (b3): two light inputs from the west and east arms with phase difference π. (a1) and (b1): optical field distributions in plane 'A'. (a2) and (b2): optical field distributions in plane 'B'. (a3) and (b3): optical field distributions in plane 'C'.

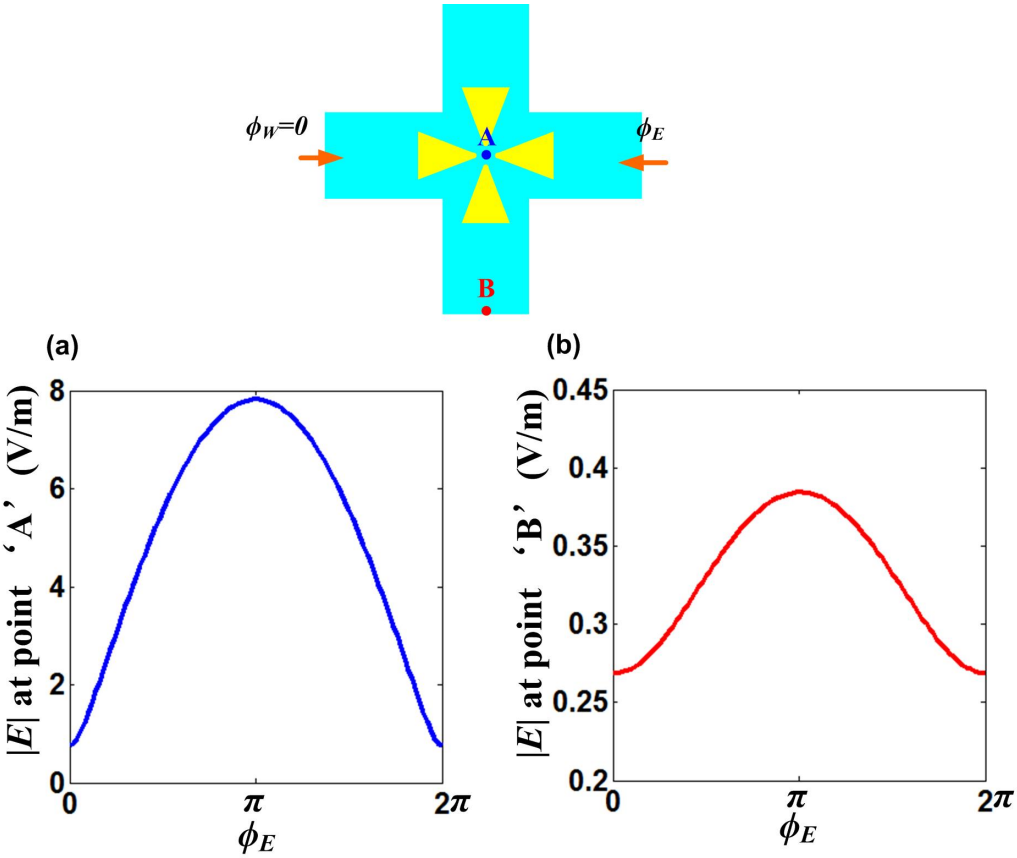

Figure 75: The optical field amplitude at (a) point 'A' in plane 'A' and (b) point 'B' in plane 'C' as in the schematic diagram above.

To confirm this expectation, we monitor the electric field at the central point of the structure (point 'A') in the middle plane cutting through the Au layer (plane 'A') and the electric field at a reference point in the south arm (point 'B') in the plane cutting through the waveguide (plane 'C'), as shown in Figure 75. Point 'A' represents the local electric field around the tips and point 'B' represents the couplings into the waveguide. We can see that both of them reach the minimum when $\Phi = 0$ and maximum when $\Phi = \pi$, and our expectation is confirmed.

7.2.2.3 Local field configuration with inputs from three arms

Now let us increase the number of inputs by one and we have three inputs from the west, east and north arms. For a consideration of symmetry, we force the phase Φ_W at the reference point in the west arm to be the same as the phase Φ_E at the reference point in the east arm. We may expect that the local field around the tips generated by interference between the two arms is destructive. Now the only arm with a varied phase is the north arm with phase Φ_N at the corresponding reference point.

The result is shown in Figure 76.

We can still apply our binary logic analysis. For Figure 76 (a0) (a1) (a2) and (a3), the phase Φ_N for the north arm input is 0, which is the same as the two other inputs from the west and east arms. Therefore, both the interference between the north-arm and west-arm inputs and the interference between the north-arm and east-arm inputs are repulsive. Therefore, the local field will reside in the remaining south arm with no inputs. From Figure 76 (a1), we can see that this is exactly the case with two hot spots in the gaps between the west and south tips and between the east and south tips.

Analogously, we can apply the same logic analysis to the case when $\Phi_N = \pi$ (Figure 76 (b0) (b1) (b2) and (b3)). Now both the interference between the north-arm and west-arm inputs and the interference between the north-arm and east-arm

inputs are attractive, which is confirmed by Figure 76 (b1) where there are two hot spots in the gaps between the west and north tips and between the east and north tips.

7.2.2.4 Local field configuration with inputs from all four arms

Now let us consider the case with inputs from all four arms with the same amplitude. We have the most flexibility of local field configuration since now we should control the phases (Φ_W, Φ_E, Φ_N, Φ_S) for all arms and have three free parameters when considering relative phases. We can generate several interesting local field patterns by adjust the parameters of phases. Only using the binary logic analysis as the previous analysis, we will be able to explanations to them.

In Figure 77 (a0) (a1) (a2) and (a3), all the phases on reference points in the four arms have the same value of 0 except the phase Φ_W from the west arm being π. Therefore, by the binary logic analysis, the interference between the west-arm input and an input from any of the remaining arms is attractive. As shown in In Figure 77 (a1), there are two hot spots in the gaps between the west and north tips and between the west and south tips, which is very much like the pattern in Figure 72 where there is only one input from the west arm.

In Figure 77 (b0) (b1) (b2) and (b3), all the phases on reference points in the four arms have the same value of 0. Therefore, the interference between any inputs from two arms is repulsive. As shown in In Figure 77 (b1), we can barely see a prominent hot spot. However, the scattering pattern shown in Figure 77 (b2) has a shape of "red cross" which is very interestingly looking.

In Figure 78 (a0) (a1) (a2) and (a3), we have the phases from the two arms in the horizontal waveguide being 0 and the phases from the two arms in the vertical waveguide being π, i.e., $\Phi_W = \Phi_E = 0$ and $\Phi_S = \Phi_N = \pi$. Also, by the binary logic analysis, the interference between any two adjacent arms are attractive. As shown

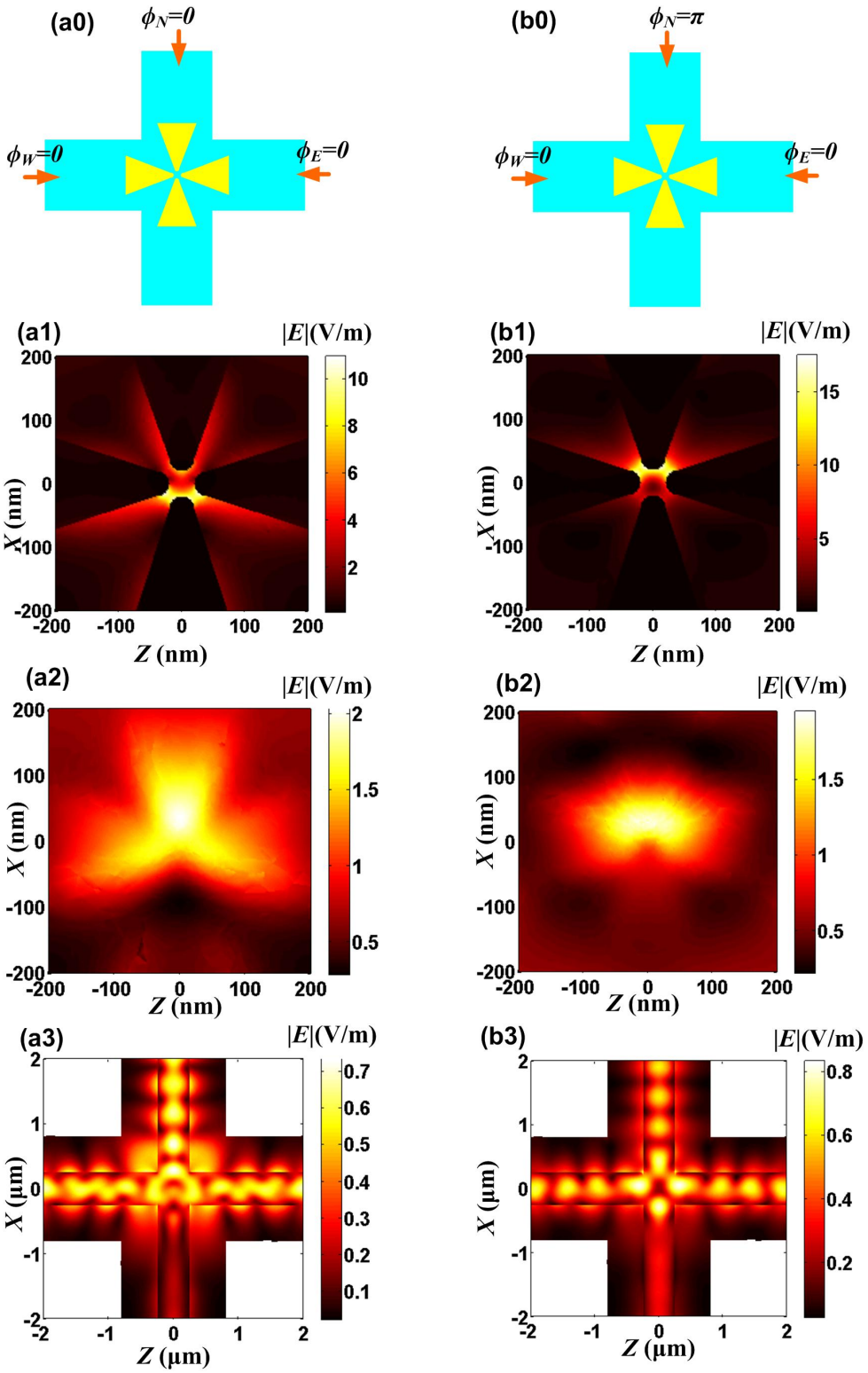

Figure 76: (a0) (a1) (a2) and (a3): three light inputs from the west, east and north arms with phase differences 0. (b0) (b1) (b2) and (b3): three light inputs from the west, east and north arms with the phase in the north-arm input being π and the phase in the other two being 0. (a1) and (b1): optical field distributions in plane 'A'. (a2) and (b2): optical field distributions in plane 'B'. (a3) and (b3): optical field distributions in plane 'C'.

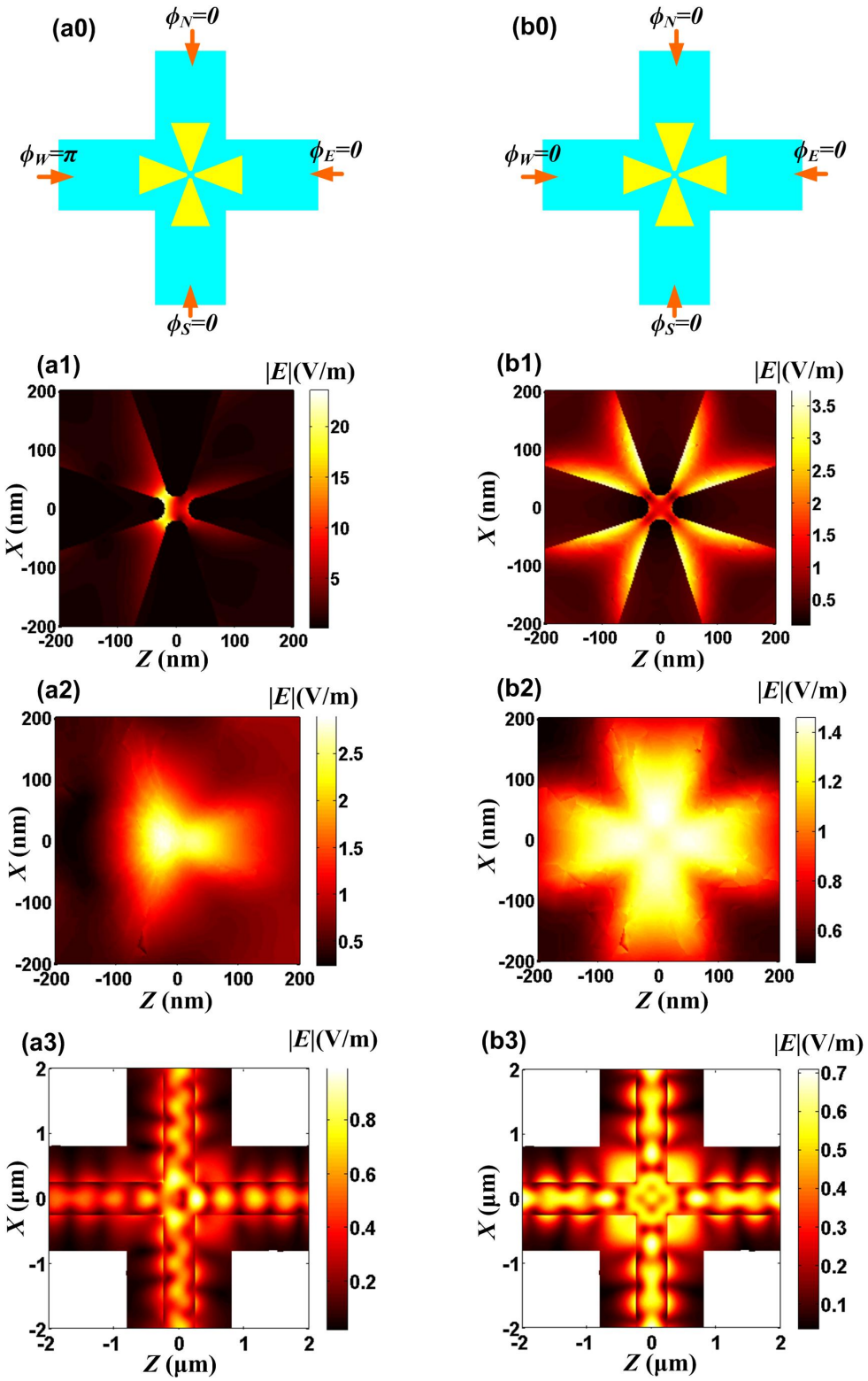

Figure 77: (a0) (a1) (a2) and (a3): four light inputs from all arms with the phase in the west-arm input being π and the phase in the other two being 0. (b0) (b1) (b2) and (b3): four light inputs from all arms with the phase difference '0' among all arms of inputs. (a1) and (b1): optical field distributions in plane 'A'. (a2) and (b2): optical field distributions in plane 'B'. (a3) and (b3): optical field distributions in plane 'C'.

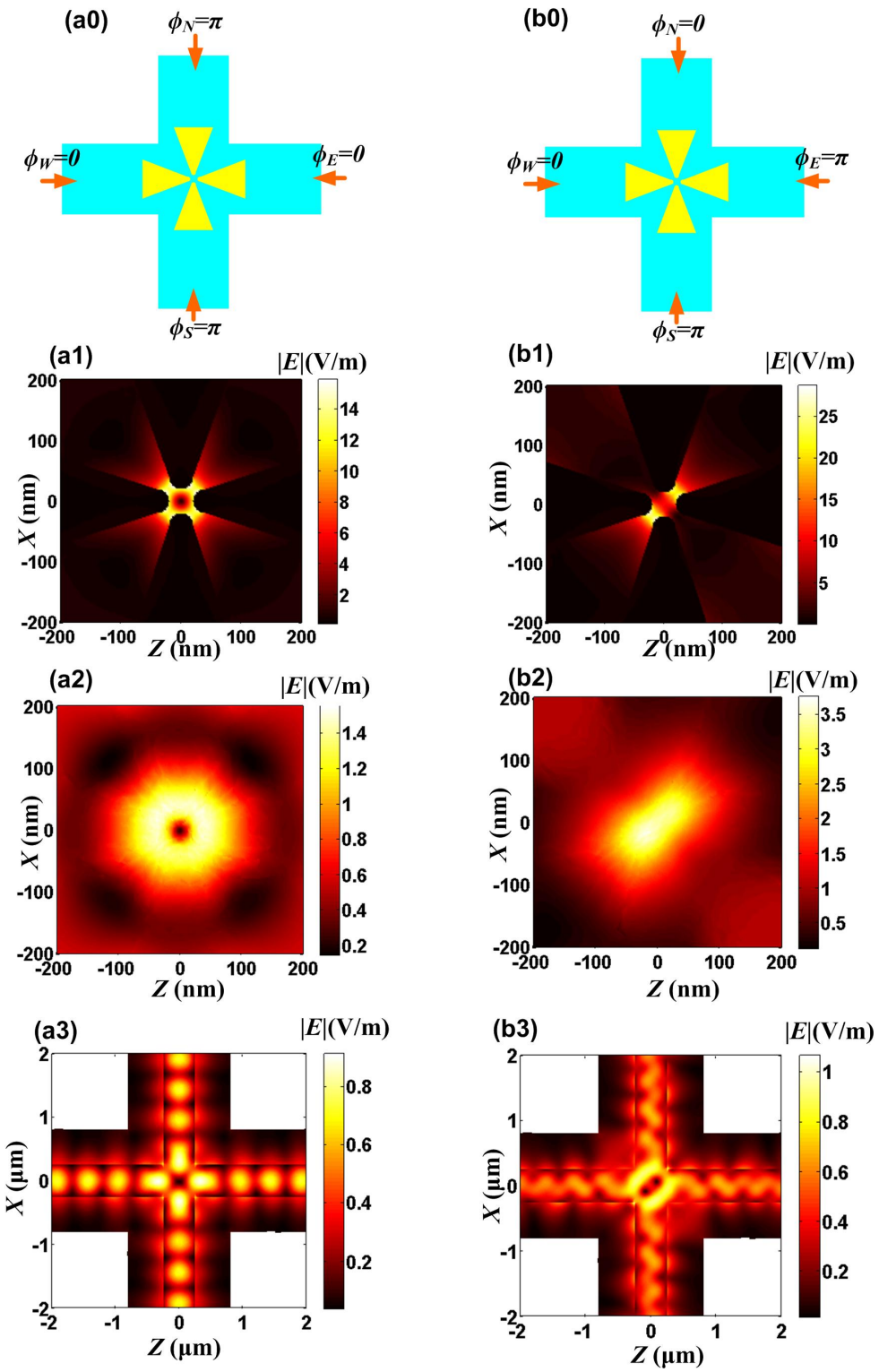

Figure 78: (a0) (a1) (a2) and (a3): four light inputs from all arms with the phase in the north-arm and south-arm inputs being π and the others being 0. (b0) (b1) (b2) and (b3): four light inputs from all arms with the phase in the east-arm and south-arm inputs being π and the others being 0. (a1) and (b1): optical field distributions in plane 'A'. (a2) and (b2): optical field distributions in plane 'B'. (a3) and (b3): optical field distributions in plane 'C'.

in In Figure 78 (a1), there are four hot spots in the gaps between each pair of the adjacent plasmonic tips. Notice that the pattern in Figure 78 (a2) has a shape of octagon with a hollow center.

In Figure 78 (b0) (b1) (b2) and (b3), the phase Φ_W in the west-arm input and the phase Φ_N in the north-arm input are both 0, while the phase Φ_S in the north-arm input and the phase Φ_E in the east-arm input are both π. Based on similar binary logic analysis, the interferences between the adjacent west and south arms and between the adjacent north and east arms are attractive, and the interferences between the adjacent west and north arms and between the adjacent south and east arms are repulsive. Therefore, we are able to observe to hot spots, one in the gap between the plasmonic tips on the west and south arms and the other in the gap between the plasmonic tips on the north and east arms. Because the interferences between the south and north arms and between the west and east arms are also attractive, the field pattern in Figure 78 (b2) does not have a hollow center like the pattern in Figure 78 (a2).

7.3 Conclusion

We have analyzed a strategy of realizing local field configuration in a very small area ($\sim 100\,\text{nm} \times 100\,\text{nm}$) using composite plasmonic structures composed of PLCs with tips closely facing each other. In particular, we analyzed a two-arm structure with two PLCs on a single waveguide and a four-arm structure with four PLCs on two perpendicular waveguides.

Flexible configurations of local field are achieved by phase modulations on each of the input arms. We choose a reference point on each arm with the same distance from the center points of the structures and evaluate the phase at each reference point with a single input from the corresponding arm. The overall local field pattern around the plasmonic pattern is determined by the relative phases on those reference points.

We've discovered that if the relative phase between two arms of inputs is 0, then their interference pattern is destructive (or repulsive), and if the relative phase between two arms of inputs is π, then their interference pattern is constructive (or attractive). Using this simple logic-like criterion, we are able to give analytic estimations of the local behaviors of the interference patterns around the plasmonic tips. There are many interesting local field patterns we can generate with certain modulations of the phases in the input arms.

This mechanism of local field configuration is not specific to our structure in silicon platforms. Actually, as long as you can design your PLC for certain materials of waveguides, buffer layers, substrates and metals with the right dimensions at the right waveguide, you may use this strategy to design local field configurations. For example, we can apply everything in the same form onto a silicon nitride platform working at a wavelength of 800 nm. Then we can apply such local field configurations to generate more complicated optical traps for nano-particles. In particular, we can obtain the ability of not only trapping nano-particles but also doing certian manipulations on the trapped nano-particles by modulating the phases in the input arms.

REFERENCES

REFERENCES

[1] V. Backman, M. B. Wallace, L. T. Perelman, and etc., "Detection of preinvasive cancer cells," Nature **406,** 35–36 (2000).

[2] J. R. Mourant, T. M. Johnson, S. Carpenter, A. Guerra, T. Aida, and J. P. Freyer, "Polarized angular dependent spectroscopy of epithelial cells and epithelial cell nuclei to determine the size scale of scattering structure," J. Biomed. Opt. **7,** 378–387 (2002).

[3] A. Katz, A. Alimova, M. Xu, E. Rudolph, M. Shah, H. E. Savage, R. Rosen, S. A. McCormick, and R. R. Alfano, "Bacteria size determination by elastic light scattering," IEEE J. Sel. Top. Quantum Electron. **9,** 277–287 (2003).

[4] V. P. Maltsev, and K. A. Semyanov, Characterization of bio-particles from light scattering, (VSP, 2004).

[5] H. M. Shapiro, "Practical flow cytometry," (4th ed., WILEY-LISS, 2003).

[6] A. Wax, C. H. Yang, R. R. Dasari and M. S. Feld, "Measurement of angular distributions by use of low coherence interferometry for light-scattering spectroscopy," Optics Letters **26,** 322–324 (2001).

[7] L. T. Perelman, V. Backman, M. Wallace, G. Zonios, R. Manoharan, A. Nusrat, S. Shields, M. Seiler, C. Lima, T. Hamano, I. Itzkan, J. Van Dam, J. M. Crawford, and M. S. Feld, "Observation of periodic fine structure in reflectance from biological tissue: a new technique for measuring nuclear size distribution," Phys. Rev. Lett. **80,** 627–630 (1998).

[8] V. Backman, G. Gurjar, K. Badizadegan, I. Itzkan, R. R. Dasari, L. T. Perelman, and M. S. Feld, "Polarized light scattering spectroscopy for quantitative measurement of epithelial cellular structure in situ," IEEE J. Sel. Top. Quantum Electron. **5,** 1019–1026 (1999).

[9] G. Mie, "Beiträge zur Optik trüber Medien, speziell kolloidaler Metallösungen," Ann. Phys. Leipzig **25,** 377–445 (1908).

[10] W. T. Grandy, "Scattering of waves from large spheres," Cambridge, (2000).

[11] M. I. Misshchenko, J. W. Hovenier, and L. D. Travis, "Light scattering by nonspherical particles, theory, measurements, and applications," Academic Press, (2000).

[12] E. M. Purcel, C. R. Pennypacker, "Scattering and absorption of light by nonspherical dielectric grains," Astrophys. J., **186,** 705–714 (1973).

[13] B. T. Draine, "The discrete-dipole approximation and its application to interstellar graphite grains," Astrophys. J., **333,** 848–872 (1988).

[14] J. D. Klett, and R. A. Sutherland, "Approximate methods for modeling the scattering properties of nonspherical particles: evalution of the Wentzel-Kramers-Brillouin method," Appl. Opt. **31,** 373–386 (1992).

[15] V. N. Lopatin, and N. S. Shepilevich, "Consequences of the integral wave equation in the Wentzel-Kramers-Brillouin approximation," Optics and Spectroscopy **81,** 103–106 (1996).

[16] C. F. Bohren, and D. R. Huffman, "Absorption and scattering of light by small particles," John Wiley & Sons, (1983).

[17] Y. Luo, J. Huang, and A. Adibi, "Accurate determination of microparticle size using Fourier transform of light scattering spectrum over wavenumber," Optics Lett. **32,** 1171–1173 (2007).

[18] C. H. Camp Jr., "Label-free flow cytometry using multiplex coherent anti-stokes Raman scattering (MCARS) spectroscopy," Dissertation submitted to Georgia Institute of Technology, (2011).

[19] J. A. Schuller, E. S. Barnard, W. Cai, Y. Jun, J. S. White, and M. L. Brongersma, "Plasmonics for extreme light concentration and manipulation," Nat. Materials **9,** 193–204 (2010).

[20] F. Wang, and Y. R. Shen, "General properties of local plasmons in metal nanostructures," Phys. Rev. Lett. **97,** 206806 (2006).

[21] Z. Liu, J. M. Steele, W. Srituravanich, Y. Pikus, C. Sun, and X. Zhang, "Focusing surface plasmons with a plasmonic lens," Nano Lett. **5,** 1726–1729 (2005).

[22] W. Chen, D. C. Abeysinghe, R. L. Nelson, and Q. Zhan, "Plasmonic lens made of multiple concentric metallic rings under radially polarized illumination," Nano Lett. **9** 4320–4325 (2009).

[23] L Yin, V. K. Vlasko-Vlasov, J. Pearson, J. M. Hiller, J. Hua, U. Welp, D. E. Brown, and C. W. Kimball, "Subwavelength Focusing and Guiding of Surface Plasmons," Nano Lett. **5,** 1399–1402 (2005).

[24] A. Yanai, and U. Levy, "Plasmonic focusing with a coaxial structure illuminated by radially polarized light," Opt. Express **17,** (2009).

[25] K. V. Nerkararyan, "Superfocusing on a surface polariton in a wedge-like structure," Phys. Lett. A **237,** 103–105 (1997).

[26] A. J. Babadjanyan, N. L. Margaryan, and K. V. Nerkararyan, "Superfocusing of surface polaritons in the conical structure," J. Appl. Phys. **87,** 3785–3788 (2000).

[27] M. I. Stockman, "Nanofocusing of optical energy in tapered plasmonic waveguides," Phys. Rev. lett. **93,** 137404 (2004).

[28] K. C. Vernon, D. K. Gramotnev, and D. F. P. Pile, "Adiabatic nanofocusing of plasmons by a sharp metal wedge on a dielectric substrate," J. Appl. Phys. **101,** 104312 (2007).

[29] E. Moreno, S. G. Rodrigo, S. I. Bozhevolnyi, L. Martín-Moreno, and F. J. García-Vidal, "Guiding and focusing of electromagnetic fields with wedge plasmon polaritons," Phys. Rev. Lett. **100,** 023901 (2008).

[30] S. I. Bozhevolnyi, and K. V. Nerkararyan, "Adiabatic nanofocusing of channel plasmon polaritons," Opt. lett. **35,** 541–543 (2009).

[31] V. S. Volkov, S. I. Bozhevolnyi, S. G. Rodrigo, L. Martín-Moreno, F. J. García-Vidal, E. Devaux, and T. W. Ebbesen, "Nanofocusing with Channel Plasmon Polaritons," Nano Lett. **9,** 1278–1282 (2009).

[32] V. S. Volkov, J. Gosciniak, S. I. Bozhevolnyi, S. G. Rodrigo, L. Martín-Moreno, F. J. García-Vidal, E. Devaux, and T. W. Ebbesen, "Plasmonic candle: towards efficient nanofocusing with channel plasmon polaritons," New J. Phys. **11,** 113043 (2009).

[33] Z. Fang, H. Qi, C. Wang, X. Zhu, "Hybrid Plasmonic Waveguide Based on Tapered Dielectric Nanoribbon: Excitation and Focusing," Plasmonics **5,** 201–212 (2010).

[34] K. Tanaka, K. Katayama, and M. Tanaka, "Nanofocusing of surface plasmon polaritons by a pyramidal structure on an aperture," Opt. Express **18,** (2010).

[35] N. C. Lindquist, P. Nagpal, A. Lesuffleur, D. J. Norris, and S. Oh, "Three-dimensional plasmonic nanofocusing," Nano Lett. **10,** 1369–1373 (2010).

[36] C. Ropers, C. C. Neacsu, T. Elsaesser, M. Albrecht, M. B. Raschke, and C. Lienau, "Grating-coupling of surface plasmons onto metallic tips: A nanoconfined light source," Nano Lett. **7,** 2784–2788 (2007).

[37] E. Verhagen, A. Polman, and L. Kuipers, "Nanofocusing in laterally tapered plasmonic waveguides," Opt. Express **16,** 766–788 (2008).

[38] A. Normatov, P. Ginzburg1, N. Berkovitch, G. M. Lerman, A. Yanai, U. Levy and M. Orenstein, "Efficient coupling and field enhancement for the nano-scale: plasmonic needle," Opt. Express **18,** (2009).

[39] H. Choi, D. F. P. Pile, S. Nam, G. Bartal, and X. Zhang, "Compressing surface plasmons for nano-scale optical focusing," Opt. Express **17,** 7519–7524 (2009).

[40] M. Schnell, P. Alonso-González, L. Arzubiaga, F. Casanova, L. E. Hueso, A. Chuvilin, and R. Hillenbrand, "Nanofocusing of mid-infrared energy with tapered transmission lines," Nature Photonics **5,** 283–287 (2011).

[41] R. Yang, R. A. Wahsheh, Z. Lu, and M. A. G. Abushagur, "Efficiently squeezing near infrared light into a 21 nm-by-24 nm nanospot," Opt. Express **16,** 20142 (2008).

[42] B. Desiatov, I. Goykhman, and U. Levy, "On-Chip Focusing of Light by Metallic Nanotip," 2010 OSA/FiO/LS

[43] B. Desiatov, I. Goykhman, and U. Levy, "Nanoscale mode selector in silicon waveguide for on-chip nanofocusing applications," Nano Lett. **9,** 3381–3386 (2009).

[44] B. Desiatov, I. Goykhman, and U. Levy, "Plasmonic nanofocusing of light in an integrated silicon photonics platform," Opt. Express **19,** 13150–13157 (2011).

[45] Y. Luo, M. Chamanzar, and A. Adibi, "Compact on-chip plasmonic light concentration based on a hybrid photonic-plasmonic structure," Opt. Express **21,** 1898–1910 (2013).

[46] P. Berini, "Plasmon-polariton waves guided by thin lossy metal films of finite width Bound modes of symmetric structures," Phys. Rev. B **61,** 10484–10503 (2000).

[47] P. Berini, "Plasmon-polariton waves guided by thin lossy metal films of finite width Bound modes of asymmetric structures," Phys. Rev. B **63,** 125417 (2001).

[48] R. Charbonneau, P. Berini, E. Berolo and E. Lisicka-Shrzek, "Experimental observation of plasmon-polariton waves supported by a thin metal film of finite width," Opt. Lett. **25,** 844–846 (2000).

[49] J. Park, K. Kim, I. Lee, H. Na, S. Lee, and B. Lee, "Trapping light in plasmonic waveguides," Opt. Express **18,** (2010).

[50] I. Goykhman, B. Desiatov, and U. Levy, "Experimental demonstration of locally oxidized hybrid silicon-plasmonic waveguide," Appl. Phys. Lett **97,** (2010).

[51] D. Dai, and S. He, "Low-loss hybrid plasmonic waveguide with double low-index nano-slots," Opt. Express **18,** (2010).

[52] L. Novotny, "The History of Near-field Optics," Progress in Optics **50,** E. Wolf (ed.), chapter 5, 137–184 (2007).

[53] S. Bourzeix, J. M. Moison, A. F. Mignard, F. Barthe, A. C. Boccara, C. Licoppe, B. Mersali, M. Allovon, and A. Bruno, "Near-field optical imaging of light propagation in semiconductor waveguide structures," Appl. Phys. Lett. **73,** 1035–1037 (1998).

[54] S. Gotzinger, S. Demmerer, O. Benson, and V. Sandoghdar, "Mapping and manipulating whispering gallery modes of a microsphere resonator with a near-field probe," J. Microscopy **202,** 117 (2001).

[55] E. Verhagen, J. A. Dionne, L. Kuipers, H. A. Atwater, and A. Polman, "Near-Field visualization of strongly confined surface plasmon polaritons in metal-insulator-metal waveguides," Nano lett. **8,** 2925–2929 (2008).

[56] J. T. Robinson, C. Manolatou, L. Chen, and M. Lipson, "Ultrasmall mode volumes in dielectric optical microcavities," Phys. Rev. Lett. **95,** 143901 (2005).

[57] A. Apuzzo, M. Février, R. Salas-Montiel, A. Bruyant, and A. Chelnokov, G. Lérondel, B. Dagens, and S. Blaize, "Observation of near-field dipolar interactions involved in a metal nanoparticle chain waveguide," Nano Lett. **13,** 1000–1006 (2013).

[58] Y. Luo, M. Chamanzar, A. Apuzzo, R. Salas-Montiel, K. N. Nguyen, S. Blaize, and A. Adibi, "On-chip plasmonic tapered light concentrator for nanofocusing in an integrated silicon photonic device," submitted to Nano Lett.

[59] A. Ashkin, J. M. Dziedzic, J. E. Bjorkholm and S. Chu, "Observation of a single-beam gradient force optical trap for dielectric particles," Opt. Lett. **11,** 288–290 (1986).

[60] D. G. Grier, "A revolution in optical manipulation," Nature **424,** 810–816 (2003).

[61] Alexandr Jonáš, and Pavel Zemańek, "Light at work: The use of optical forces for particle manipulation, sorting, and analysis," Electrophoresis **29,** 4813–4851 (2008).

[62] J. D. Jackson, "Classical Electrodynamics," (John Wiley Sons, 1999).

[63] W. M. Lee, P. J. Reece, R. F. Marchington, N. K. Metzger, "Construction and calibration of an optical trap on a fluorescence optical microscope," Nat. Protoc. **2,** 3226–3238 (2007).

[64] `http://www.cellrobotics.com`; `http://www.arryx.com`; `http://www.elliotscientific.com`.

[65] A. Ashkin, "Acceleration and trapping of particles by radiationpressure," Phys.Rev.Lett. **24,** 156–159 (1970).

[66] D. Vossen, A. van der Horst, M. Dogterom, and A. van Blaaderen, "Optical tweezers and confocal microscopy for simultaneous three-dimensional manipulation and imaging in concentrated colloidal dispersions," Rev. Sci. Instrum. **75,** 2960–2970 (2004).

[67] P. Rodrigo, L. Gammelgaard, P. Boggild, I. Perch-Nielsen, and J. Glückstad, "Actuation of microfabricated tools using multiple GPC-based counterpropagating-beam traps," Opt. Express **13,** 6899–6904 (2005).

[68] A. Constable, J. Kim, J. Mervis, F. Zarinetchi, and M. Prentiss, "Demonstration of a fiber-optical light-force trap," Opt. Lett. **18,** 1867–1869 (1993).

[69] S. D. Collins, R. J. Baskin, and D. G. Howitt, "MicroInstrument Gradient-Force Optical Trap," Appl. Opt. **38,** 6068–6074 (1999).

[70] J. Guck, R. Ananthakrishnan, T. J. Moon, C. C. Cunningham, and et al., "Optical deformability of soft biological dielectrics," Phys. Rev. Lett. **84,** 5451–5154 (2000).

[71] H. He, M. E. J. Friese, N. R. Heckenberg, and H. Rubinsztein-Dunlop, "Direct observation of transfer of angular momentum to absorptive particles from a laser beam with a phase singularity," Phys. Rev. Lett. **75,** 826–829 (1995).

[72] M. E. J. Friese, J. Enger, H. Rubinsztein-Dunlop, and N. R. Heckenberg, "Optical angular-momentum transfer to trapped absorbing particles," Phys. Rev. A **54,** 1593–1596 (1996).

[73] M. E. J. Friese, T. A. Nieminen, N. R Heckenberg and H. Rubinsztein-Dunlop, "Optical alignment and spinning of laser-trapped microscopic particles," Nature **394,** 348–350 (1998).

[74] M. E. J. Friese, H. Rubinsztein-Dunlop, J. Gold, P. Hagberg, and D. Hanstorp, "Optically driven micromachine elements," Appl. Phys. Lett. **78,** 547–549 (2001).

[75] A. La Porta, M. Wang, "Optical torque wrench: angular trapping, rotation, and torque detection of quartz microparticles," Phys. Rev. Lett. **92,** 190801 (2004).

[76] A. Bishop, T. Nieminen, N. Heckenberg, H. Rubinsztein-Dunlop, "Optical Microrheology Using Rotating Laser-Trapped Particles," Phys. Rev. Lett. **92,** 198104 (2004).

[77] P. Galajda, and P. Ormos, "Orientation of flat particles in optical tweezers by linearly polarized light," Opt. Express **11,** 446C451 (2003).

[78] S. L. Neale, M. P. MacDonald, K. Dholakia, and T. F. Krauss, "All-optical control of microfluidic components using form birefringence," Nat. Mater. **4,** 530–533 (2005).

[79] Z. Cheng, P. Chaikin, and T. Mason, "Light streak tracking of optically trapped thin microdisks," Phys. Rev. Lett. **89,** 108303 (2002).

[80] E. Higurashi, H. Ukita, H. Tanaka, and O. Ohguchi, "Optically induced rotation of anisotropic micro-objects fabricated by surface micromachining," Appl. Phys. Lett. **64,** 2209–2210 (1994).

[81] P. Galajda, and P. Ormos, Complex micromachines produced and driven by light, Appl. Phys. Lett. **78,** 249–251 (2001).

[82] L. Paterson, M. P. MacDonald, J. Arlt, W. Sibbett, P. E. Bryant, and K. Dholakia, "Controlled rotation of optically trapped microscopic particles," Science **292,** 912–914 (2001).

[83] S. Kawata, and T. Sugiura, "Movement of micrometer-sized particles in the evanescent field of a laser beam," Opt. Lett. **17,** 772–774 (1992).

[84] K. Wada, K. Sasaki, and H. Masuhara, "Optical measurement of interaction potentials between a single microparticle and an evanescent field," App. Phys. Lett. **76,** 2815–2817 (2000).

[85] Y. Hayashi, S. Ashihara, T. Shimura, and K. Kuroda, "Simultaneous separation of polydisperse particles using an asymmetric nonperiodic optical stripe pattern," App. Opt. **48** 1543–1552 (2009).

[86] T. Čižmár, M. Šiler, M. Šerý, and P. Zemánek, "Optical sorting and detection of submicrometer objects in a motional standing wave," Phys. Rev. B **74,** 035105 (2006).

[87] I. Ricárdez-Vargas, P. Rodríguez-Montero, R. Ramos-García, and K. Volke-Sepúlveda, "Modulated optical sieve for sorting of polydisperse microparticles," Appl. Phys. Lett. **88,** 121116 (2006).

[88] R. F. Marchington, M. Mazilu, S. Kuriakose, V. Garcés-Chávez, P. J. Reece, T. F. Krauss, M. Gu, and K. Dholakia, "Optical deflection and sorting of microparticles in a near-field optical geometry," Opt. Express **16,** 3712–3726 (2008).

[89] G. Brambilla, G. S. Murugan, J. S. Wilkinson, D. J. Richardson, "Optical manipulation of microspheres along a subwavelength optical wire," Opt. Lett. **32,** 3041–3043 (2007).

[90] S. Arnold, D. Keng, S. I. Shopova, S. Holler, W. Zurawsky, and F. Vollmer, "Whispering gallery mode carousel - a photonic mechanism for enhanced nanoparticle detection in biosensing," Opt. Express **17,** 6230–6238 (2009).

[91] S. Kawata, and T. Tani, "Optically driven Mie particles in an evanescent field along a channeled waveguide," Opt. Lett. **21,** 1768–1770 (1996).

[92] S. Gaugiran, S. Gétin, J. M. Fedeli, G. Colas, A. Fuchs, F. Chatelain, and J. Dérouard, "Optical manipulation of microparticles and cells on silicon nitride waveguides," Opt. Express **13,** 6956–6963 (2005).

[93] K. Grujic, O. G. Hellesø, J. P. Hole, and J. S. Wilkinson, "Sorting of polystyrene microspheres using a Y-branched optical waveguide," Opt. Express 13, 1–7 (2005).

[94] K. Grujic and O. G. Hellesø, "Dielectric microsphere manipulation and chain assembly by counter-propagating waves in a channel waveguide," Opt. Express **15,** 6470–6477 (2007).

[95] D. Psaltis, S. R. Quake, and C. H. Yang, "Developing optofluidic technology through the fusion of microfluidics and optics," Nature **442,** 381–386 (2006).

[96] C. Monat, P. Domachuk, and B. J. Eggleton, "Integrated optofluidics: A new river of light," Nature Photon. **1,** 106–114 (2007).

[97] B. S. Schmidt, A H. J. Yang, D Erickson, and M Lipson, "Optofluidic trapping and transport on solid core waveguides within a microfluidic device," Opt. Express **15,** 14322–14334 (2007).

[98] Yang, A. H. J. et al, Optical manipulation of nanoparticles and biomolecules in sub-wavelength slot waveguides. Nature **457,** 71–75 (2009).

[99] S. Lin, E. Schonbrun, and K. Crozier, "Optical manipulation with planar silicon microring resonators," Nano Lett. **10,** 2408–2411 (2010).

[100] G. Volpe, R. Quidant, G. Badenes, and D. Petrov, "Surface plasmon radiation forces," Phys. Rev. Lett. **96,** 238101 (2006).

[101] M. Righini, A. S. Zelenina, C. Girard, and R. Quidant, "Parallel and selective trapping in a patterned plasmonic landscape," Nat. Phys. **3,** 477–480 (2007).

[102] X. Miao, and L. Y. Lin, "Trapping and manipulation of biological particles through a plasmonic platform," IEEE J. Sel. Top. Quant. Electron. **13,** 1655–1662 (2007).

[103] Y. Pang, and R. Gordon "Optical trapping of 12 nm dielectric spheres using double-nanoholes in a gold film," Nano Lett., **11,** 3763–3767 (2011).

[104] M. I. Stockman, "Nanoplasmonics: past, present, and glimpse into future," Opt. Express **19,** 22029–22106 (2011).

[105] A. N. Grigorenko, N. W. Roberts, M. R. Dickinson,and Y. Zhang "Nanometric optical tweezers based on nanostructured substrates," Nat. Photonics **2,** 365–370 (2008).

[106] Mathieu L. Juan, Reuven Gordon, Yuanjie Pang, Fatima Eftekhari, and Romain Quidant, "Self-induced back-action optical trapping of dielectric nanoparticles," Nature Physics **5** (2009), 915–919.

[107] Y. Pang, and R. Gordon "Optical trapping of 12 nm dielectric spheres using double-nanoholes in a gold film," Nano Lett., **11,** 3763–3767 (2011).

[108] Y. Tsuboi, T. Shoji, N. Kitamura, M. Takase, K. Murakoshi, Y. Mizumoto, and H. Ishihara, "Optical trapping of quantum dots based on gap-mode-excitation of localized surface plasmon," Phys. Chem. Lett. **1**, 2327–2333 (2010).

[109] K. Wang, E. Schonbrun, P. Steinvurzel, and K B. Crozier "Trapping and rotating nanoparticles using a plasmonic nano-tweezer with an integrated heat sink," Nat. Communications **2,** 469 (2011).